Structural Analysis of JC Polyomavirus Receptors and Inhibitors

Dissertation

der Mathematisch-Naturwissenschaftlichen Fakultät

der Eberhard Karls Universität Tübingen

zur Erlangung des Grades eines

Doktors der Naturwissenschaften

(Dr. rer. nat.)

vorgelegt von

M.Sc. Christina Harprecht

aus Bitburg

Tübingen

2019

Gedruckt mit Genehmigung der Mathematisch-Naturwissenschaftlichen Fakultät der Eberhard Karls Universität Tübingen.

Tag der mündlichen Qualifikation:	09.07.2019
Dekan:	Prof. Dr. Wolfgang Rosenstiel
1. Berichterstatter:	Prof. Dr. Thilo Stehle
2. Berichterstatter:	Prof. Dr. Dirk Schwarzer

Structural Analysis of JC Polyomavirus Receptors and Inhibitors

Dissertation

der Mathematisch-Naturwissenschaftlichen Fakultät

der Eberhard Karls Universität Tübingen

zur Erlangung des Grades eines

Doktors der Naturwissenschaften

(Dr. rer. nat.)

vorgelegt von

M.Sc. Christina Harprecht

aus Bitburg

Tübingen

2019

Gedruckt mit Genehmigung der Mathematisch-Naturwissenschaftlichen Fakultät der Eberhard Karls Universität Tübingen.

Tag der mündlichen Qualifikation:	09.07.2019
Dekan:	Prof. Dr. Wolfgang Rosenstiel
1. Berichterstatter:	Prof. Dr. Thilo Stehle
2. Berichterstatter:	Prof. Dr. Dirk Schwarzer

Abstract

Polyomaviruses are non-enveloped, double-stranded DNA viruses that have been found to infect mammals, birds and fish. The first two discovered human polyomaviruses, JC polyomavirus (JCPyV) and BK polyomavirus (BKPyV), are closely related, and the majority of the population is seropositive for these viruses. While they generally cause an asymptomatic, persistent infection in healthy individuals, they can trigger severe diseases in immunocompromised patients. In the case of JCPyV, viral reactivation results in infection of astrocytes and oligodendrocytes in the central nervous system. This in turn leads to the fatal disease Progressive Multifocal Leukoencephalopathy (PML), which is characterized by the demyelination of these cells. For BKPyV, infection can lead to polyomavirus-associated nephropathy (PVAN) and hemorrhagic cystitis in renal transplant patients. About 10% of kidney transplant patients suffer a graft loss thereafter. So far, there is no efficient cure other than the reconstitution of the immune system for either disease.

The icosahedral polyomavirus capsid is comprised of 72 pentamers of the major capsid protein VP1. Each VP1 pentamer is typically associated with one copy of a minor capsid protein, VP2 or VP3. The structure of a VP1 monomer is characterized by a jelly-roll fold consisting of a conserved β-barrel core and highly divergent loops connecting the β-strands. Thus, the loops confer receptor specificity and polyomaviruses have been shown to rely on sialylated carbohydrate receptors for host cell attachment. For JCPyV, it has been shown that the engagement of lactoseries tetrasaccharide c (LSTc) is required for the attachment of JCPyV to host cells. More recently, the adipocyte plasma membrane-associated protein APMAP was identified as putative receptor for JCPyV. Little is known about this type II transmembrane protein, and its extracellular region, which is responsible for binding to JCPyV, was investigated in the course of this work. Secondary structure prediction of the extracellular region indicated the presence of a six-bladed β-propeller, with each blade containing a twisted four-stranded antiparallel β-sheet. This prediction is supported by CD spectroscopic analysis of purified protein. The work performed in this project provides a platform for future studies about the structure of APMAP, its function and its molecular interactions with JCPyV VP1.

Since there is still no efficient cure for diseases caused by JCPyV nor BKPyV, an important goal is to develop strategies to interfere with virus receptor binding or to block viral assembly. One possibility for preventing virus receptor interactions or viral assembly is the design of small molecule compounds that can act as viral attachment or assembly inhibitors. This was one project investigated in this work. Fragment-based drug discovery was conducted in order to find small molecule fragments that were analyzed in crystal soaking experiments with JCPyV VP1. Two compounds were shown to bind to JCPyV VP1, both of which display the same binding site. The binding site is located on the inside of the VP1 pentamer and does partially overlap with the VP2 binding site. Based on the identified compounds, molecular modeling studies were performed to find new compounds displaying a higher affinity towards JCPyV VP1. Since none of these compounds was shown to bind, another approach was pursued. Based on the sequence of JCPyV VP2, peptides that were hypothesized to bind to JCPyV VP1 with high affinity were designed and crystallized

with JCPyV VP1. Although difference omit maps were observed in multiple data sets, assignment to any peptide structure was not possible and binding of these peptides to JCPyV VP1 could thus not be confirmed.
In a third project, JCPyV VP1 protein in complex with single-chain variable fragments of the cross-neutralizing, monoclonal antibody 29B1 was structurally analyzed. The crystal structure revealed the antibody epitope and shed light onto the neutralization escape of characteristic PML mutants. Furthermore, comparison with the complex structure of BKPyV VP1 allowed for the detection of subtle differences in binding of 29B1 between JCPyV VP1 and BKPyV VP1. Together with the analysis of previously solved crystal structures of JCPyV VP1 – antibody fragment complexes, the different binding profiles of these antibodies to JCPyV VP1 variants could be explained. This knowledge could provide a platform for a rational design of vaccines and therapeutic antibodies.

Zusammenfassung

Polyomaviren zählen zu den nicht-umhüllten, Doppelstrang-DNA Viren, die Säugetiere, Vögel und Fische infizieren können. Die zuerst entdeckten menschlichen Polyomaviren, JC Polyomavirus (JCPyV) und BK Polyomavirus (BKPyV) sind eng miteinander verwandt und die Mehrzahl der weltweiten Bevölkerung ist seropositiv für diese Viren. Während sie generell eine asymptomatische, persistierende Infektion in gesunden Individuen hervorrufen, so können sie zu ernsten Erkrankungen in immunkompromittierten Patienten führen. Im Falle von JCPyV resultiert die virale Reaktivierung zur Infektion von Astrozyten und Oligodentrozyten im zentralen Nervensystem. Dies wiederum führt zur meist tödlich verlaufenden Krankheit Progressive Multifokale Leukoenzephalopathie, die sich durch die Demyelinisierung dieser Zelltypen auszeichnet. Für BKPyV kann eine Infektion bei Nierentransplantationspatienten zu Polyomavirus-assoziierter Nephropathie (PVAN) und hämorrhagischer Zystitis führen. Hierdurch erleiden etwa 10% aller Nierentransplantationspatienten eine Abstoßung und Verlust des Spenderorgans. Bislang gibt es keine andere effiziente Heilungsstrategie als die Wiederherstellung des Immunsystems.

Das ikosahedrale Polyomavirus-Kapsid setzt sich aus 72 Kopien der Haupt-Kapsidproteins VP1-Pentamere zusammen. Diese VP1-Pentamere sind in der Regel mit einer Kopie eines Neben-Kapsidproteins, entweder VP2 oder VP3, assoziiert. Die VP1-Struktur weist eine typische ‚jelly-roll'-Faltung mit einer konservierten β-barrel Kernstruktur und stark divergierenden Loopregionen auf. Diese Loopregionen vermitteln die Rezeptorspezifität, während Polyomaviren nachweislich auf sialylierte Kohlenhydratrezeptoren zur Bindung an die Wirtszelle angewiesen sind.
Für JCPyV hat sich gezeigt, dass das Vorhandensein des Lactoseries Tetrasaccharides c (LSTc) für die Bindung von JCPyV an Wirtszellen erforderlich ist. Vor kurzem wurde das Adipozytenplasmembran assoziierte Protein APMAP als mutmaßlicher Rezeptor für JCPyV identifiziert. Über dieses Transmembranprotein vom Typ II ist wenig bekannt und der extrazelluläre Teil, der für die Bindung an JCPyV verantwortlich ist, wurde im Rahmen dieser Arbeit untersucht. Die Sekundärstrukturvorhersage ergab einen sechsblättrigen β-Propeller, wobei jede Propellerschaufel ein in sich verdrehtes viersträngiges antiparalleles β-Faltblatt enthielt. Diese Vorhersage konnte durch die Analyse von CD-Spektren des gereinigten Proteins bestätigt werden. Die in diesem Projekt durchgeführten Arbeiten bieten die Grundlage für zukünftige Studien über die Proteinstruktur, -funktion und mögliche Interaktionen mit JCPyV VP1.

Da es für die von JCPyV und BKPyV hervorgerufenen Krankheiten nach wie vor keine wirksame Therapie gibt, ist es ein Ziel, geeignete Mittel zu finden, um die Bindung des Virus an den Rezeptor zu unterbinden oder die virale Zusammensetzung zu blockieren. Eine Möglichkeit, die Wechselwirkungen zwischen Virus und Rezeptor zu inhibieren oder den viralen Aufbau zu verhindern, stellt das Design von niedermolekularen Verbindungen dar, die als Inhibitoren fungieren können. Dieses Projektwurde im Rahmen dieser Arbeit untersucht. Dabei wurde das Prinzip der fragmentbasierten Wirkstoffentdeckung angewendet, um kleine Molekülfragmente zu finden, die in Soaking-Experimenten mit JCPyV VP1-Kristallen analysiert wurden. Es konnte gezeigt werden, dass zwei Verbindungen an JCPyV VP1 binden, wobei beide die gleiche Bindungsstelle aufweisen. Die Bindungsstelle

befindet sich dabei innerhalb des VP1-Pentamers und überlappt teilweise mit der VP2-Bindungsstelle. Basierend auf den identifizierten Verbindungen wurden Molecular Modeling Studien durchgeführt, um neue Verbindungen mit einer höheren Affinität zu JCPyV VP1 zu finden. Da keine dieser Compounds nachweislich bindet, wurde ein anderer Ansatz verfolgt. Basierend auf der Sequenz von JCPyV VP2 wurden Peptide entwickelt, die mit hoher Affinität an JCPyV VP1 binden sollten. Die in der Proteinkristallstruktur beobachtete Differenzelektronendichte konnte keiner Peptidsequenz zugeordnet werden und eine Bindung der Peptide an JCPyV VP1 konnte somit nicht bestätigt werden.

In dieser Arbeit wurde das JCPyV VP1-Protein im Komplex mit singlechain-variablen Fragmenten des kreuzneutralisierenden, monoklonalen Antikörpers 29B1 strukturell analysiert. Durch die Strukturaufklärung wurde das Antikörperepitop bestimmt und erklärt, wie charakteristische PML-Mutanten der Antikörperneutralisation entgehen können. Der Vergleich mit der BKPyV VP1 Komplexstruktur deckte subtile Unterschiede im Bindungsmuster von 29B1 an JCPyV VP1 und BKPyV VP1 auf. Zusammen mit der Analyse von zuvor gelösten Kristallstrukturen von JCPyV VP1 - Antikörperfragmentkomplexen konnten die unterschiedlichen Bindungsprofile dieser Antikörper zu verschiedenen JCPyV VP1-Varianten erörtert werden. Dieses Wissen kann dazu genutzt werden, Impfstoffe und therapeutische Antikörper zu entwickeln.

Contributions of Others

All of the experiments described in this thesis were performed by me, with exceptions clearly indicated in the text.

Contents

Abbreviations

3C	human rhinovirus 3C protease
5-HTR	5-hydroxytryptamine, serotonine receptor
aa	amino acid
Ac	acetate
AIDS	Acquired Immunodeficiency Syndrome
Amp	Ampicillin
APMAP	adipocyte plasma membrane associated protein
APS	ammonium persulfate
ASU	asymmetric unit
BKPyV	BK polyomavirus
bp	basepairs
cw	clockwise
ccw	counter-clockwise
CDR	complementary determining region
CFS	cerebrospinal fluid
CNS	central nervous system
Da	Dalton
DNA	Desoxyribonucleic acid
ds DNA	double-stranded DNA
E. coli	*Escherichia coli*
Fab	fragment antigen-binding
FDA	food and drug administration
GAG	Glycosaminoglycan
Gal	Galactose
h	hour
HBGA	Histo-blood group antigen
IPTG	isopropyl-β-D-thiogalactopyranoside
JCPyV	JC polyomavirus
Kan	kanamycin
kDa	kilodalton
L	liter
LB	Lysogeny Broth
LSTc	lactoseries tetrasaccharide c
mAb	monoclonal antibody
mAu	milli absorption units
min	minutes
MPyV	murine polyomavirus
mL	milliliter
MWCO	molecular weight cut-off
NCS	non-crystallographic symmetry
Neu5Ac	5-N-acetyl-neuraminic acid
NLS	nuclear localization signal
NPS	nitrate phosphate sulfate
OD_{600}	optical density at wavelength 600
PML	progressive multifocal leukoencephalopathy
PMSF	phenylmethanesulfonylfluoride
r.m.s.d.	root mean square deviation

rpm	revolutions per minute
s	seconds
scFv	single chain variable fragment
SDS	sodium dodecyl sulfate
SDS-PAGE	sodium dodecyl sulfate polyacrylamide gel electrophoresis
SEC	size exclusion chromatography
SOC	Super Optimal Broth
SV40	simian virus 40
TCEP	tris(2-carboxyethyl)phosphine
TEA	triethanolamine
TEV	tobacco etch virus
V_H	variable region heavy chain
V_L	variable region light chain
VLP	virus-like particle
VP1	viral protein 1
VP2	viral protein 2
VP3	viral protein 3
VP4	viral protein 4
(w/v)	weight per volume

1. Introduction

1.1 Polyomaviruses

Polyomaviruses constitute the family of *Polyomaviridae*. They were first described in 1953 by Ludwig Gross (Gross 1953) and their name is derived from the Greek words *poly-*, meaning many, and *-oma*, which means tumor. Murine polyomavirus (MPyV) and simian vacuolating virus (SV40) were the first polyomaviruses to be discovered (Stewart, Eddy, and Borgese 1958; Sweet and Hilleman 1960), and they still serve as model systems for studying eukaryotic molecular biology. MPyV causes tumor formation when inoculated in mice.an these were the first organisms found to be carrying polyomaviruses. Since then, polyomaviruses have been found to infect birds, fish and mammals. Currently, there are 13 human polyomaviruses. So far, a total number of 77 polyomaviruses are known, and they belong to four genera, *Alphapolyomavirus*, *Betapolyomavirus*, *Gammapolyomavirus* and *Deltapolyomavirus*. Five species could not be assigned to any genus (ICTV Report Polyomaviridae).
Four of the 13 known human polyomaviruses were shown to cause disease (Gardner et al. 1971; Padgett et al. 1971; Allander et al. 2007; Gaynor et al. 2007; van der Meijden et al. 2010). The first two of these, JC polyomavirus (JCPyV) and BK polyomavirus (BKPyV), were characterized in 1971 and received their name from the initials from the patients they were isolated from (Gardner et al. 1971; Padgett et al. 1971). For almost 40 years, JCPyV and BKPyV were the only known human polyomaviruses, but with technological advancements in the last two decades, genetic screening and high-throughput sequencing techniques led to the discovery of several new polyomaviruses. This includes Trichodysplasia spinulosa-associated polyomavirus (TSPyV), which was discovered in a rare skin condition (van der Meijden et al. 2010) and Merkel Cell polyomavirus (MCPyV), which is associated with Merkel Cell Carcinoma (MCC), a rare, but aggressive form of skin cancer. MCPyV is the first polyomavirus that is known to cause cancer in humans (Feng et al. 2008). Between 1955 and 1963, a prominent member of the polyomavirus family, Simian Virus (SV40), came into focus due to the contamination of poliovirus vaccines. Almost one hundred million people in the US have been inadvertently exposed to SV40 through vaccination with contaminated vaccines (Shah and Nathanson 1976). SV40 shows transforming abilities in cell culture and has oncogenic potential in small animal models such as hamsters. Concerns about the oncogenic potential and SV40 induced tumors in humans arose, but could not be confirmed (Shah 2007). The potential oncogenicity has reinforced the interest in polyomaviruses and their role in diseases and cancer (Dalianis and Hirsch 2013; De Gascun and Carr 2013; Moens, Van Ghelue, and Ehlers 2014). Seroprevalence studies have shown that polyomaviruses infect a large proportion of the population worldwide. The seroprevalence increases typically during childhood, indicating that primary exposure occurs in early stages of life (Kean et al. 2009).
Polyomaviruses are nonenveloped viruses and comprising a small, circular, double-stranded DNA genome of about 5,000 bp. The genome is packed into an icosahedral capsid, which is about 40 - 45 nm in diameter. The typical polyomavirus genome

codes for five to nine proteins, whereas two transcriptional regions are defined, the early and late regions, depending on transcription onset during the infection. Early during infection, the nonstructural proteins large tumor antigen (LTAg) and small tumor antigen (STAg) are expressed, which are responsible for the promotion of viral replication and the transforming properties of polyomaviruses. The three capsid proteins, VP1, VP2 and VP3, are considered late proteins because expression starts after the replication of viral DNA. Some polyomaviruses produce additional early and late proteins with VP4 encoded by simian virus 40 (SV40) being one example for an additional late protein. Unlike VP1, VP2 and VP3, VP4 is not a component of the virus particle, but a regulatory protein involved in egress (Ehlers and Moens 2014).
Polyomaviruses show high homology to one another. In particular, JCPyV and BKPyV show a sequence identity between the VP1 proteins of 87%. The work presented in this thesis focuses on JCPyV and the closely related BKPyV. Studies about JCPyV receptors and inhibitors could also be translated to the highly similar BKPyV, as seen for cross-neutralizing antibodies (Jelcic et al. 2015).

1.1.1 Epidemiology and Pathogenesis

JCPyV

About 50 to 80% of the human population are seropositive for JCPyV (Kean et al. 2009; Egli et al. 2009; Knowles et al. 2003). The virus causes a persistent, asymptomatic infection in the kidney, bone marrow and B-lymphocytes of healthy individuals and remains latent in an archetypal form that is incapable of successfully infecting glial cells (Major et al. 1990; Monaco et al. 1996; Dubois et al. 1997; Chapagain and Nerurkar 2010; Monaco et al. 1998). JCPyV likely infects via the upper respiratory tract by close interpersonal contact and might spread by the hematogenous route (Ferenczy et al. 2012). Virus transmission can also occur, albeit rarely, by semen or organ transplantation, or urine-to-oral and by vertical transplacental and perinatal transmission (Bofill-Mas and Girones 2001; Bellizzi, Anzivino, Rodio, Cioccolo, et al. 2013; Boldorini et al. 2011). The virus sheds in the urine of healthy individuals (Yogo et al. 1990) and the detection of JCPyV in stool samples and in urban sewage worldwide may have implications on the transmission through contaminated water and by a fecal-oral route (Hamza et al. 2009; McQuaig et al. 2009; Ahmed et al. 2010; Bofill-Mas et al. 2003). Infection is usually asymptomatic in healthy individuals. However, under conditions of immune modulation or immunosuppression, JCPyV can become reactivated and spread to the central nervous system (CNS) (Dubois et al. 1997; Ferrante et al. 1995; Gorelik et al. 2011). Here it infects astrocytes and oligodendrocytes (Du Pasquier et al. 2003; Koralnik et al. 2005; Wuthrich et al. 2009). B-lymphocytes have been proposed to be the main carrier for JCPyV and thus enabling the virus to disseminate from and/or towards the brain via the blood-brain barrier (BBB) (Tornatore et al. 1992; Chapagain and Nerurkar 2010; Van Loy et al. 2015). Glial cells and especially oligodendrocytes are crucial for myelination in the CNS. JCPyV infection of oligodendrocytes results in their cytolytic destruction.
JCPyV is the causative agent of Progressive Multifocal Leukoencephalopathy (PML), a fatal, demyelinating disease involving progressive damage to brain white matter. PML has been mainly associated with patients with Human Immunodeficiency

Virus/Acquired Immune Deficiency Syndrome (HIV/AIDS) and patients undergoing prolonged immunomodulating treatments for immune-mediated diseases such as multiple sclerosis (MS) (Tan and Koralnik 2010; Bellizzi, Anzivino, Rodio, Palamara, et al. 2013; Diotti et al. 2013). Natalizumab was the first immunomodulating therapy of MS patients that was linked to PML (Berger 2017; Gorelik et al. 2010). Other immunomodulatory drugs like fingolimod, rituximab and dimethyl fumarate (DMF) have also been linked to the development of PML (Vargas and Tyor 2017; Carson et al. 2009). In the CNS, JCPyV leads to infection of glial cells, astrocytes and oligodendrocytes causing severe demyelination and thus PML (Silverman and Rubinstein 1965; Zurhein and Chou 1965; Major et al. 1985; Major et al. 1992; Kondo et al. 2014). PML is characterized by a fast progression, and is fatal within months if left untreated (Khanna et al. 2009). There is no efficient treatment against PML so far, other than the reconstitution of the immune system (Pavlovic et al. 2015; Tan et al. 2011; Vermersch et al. 2011; Prosperini et al. 2016). The immune system reconstitution can lead to the development of immune reconstitution inflammatory syndrome (IRIS), which is characterized by T and B cells infiltrating the brain and causing prominent inflammation of the infected tissue. This inflammation leads to elimination of the virus, but often the consequences are acute neurological deterioration and additional brain damage and might even result in death due to tissue swelling (Tan et al. 2011; Aly et al. 2011; Metz et al. 2012). How JCPyV exactly enters the CNS is currently unknown, however, it could be transferred as free virus or carried by B-cells (Chapagain and Nerurkar 2010). There are several routes of entry for B-cells into the CNS, which could also apply to JCPyV. It could be transferred directly to glial cells from B-cells that have entered the CNS parenchyma or indirectly enter via the blood-brain barrier (BBB), blood-meningeal barrier (BMB) or blood-CSF barrier (BCSFB).

BKPyV

BKPyV was isolated from the urine sample of a renal transplant patient and was named after the initials of said patient (Gardner et al. 1971). About 75% of the population are seropositive for BKPyV (Knowles 2006). Like JCPyV, BKPyV also establishes a lifelong, asymptomatic infection in the epithelial cells of the urinary tract. However, in immunocompromised patients the virus can replicate to pathogenic levels. BKPyV infections can lead to polyomavirus-associated nephropathy (PVAN) and hemorrhagic cystitis in renal transplant patients (Bennett, Broekema, and Imperiale 2012; Rinaldo, Tylden, and Sharma 2013). Seemingly, the virus in the donor kidney can hijack and replicate to pathogenic levels in transplant recipients who lack antibody responses against the virus in the graft (Pastrana et al. 2012; Scadden et al. 2017; Schmitt et al. 2014; Schwarz et al. 2016; Solis et al. 2018). About 10% of kidney transplant patients are affected by PVAN, which occurs early after transplant, likely when immunosuppression is at its peak (Hirsch et al. 2005). In kidney transplant patients, the virus initially replicates in the distal tubular cell, leading to necrosis and inflammation initiation (Lamarche et al. 2016). Recent studies furthermore suggest that BKPyV might also play a causal role in cancers of the urinary tract, especially in kidney transplant patients. These individuals show an increased risk of developing

bladder and kidney cancer (Frasca et al. 2015; Tillou and Doerfler 2014; Gupta et al. 2018).

1.1.2 Structure and Organization of the Polyomavirus Capsid

Major Capsid Protein VP1

The polyomavirus capsid has a diameter of approximately 45 to 50 nm, and the major component is the major viral protein VP1. Five VP1 monomers are assembled around a fivefold symmetry axis to form a VP1 pentamer, and the virion is comprised of 72 copies, which are centered on the vertices of a T=7dextro (T=7d) icosahedral lattice. Capsomer interactions mainly involve the VP1 carboxy-terminus invading a neighboring pentamer, and then are further stabilized by calcium ions and disulfide bonds between the pentamers (Ishizu et al. 2001). Every VP1 pentamer interacts with a single copy of either VP2 or VP3 on its inner cavity (Liddington et al. 1991; Stehle and Harrison 1996; Chen, Stehle, and Harrison 1998). This interaction is predicted to occur in one of five symmetry-related orientations, and binding is mediated by the common C-terminal 105 residues of VP2/VP3 in this location (Griffith et al. 1992; Chen, Stehle, and Harrison 1998). Yet, only 20 amino acids were resolved and these residues are proposed to insert in a hairpin-like manner into the VP1 cavity (Chen, Stehle, and Harrison 1998). The tertiary structure of the major capsid protein VP1 features an N-terminal arm, a jelly-roll β-sandwich core and a long C-terminal extension (Liddington et al. 1991). Polyomavirus VP1 in its monomeric form is formed by two antiparallel β-sheets. These are comprised of strands B, I, D and G (BIDG-sheet) and a second one formed by strands C, H, E and F (CHEF-sheet). These two β-sheets form a jelly-roll fold, a motif that frequently can be found in virus capsid proteins (Stehle et al. 1994; Stehle and Harrison 1996; Liddington et al. 1991). Polyomavirus VP1 structures show characteristic extended and structurally variable surface loops that protrude from the otherwise conserved β-strand core. The strands B, I, D, G2 and C, H, E, F are connected via these loops, hence these loops are named e.g. BC-, DE-, HI- and EF-loops (Liddington et al. 1991; Stehle and Harrison 1997; Neu et al. 2008; Neu et al. 2010; Neu, Bauer, and Stehle 2011; Neu, Khan, et al. 2013; Neu, Allen, et al. 2013; Khan et al. 2014). The BC-loop is further divided into two regions, BC1- and BC2-loop, which protrude from the top of VP1 into different directions. The G-strand is similarly divided into two parts, G1 and G2, where G1, the N-terminal region, of one monomer contributes to the CHEF-sheet of the clockwise neighbor. The G2-part contributes to the BIDG sheet.

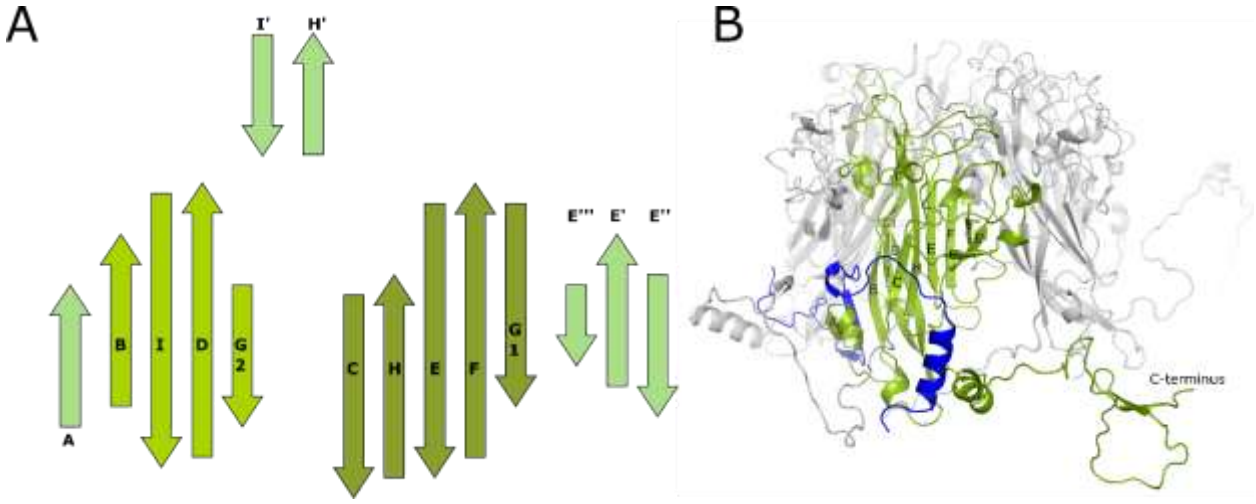

Figure 1. Illustration of the characteristic jelly-roll fold and the structure of SV40 VP1. (A) Schematic illustration of the β-sheets of VP1. The two sheet-structures BIDG and CHEFG are highlighted in darker green and loops between strands are shown as lines. (B) One monomer of the VP1 pentamer is shown in green and neighboring VP1 monomers in grey (PDB code 1SVA). The conserved β-sheets are connected via the protruding surface loops, BC-, DE--, HI- and EF-loops. The BC loop is subdivided into a BC1- and a BC2-part, facing different directions. In the contextual role of the virion, the incoming C-terminal arm, contributed by a neighboring pentamer, is shown in blue.

Contrary to the other loops, the EF-loop protrudes from the bottom of the VP1 pentamer and includes a small three-stranded β-sheet (termed E''', E' and E'') on the side of the pentamer (Stehle and Harrison 1996). Monomers are identical throughout the capsid and neighboring monomers within the pentameric unit form extensive interfaces comprising about 2,200 to 2,800 Å^2 (Protein Interfaces, surfaces and assemblies service PISA at the European Bioinformatics Institute, http://www.ebi.ac.uk/pdbe/prot_int/pistart.html; (Krissinel and Henrick 2007)). The C-terminal arm of VP1 emerges from the base of the monomer and interacts with VP1 from a neighboring pentamer, thus tying together the pentamers within the capsid (Liddington et al. 1991; Stehle and Harrison 1996). In the fully assembled virion, most pentamers contact each other primarily through the C-terminal arms. Each pentamer receives five invading C-terminal arms, one from each of five other pentamers, and donates five C-terminal arms to the surrounding pentamers. The exchange pattern among different pentamers determines the surface lattice.

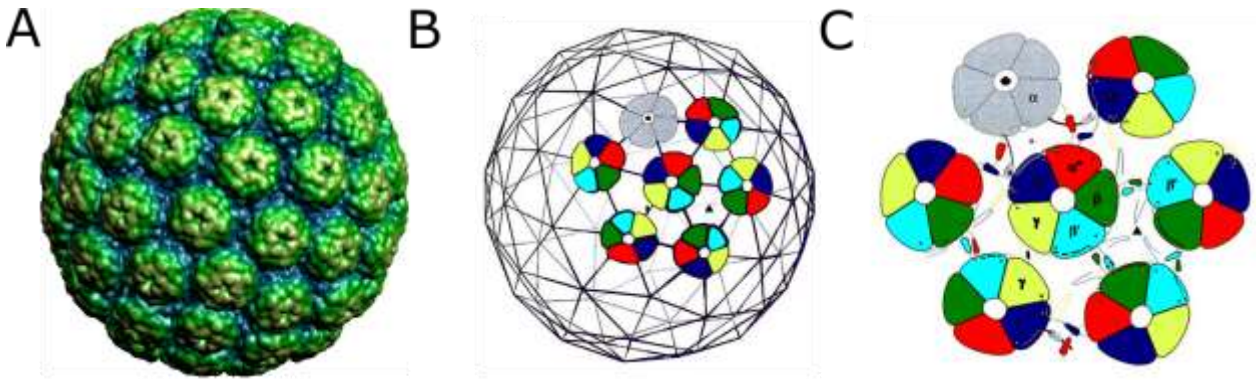

Figure 2: Capsid organization of Polyomaviruses. (A) Full SV40 virion (PDB code 1sva). The figure was obtained from VIPERdb (http://viperdb.scripps.edu) (Carrillo-Tripp et al. 2009). (B) Architecture of the virion shell with the pentamer arrangement on the T=7d icosahedral lattice. Strict pentamers are shown in gray and local pentamers are colored. (C) Interpentamer contacts in the virion. The three different kind of axes (approximate 3-fold axis, approximate 2-fold axis, strict 2-fold axis) are indicated between the corresponding pentamers. Figure panels B and C are adapted from (Stehle et al. 1996).

Polyomaviruses exhibit a rather unexpected capsid organization, with featuring pentamers instead of hexamers in hexavalent positions of the icosahedral capsid. Based on the location in the capsid, two different classes of pentamer can be distinguished: Twelve pentamers lie on the twelve 5-fold rotation axes of the icosahedron, whereas each pentamer is surrounded by five other pentamers, the remaining sixty pentamers do not lie on global symmetry axes and they are surrounded by six other pentamers (Figure 2). The particular orientations of the 5- and 6-coordinated pentamers lead to just three kinds of interpentamer contacts: an approximate 3-fold axis relating subunits labelled α, α' and α''; an approximate 2-fold axis relating those labelled β and β'; and a strict icosahedral 2-fold axis relating those labelled γ (Liddington et al. 1991; Rayment et al. 1982; Salunke, Caspar, and Garcea 1986). The γ-monomers are the only ones that do not exhibit an α-helical segment at the C-terminus. Two helices mediate contacts between monomers β and β', three helices the contacts between α, α' and α'', and contacts between γ-monomers are mediated by flexible non-helical structures (Figure 2). The C-terminal end can either be flexible or form a short antiparallel terminal β-ribbon composed of strands K and L (KL β-ribbon). However, for all pentamers, the invading C-terminal arm of a neighboring pentamer contributes to strand J, which is clamped in place by the β-strand A of the N-terminal arm resulting in a six-stranded β-sheet (AJBIDG2) (Figure 1) (Stehle and Harrison 1996).

Capsomer interactions are further stabilized by disulfide bonds and divalent ions. Whereas the CD-loop can adopt various conformations, a conserved cysteine residue can be found at the tip of the CD-loop. (Stehle et al. 1996; Stehle and Harrison 1996). In SV40, cysteine C104 from the α-subunit contacts VP1 monomers α' and α'' from 6-fold coordinated pentamers to form disulfide bonds with equivalent cysteines. Similarly, this disulfide bridging can be observed for cysteine residues of the CD-loops of the β and β' monomers. Furthermore, inter-pentamer bridges might be formed by cysteines C9 in the C-terminal arms (Stehle et al. 1996; Jao et al. 1999). In MPyV, CD-loop residue C114 is involved in a disulfide bridge with C19 in the N-terminal arm of the counterclockwise VP1 monomer, thus retaining the N-terminal clamp (Stehle and Harrison 1996). Assembly of MPyV VP1 pentamers has been shown to be facilitated by calcium ions (Salunke, Caspar, and Garcea 1986, 1989). In the assembled SV40 capsid, two calcium ion binding sites were identified (Stehle and Harrison 1996). The ions bridge the invading C-terminal arm of one pentamer with core residues of the accepting pentamer (Liddington et al. 1991; Stehle et al. 1996). Hence, Ca^{2+} potentially serves as a trigger at the pentamer interface and the addition or depletion of Ca^2 facilitates capsid assembly or disassembly, respectively (Salunke, Caspar, and Garcea 1986; Kawano et al. 2009). Among different polyomaviruses, both calcium binding sites and cysteine residues are highly conserved. This implies that capsid

assembly, disassembly and stabilization *in vivo* underlie similar principles (Stehle et al. 1996; Stehle and Harrison 1996; Schelhaas et al. 2007; Walczak and Tsai 2011). Hence, treatment with reducing and Ca^{2+}-chelating agents such as EDTA results in the disassembly of SV40, MPyV and other polyomaviruses *in vitro* (Brady, Winston, and Consigli 1977; Kosukegawa et al. 1996; Ishizu et al. 2001).

Minor Capsid Proteins VP2/VP3

VP1 pentamers are generally associated with one molecule of either VP2 or VP3, which overlap in sequence, although the presence and role of the minor capsid proteins can vary among different species (Barouch and Harrison 1994; Gasparovic, Gee, and Atwood 2006; Kawano et al. 2006; Schowalter and Buck 2013). In the absence of these minor capsid proteins, VP1 can self-assemble into virus-like particles with similar structural properties to native virions (Kosukegawa et al. 1996; Gillock et al. 1997). VP2 and VP3 share a common C-terminal sequence with VP2 exhibiting additional residues at its N-terminus. Binding studies have shown that VP1 interacts tightly with VP2/VP3, and that a sequence near the common C-terminus of VP2/VP3 is sufficient for complex formation (Barouch and Harrison 1994). The crystal complex structure of MPyV VP1 with the common C-terminal segment of VP2 (residues 214-318) shows that it binds VP1 mainly through hydrophobic interactions. Yet, salt bridges as well as hydrogen bonds at two positions at the internal region of VP1 are as well involved in interactions within the complex (Chen, Stehle, and Harrison 1998). However, only residues 269-296 are resolved in the electron density map and make contact with three monomers within the pentamer. Sequence alignment of VP2 from different polyomaviruses showed that the only long stretch of highly conserved amino acids is from residues 266-302, containing the region visible in the crystal structure (Chen, Stehle, and Harrison 1998).

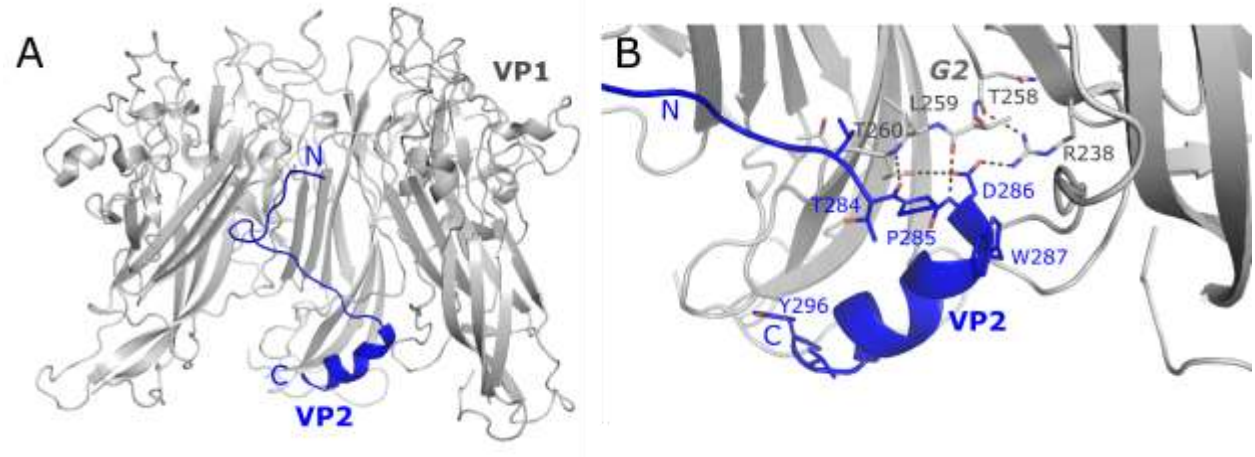

Figure 3: Structure of the VP1 –VP2 complex of MPyV. (A) Open view, displaying VP2 (blue) in its binding site surrounded by three MPyV VP1 monomers shown in grey (PDB code 1CN3). The remaining two monomers are not shown. (B) Interactions between VP1 and VP2 are shown with dashed black lines. Residues of interest are highlighted as sticks.

Previous work on SV40 found that VP3 was dispensable but VP2 was necessary for infection (Cole et al. 1977; Gharakhanian, Munoz, and Mayorca 2003). In contrast, MPyV devoid of VP2 or VP3 were reported to be noninfectious (Mannova et al. 2002). Similarly, for JCPyV both minor proteins are needed for proper propagation of the virus (Gasparovic, Gee, and Atwood 2006). VP2 has been shown to be modified by a myristylation moiety, a co-translational addition of fatty acid, at its N-terminus (Streuli and Griffin 1987; Resh 1999). This myristylation site is important for infection likely due to its interaction with host cell membranes (Krauzewicz et al. 1990; Sahli et al. 1993). During viral infection, VP1 regulates the membrane localization of minor capsid proteins and both VP2 and VP3 post-translationally integrate into ER membranes in the absence of VP1 (Daniels, Rusan, Wadsworth, et al. 2006; Burkert et al. 2014). The efficient transportation of viral DNA into cells is facilitated by VP2 and VP3. Both SV40 and BK minor capsid proteins contain a C-terminal nuclear localization signal (NLS). Mutations of basic residues in this region have been shown to decrease nuclear entry during host cell infection (Nakanishi et al. 2002a; Nakanishi, Itoh, et al. 2007a; Nakanishi, Li, et al. 2007; Bennett et al. 2015a).
In general, the N-terminus of VP2 is more flexible and not as tightly folded as the common C-terminal part of VP2 and VP3, which is responsible for VP1 binding. It has been found that the N-terminal region of VP2 is sensitive to gentle proteolysis (Chen, Stehle, and Harrison 1998). During infection, this part of VP2 would be able to emerge more easily from the inside of the virion and propagate a structural rearrangement. The exact mechanism of the exposure of minor capsid proteins during infection still needs to be further elucidated.

1.2 Virus Glycan Receptors

Interactions between viruses and receptors play a major role in viral host range, tissue tropism and viral pathogenesis. Attachment to one or multiple receptors by viruses is critical to overcome the plasma membrane barrier and to enter the host cell to eventually utilize the host cell machinery. Viral attachment proteins recently were described as “keys” able to unlock the host cells by interacting with the “lock”, the receptor, on the cell surface; interactions that are vital for viruses to successfully enter the host cell (Maginnis 2018). Viruses often rely on particular classes of molecules in order to drive these mechanisms. These can include sialic acid containing carbohydrates, glycosaminoglycans (GAGs) or histo-blood group antigens (HBGAs) (Figure 4).

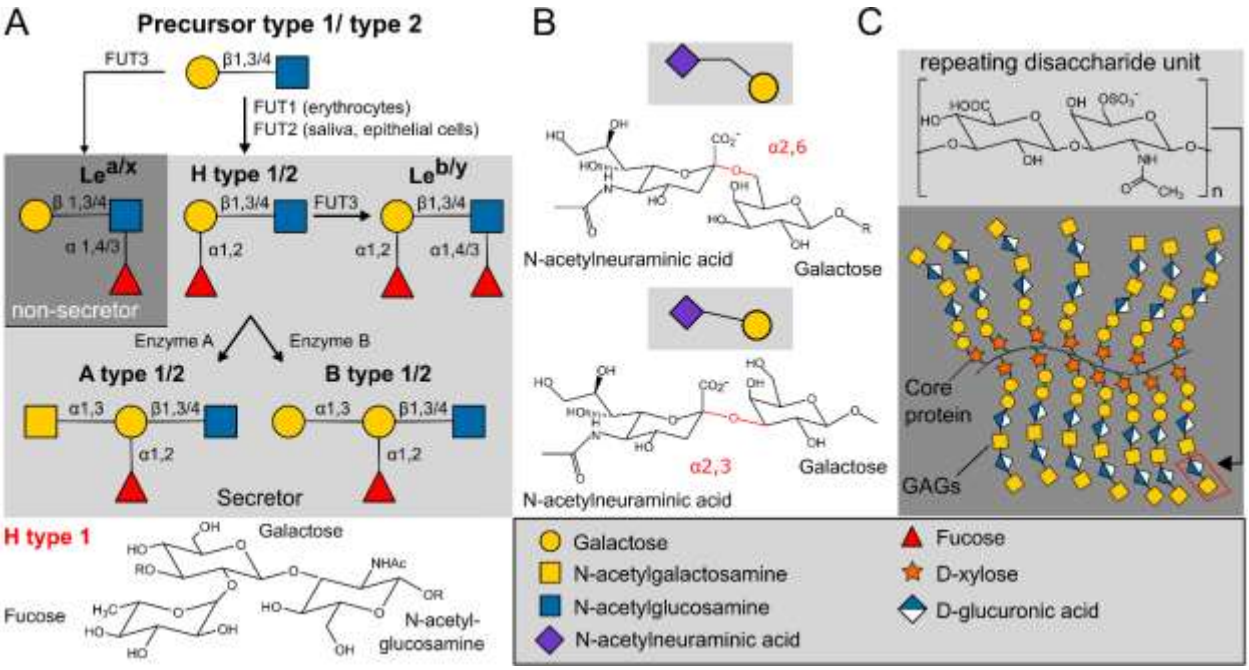

Figure 4: Glycan types that can function as viral receptors. (A) Biosynthesis of human ABH and Lewis HBGAs of type 1 and type 2. The types are defined by the glycosidic linkage of the precursor (type 1 is β1,3 and type 2 is β1,4 linked). Each step of the synthesis is catalyzed by a specific glycosyltransferase. FUT1 and FUT2 gene products control the same reaction. FUT1 is expressed in erythrocytes and FUT2 in secretory tissues giving rise to its glycosidic product in saliva and mucosal secretions. Sequential addition of monosaccharides to the precursor results in secretor-HBGAs in the presence and to non-secretor Lewis types in absence of FUT2 in secretions. FUT3 is primarily expressed in the epithelial cells of gastrointestinal tissue and adds a fucose to the precursor or H-type antigens. Enzyme A or enzyme B adds GalNAc or galactose via α1,3 linkages to H-type antigens, respectively, resulting in A and B type HBGAs. As an example, H type 1 is shown in a structural representation. (B) Sialic acid variants. Sialic acids terminate N- and O-glycans as well as glycolipids. The two common types of linkages, the α2,6- and α2,3- linkage, are shown with the most prominent sialic acid in humans, N-acetylneuraminic acid, and galactose in a structural and schematic representation. The glycosidic linkage is highlighted in red. (C) In general, glycosaminoglycans are composed of repeating identical disaccharide units of N-acetylated or N-sulfated amino sugar linked to uronic acid or galactose. These units form long, unbranched GAG chains connected to a core protein. Depicted is chondroitin sulfate, a sulfated glycosaminoglycan consisting of repeating N-acetylgalactosamine and glucuronic acid units (adapted from (Dietrich, Harprecht, and Stehle 2017)).

Common viral receptors, including for polyomaviruses, are sialylated glycans, which are ubiquitously expressed in higher vertebrates (Stroh and Stehle 2014). Sialic acids, the terminal monosaccharide units on glycan chains of N- and O-linked glycoproteins and glycolipids and are usually part of the recognition site to which viruses attach (Varki and Varki 2007; Wasik, Barnard, and Parrish 2016). Interactions between a viral attachment protein and its glycan receptor primarily involve the sialic acid itself, which is bound with a relatively small contact area in a solvent-exposed region of the protein. Consistently, the binding affinities are typically very low, with dissociation constants in the millimolar range (Neu et al. 2008; Burmeister et al. 2004; Stehle and Harrison 1996; Sauter et al. 1989). In most cases, though, low affinity is overcome by high avidity. Sialic acids consist of a nine-carbon backbone, but show great diversity in their types and linkages and are among the most diverse sugars found on glycan chains of mammalian cell surfaces. The most common modifications can be found at the 4, 5, 7,

8 and 9 positions and involve acetylations, methylations and sulfatations. These different modifications and linkages determine specificity and evolution of viruses has selected for specific interactions with different glycan types. Different modifications occur specifically in eukaryotes, archaea or bacteria and play an important role in the tropism of the virus at the level of host, tissue as well as differentiated cell types (Gee et al. 2006; Wasik, Barnard, and Parrish 2016).

The primary sialic acid forms are determined by modifications at the 5-carbon position, such as N-acetylneuraminic acid (Neu5Ac) or N-glycolylneuraminic acid (Neu5Gc) (Varki and Schauer 2009). Neu5Ac is the most abundant sialic acid in humans and features a carboxylate group at C2, an N-acetyl group at the C5 position and a glycerol chain at position C6. Neu5Gc, which only differs by a single oxygen atom at the C5 position from Neu5Ac, cannot be synthesized in humans due to a mutation causing irreversible inactivation of the gene encoding for cytidine monophosphate-N-acetyl neuraminic acid hydroxylase (CMAH), which hydroxylates Neu5Ac (Chou et al. 1998; Irie and Suzuki 1998; Varki 2001). The loss of Neu5Gc and the accumulation of its precursor Neu5Ac has several implications for humans, including a change in pathogen regimes. Pathogens binding Neu5Gc are no longer able to infect humans, in turn, those binding Neu5Ac would have a special preference for human cells due to the great increase in its density (Varki 2009). Neu5Gc can be incorporated from exogenous sources, the richest sources being red meat and dairy products, and it can even be found in human carcinomas and fetal tissues (Tangvoranuntakul et al. 2003; Varki and Varki 2007; Samraj et al. 2015). Furthermore, all humans have significant levels of circulating antibodies against Neu5Gc (Tangvoranuntakul et al. 2003; Nguyen, Tangvoranuntakul, and Varki 2005; Padler-Karavani et al. 2008; Zhu and Hurst 2002).

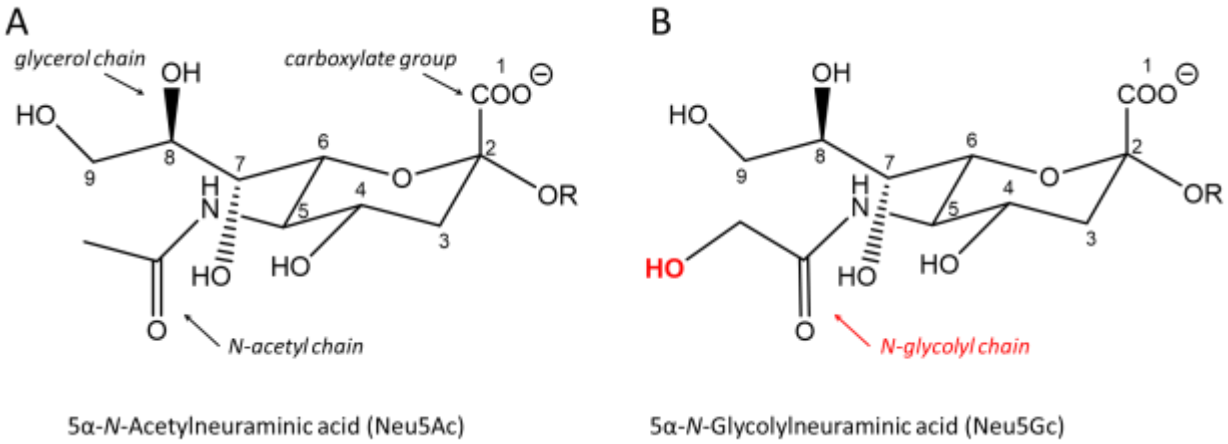

Figure 5: Structures of Neu5Ac and Neu5Gc. (A) Neu5Ac, which features an N-acetyl group at position C5, is the most abundant sialic acid variant in humans. (B) Neu5Gc, which only differs by an N-glycolyl chain instead of an N-acetyl chain from Neu5Ac, is not synthesized in humans due to a mutation of the CMAH gene. Neu5Gc is commonly found in monkeys and other vertebrates. Common functional groups of sialic acids are the carboxylate group, glycerol and N-acetyl or N-glycolyl, respectively, but also acetylations, methylations and sulfatations at positions C4, C5, C7, C8 and C9 of the 9-carbon backbone (Angata and Varki, 2002).

Additional variations in sialic acid forms can be found in glycoconjugates such as N- or O-linked proteins and glycolipids, where sialic acids can be linked via α2,3 and α2,6-linkage to either galactose (Gal) or to *N*-acetylglucosamine. Additionally, sialic acids can be linked to one another via α2,8 and α2,9-linkages (Muhlenhoff, Eckhardt, and Gerardy-Schahn 1998; Varki and Schauer 2009). Gangliosides, a particular type of glycolipids, are classified into four asialo-, a-, b- and c-series gangliosides, based on the number and complexity of their sialic acid branching patterns (Schnaar, Suzuki, and Stanley 2009). They are abundantly expressed in all human tissues and body fluids with varying expression patterns among different types of cells. During brain development, expression levels and patterns change drastically. The predominant gangliosides in embryonic brains are GM3 and GD3, whereas in the adult brain expression levels of these two gangliosides are downregulated and simultaneously, expression levels of GM1, GD1a, GD1b and GT1b are upregulated (Ngamukote et al. 2007; Yu et al. 1988) (Ngamukote et al., 2007). Gangliosides are primarily, but not exclusively, localized in the outer leaflet of plasma membranes. Gangliosides present on the cell surface are involved in cell-cell recognition and adhesion and signaltransduction with cell surface microdomains, such as caveolae (Anderson 1998; Yu et al. 2011). Furthermore, they play an important role in the modulation of intracellular and intracellular calcium homeostasis (Ledeen and Wu 2008). One important factor dictating the host tropism and pathogenicity of different viruses are varying expression patterns of glycan receptors and pseudo-receptors among different tissues.

1.2.1 Polyomavirus Sialic Acid Glycan Receptors

Polyomaviruses rely on carbohydrates as receptors for primary cell attachment and entry. The ability of different polyomaviruses to infect different hosts is determined by discrimination between different sialic acid residues. Although capsids of polyomaviruses all have a very similar structure, they all rely on different receptors (Table 1) (Gee et al. 2006; Liu, Hope, and Atwood 1998; Yan et al. 1996).

Table 1: Cellular components associated with polyomavirus entry.

Polyomavirus	Structural studies	Glycan receptors or glycan receptor motifs	Co-receptors
JCPyV	LSTc (Neu et al. 2010)	• LSTc (Neu et al. 2010) • GM2, GM1 (Leonid Gorelik, Consortium for Functional Glycomics [CFG], available online at hhtp://www.functionalglycomics.org)	5-HT2R (Elphick et al. 2004; Assetta et al. 2013)

		• GD1a, GD2, GD1b, GT1b (Gorelik et al. 2011) • GM3, GD2, GD3, GD1a, GD1b, GT1b, GQ1b (Komagome et al. 2002)	
BKPyV	GD3 (Neu, Allen, et al. 2013) GT1b (Hurdiss et al. 2018)	• GT1b, GD1b (Low et al. 2006) • GD3, GD2, GD1b, GT1b (Neu et al., 2013a)	-
SV40	GM1 (Neu et al. 2008)	• GM1 (Neu et al. 2008; Tsai et al. 2003; Campanero-Rhodes et al. 2007)	MHC class 1 (Atwood and Norkin 1989) AxI (Drayman et al. 2013) α2β1 integrin (Stergiou et al. 2013)
MPyV	3'SL (Stehle et al. 1994) DSLNT (Stehle and Harrison 1996)	• GD1a, GT1b (Tsai et al. 2003)	α4β1 integrin (Caruso et al. 2003)

Receptors for SV40, MPyV

SV40 binds to the MHC class I molecule at the plasma membrane, confirmed by antibodies to MHC class I antibodies, which slightly reduce SV40 infection (Breau, Atwood, and Norkin 1992; Atwood and Norkin 1989). Yet, the MHC molecule is not endocytosed with the virus, signifying the requirement for a specific receptor for transport to the ER and infection of the cells (Anderson, Chen, and Norkin 1998). SV40 was shown to bind to the glycolipid receptor ganglioside GM1 on the cell surface (Tsai et al. 2003; Campanero-Rhodes et al. 2007; Ewers et al. 2010) before internalization and trafficking to the endolysosomes (Engel et al. 2011). Both the Galβ1-3GalNAc and Neu5Ac branches directly contact the major capsid protein VP1 and thus provide binding activity (Neu et al. 2008). In simians, which are the natural host for SV40, GM1 contains a terminal Neu5Gc at the equivalent position like Neu5Ac in humans (Varki 2001). Both GM1 variants can serve as receptors for SV40, although Neu5Gc significantly increases binding (Campanero-Rhodes et al. 2007). GM1 is bound in shallow solvent-exposed portions at the outer surface of the pentamer. This binding pocket is formed by the loops connecting β-strands B and C (BC-loop), D and E (DE-loop) and H and I (HI-loop). These loops show high sequence variability among polyomaviruses, contrasting the otherwise conserved VP1 core structure. This results in high receptor specificity by mediating different contacts to receptors (Neu et al. 2008).

Like SV40, MPyV also binds to ganglioside receptors (Tsai et al. 2003) and both polyomaviruses utilize similar binding locations on the outer surface of VP1. In contrast to SV40, MPyV recognizes GD1a and GT1b as receptors. These gangliosides carry either two (GD1a) or three (GT1b) Neu5Ac residues, which are distributed over two

branches. The part recognized by MPyV VP1 is limited to a terminal Neu5Ac-α2,3-Gal linked structure (Neu et al. 2008; Tsai et al. 2003; Stehle et al. 1994; Stehle and Harrison 1996, 1997; Cahan, Singh, and Paulson 1983). This moiety is also present on the shorter arm of GM1, nevertheless it is too close to the ceramide to be recognized as a receptor by MPyV (Tsai et al. 2003). Nevertheless, MPyV features a high ligand binding promiscuity due the ubiquitous minimal Neu5Ac-α2,3-Gal motif. This has been shown for three closely related prototype strains, which feature high differences in pathogenicity and spread when transfected in new-born virus-free mice (Buch et al. 2015). The three MPyV strains RA, PTA and LID all bind to the established receptors GD1a and GT1b and additionally, with even higher potency, to ganglioside GT1a. However, single changes in the amino acid composition of the viral capsid promote subtle differences in binding affinity resulting in the discrepancy in pathogenicity among different MPyV strains (Buch et al. 2015; Tsai et al. 2003; You et al. 2015).

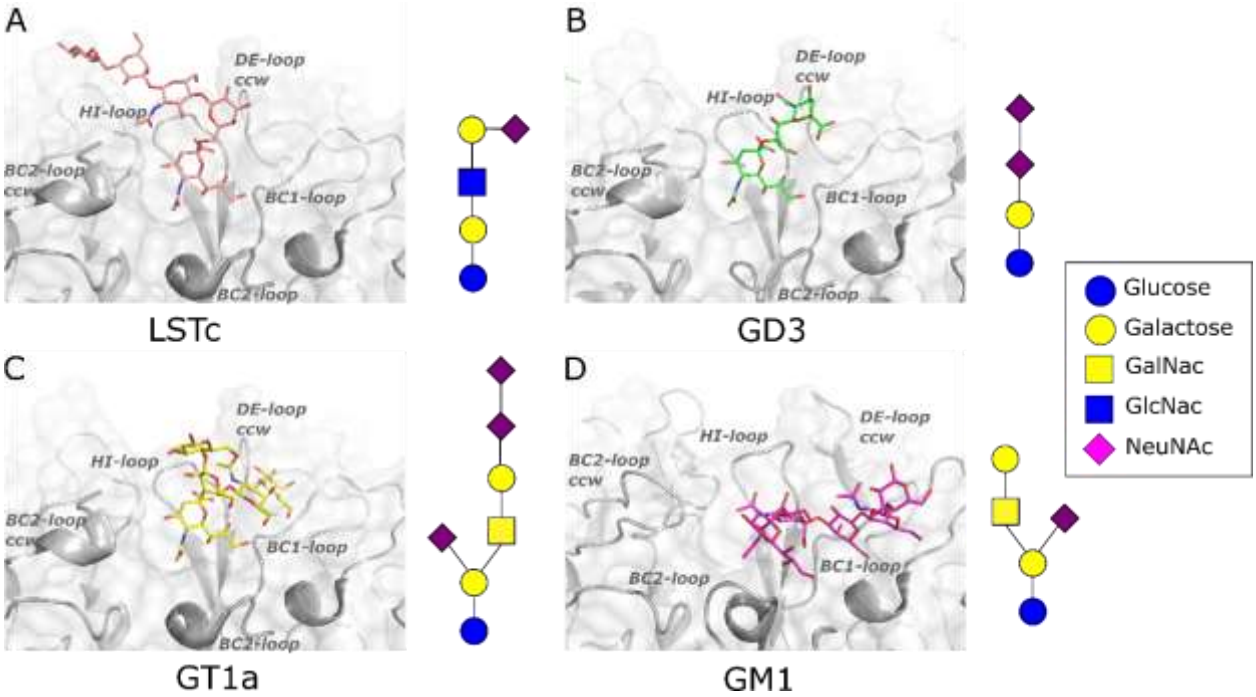

Figure 6: Glycan binding site of JCPyV, BKPyV, MPyV and SV40. (A) JCPyV-LSTc (PDB code: 3NXD), (B) BKPyV-GD3 glycan (PDB code: 4MJ0), (C) MPyV-GT1a glycan (PDB code: 5CPW) and (D) SV40-GM1 glycan (PDB code: 3BWR) complex structures are shown with VP1 in grey surface and cartoon presentation. Loop regions lining the glycan binding site are labeled and glycan are shown in stick presentation with oxygen in red and nitrogens in blue. Schematic presentations of the glycans used in the crystallographic studies are indicated below the structural figures.

Receptors for JCPyV

The cellular host range, which is limited to cells in the kidney, B lymphocytes of the bone marrow and oligodentrocytes and astrocytes in the CNS, is indicative of a more restricted receptor usage for JCPyV than for the more promiscuous polyomaviruses SV40 and MPyV (Gee et al. 2006). Experimental studies with viruses pre-treated with ganglioside GT1b inhibited infection of glial cells indicating that JCPyV can bind

glycolipids and glycoproteins containing sialic acids (Komagome et al. 2002; Gee et al. 2006). Gangliosides may play a role in initial attachment of the virus, act as a second messenger or inhibit the primary receptor (Lloyd and Furukawa 1998; Gee et al. 2006). JCPyV requires the serotonin receptor 5HT2α as the proteinaceous component to infect and enter cells (Elphick et al. 2004). 5HT2αR contains five N-linked glycosylation sites on the extracellular N-terminus, which are not required for successful JCPyV infection (Maginnis et al. 2010). In line with recent results, it has been shown that glycosylation of 5HT2αR is important for receptor expression (Dutton et al. 2008; Monk et al. 2004; Quirk et al. 2004). In prior studies it was also shown that JCPyV infection of glial cells was inhibited by an N-linked glycosylation inhibitor, but not by an O-linked glycosylation inhibitor, indicating that N-linked glycoprotein with terminal α2,6-linked sialic acid is utilized as receptor by JCPyV (Liu, Wei, and Atwood 1998). Biochemical binding analyses demonstrated that JCPyV virus-like particles (VLPs) comprised of VP1 bind to glycoproteins and glycolipids with oligosaccharides containing α2,3-, α2,6- or α2,8-linked sialic acid (Dugan, Gasparovic, and Atwood 2008). VLPs of the laboratory prototype strain Mad-1 bind to oligosaccharides containing α2,3-, α2,6- or α2,8-linked sialic acid including gangliosides GM3, GD2, GD3, GD1b, GT1b and GQ1b with only weak binding to GD1a as shown by a virus-overlay-blotting-assay (Komagome et al. 2002). VLPs of with VP1s of genotype 3 strain WT3 bind to gangliosides containing α2,3- or α2,8-linked sialic acids, including asialo-GM1, GD1a, GD1b, GD2, GT1a and GT1b (Gorelik et al. 2011). WT3 VLPs additionally bind to gangliosides GM1 and GM2 as confirmed by glycan array (Leonid Gorelik, Consortium for Functional Glycomics [CFG], available online at hhtp://www.functionalglycomics.org, according to CFG policy). While Mad-1 VLPs were able to bind to several α2,3-, α2,6- or α2,8-sialic acid-containing structures, the highest affinity was observed for α2,6-sialic acid expressed on lactoseries tetrasaccharide c (LSTc), a linear pentasaccharide expressing a terminal α2,6-sialic acid on glycoproteins and glycolipids (Xu et al. 2009). In glycan array studies, JCPyV VP1 pentamers bound specifically to α2,6-linked sialic acid linked LSTc (Neu et al. 2010). Mad-1 strain VLPs also specifically bind only to LSTc in glycan array studies, indicating that VLPs with 72 copies of VP1 retain the specificity to LSTc and additionally gain avidity (data from CFG). LSTc binds on top of the JCPyV VP1 pentamer, whereas the binding site is formed by residues from the BC-, DE- and HI-loops from one monomer and residues from the BC-loop of the clockwise neighboring monomeric unit (Neu et al. 2010). This mode of binding has already been observed for receptor binding of other polyomaviruses, such as MPyV and SV40. LSTc has a linear sequence of NeuNAc-α2,6-Gal-β-1,4-GlcNAc-β1,3-Gal-β-1,4-Glc and binds to JCPyV VP1 in a specific L-shaped conformation (Breg et al. 1989; Neu et al. 2010). The mode of engagement by JCPyV occurs by a single, terminal sialic acid, which is connected to the remaining oligosaccharide chains via an α2,6-linkage. Both the specific L-shaped conformation and sialic acid contacts are required for attachment of JCPyV (Neu et al. 2010).

α2,6-linked sialic acid was shown to be highly distributed on B lymphocytes in tonsils and the spleen, as well as on oligodendrocytes and astrocytes, cell types that have been shown to be susceptible for JCPyV infection (Padgett et al. 1971; Monaco et al. 1996; Monaco et al. 1998; Eash et al. 2004). The receptor is also expressed in the

lungs and in the kidneys, which may be indicative of the route of transmission and site of persistence in the viral lifecycle (Bofill-Mas et al. 2003; Bofill-Mas and Girones 2003; Monaco et al. 1998; Eash et al. 2004). However, JCPyV infection of neuronal cells might occur by binding to other sialic acid structures, by utilization of an alternate receptor or by a unique entry mechanism such as cell-to-cell spread (Eash et al. 2004).

Whereas the non-pathogenic archetype JCPyV strain, which persistently infects the kidneys and can be found in the urine of healthy subjects, binds to the pentasaccharide LSTc (Neu et al. 2010; Stroh et al. 2015), JCPyV strains found in the serum, cerebrospinal fluid and brains of PML patients often contain mutations in residues lining the LSTc-binding pocket on the apical surface of VP1 (Gorelik et al. 2011; Reid et al. 2011; Sunyaev et al. 2009). These so called PML-type strains contain polymorphic changes in the non-coding control region (NCCR) and thereby convert the virus to the neuropathogenic form (Ferenczy et al. 2012; Frisque 1983; Krebs, McAvoy, and Kumar 1995; Sock et al. 1996). In addition to NCCR rearrangements, 89-90% of viral isolates from the blood and cerebral spinal fluid (CSF) of PML patients exhibit mutations in the JCPyV VP1. The most common mutations are L54F, S266F and S268F/Y (Zheng et al. 2005; Delbue et al. 2009; Sunyaev et al. 2009; Gorelik et al. 2011; Reid et al. 2011). Most of these characteristic PML mutations render the virus incapable of binding LSTc or other sialylated glycans, indicating these strains are under positive selection during the development of PML (Gorelik et al. 2011; Maginnis et al. 2013; Ray et al. 2015; Sunyaev et al. 2009). This prediction is in line with results obtained from a human glial cell-engrafted chimeric mouse model of PML (Kondo et al. 2014). In this mouse model, infection with a native, wild-type JCPyV strain leads to PML-like pathology and, even more importantly, disease progression is characterized by the appearance of viral strains with VP1 mutations lining the LSTc-binding pocket, including some of the characteristic mutations observed in the brains of PML patients (Kondo et al. 2014). Mice challenged with JCPyV carrying either of the two most common PML mutations (VP1 L55F or S269F) showed robust infection of engrafted human oligodendrocytes, astrocytes and glial progenitor cells in vivo and infection occurred at an equivalent or higher frequency compared to wild-type virus. PML-mutant JCPyV strains remain fully infectious in a range of brain cells, although receptor binding is abrogated. Crystallographic studies of JCPyV VP1 pentamers with these mutations do no longer bind to LSTc oligosaccharide, as these mutations block the receptor binding site on the VP1 pentamer (Maginnis et al. 2013). Mutations in these VP1 apical surface loops may allow polyomaviruses to escape from antibody-mediated neutralization (Ray et al. 2015; Pastrana et al. 2013).

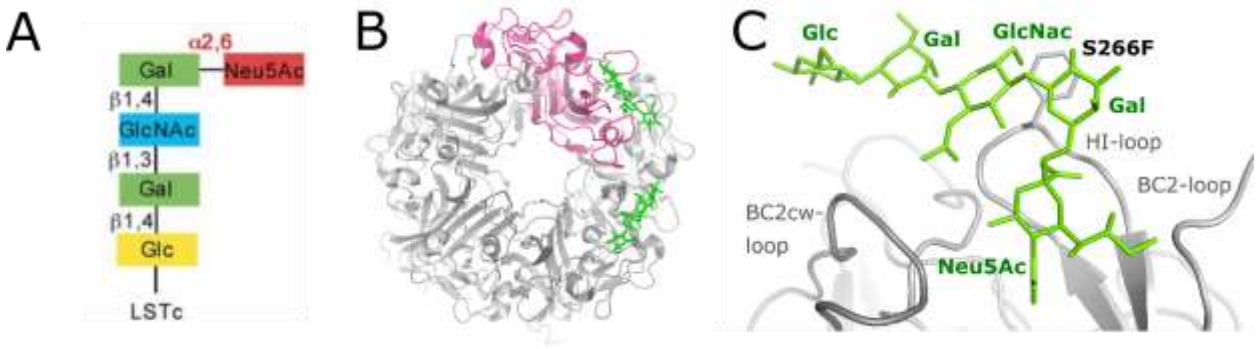

Figure 7: JCPyV VP1 glycan binding. (A) Schematic presentation of the α2,6-linked Neu5Ac glycan LSTc and its characteristic L-shaped conformation. (B) Top view of the JCPyV VP1 pentamer in complex with LSTc (PDB code 3NXD). The pentamer is shown in cartoon presentation with one monomer highlighted in pink. LSTc is shown in green stick presentation. (C) Close-up view of the LSTc binding site. JCPyV VP1 is shown in cartoon presentation with the neighboring monomer in a darker grey. The binding site is formed by the variable surface loops connecting the β-strands of the jelly-roll core. One of the characteristic PML-associated mutations, S266F, is shown in sticks. The introduction of the rather bulky residue in the receptor binding site would cause sterical clashes.

Receptors for BKPyV

BKPyV binds to α2,3-linked sialic acid, and it has been shown that gangliosides GD1b and GT1b are utilized for attachment and infectious entry into renal proximal tubular epithelial cells. However, in functional cell-based and structural studies it was demonstrated that the common α2,8-disialic acid motif on gangliosides is recognized as primary epitope for binding of BKPyV. BKPyV infection efficiency has been shown to be increased by b-series gangliosides GD3, GD2, GD1b and GT1b (O'Hara et al. 2014; Neu, Allen, et al. 2013). The increased affinity towards these more complex b-series gangliosides only partially dictate receptor usage. Another factor, which counteracts low binding affinity, is a greater receptor abundance on host cells resulting in higher avidity (Neu, Allen, et al. 2013). BKPyV probably engages a mixture of gangliosides on the cell surface for attachment and entry. The virus persistently resides in the kidney and here cells are particularly rich in more simple gangliosides, such as GM3 and GD3 (Shayman and Radin 1991). The relative abundance of gangliosides differs not only between the kidney and the brain, there is also significant variation between expression levels of different tissues in the adult kidney (Holthofer, Reivinen, and Miettinen 1994; Yu, Nakatani, and Yanagisawa 2009). BKPyV latency and reactivation might be influenced by developmental and drug-induced changes in ganglioside distribution (Neu, Allen, et al. 2013). Recently, structural studies of BKPyV gave rise to speculations that BKPyV interacts with glycosaminoglycans (GAGs) (Hurdiss et al. 2018). Structural evidence is missing so far; however, one possibility is that GAGs bind to the pore of the VP1 pentamer, where they also would be in close proximity to the minor capsid proteins VP2 and VP3. The lack of VP2 and VP3 in pseudoviruses renders them less efficient in transducing a range of different cell types (Schowalter and Buck 2013).

Similarly as for JCPyV, BKPyV also features neutralization-escape mutations in the major capsid protein VP1, which can alter the spectrum of sialylated glycans the virus engages for infection (Peretti et al. 2018). BKPyV strain IV, which is associated with post-transplant nephropathy (BKVN), has been shown to establish dominant

mutations, one common mutation being E73Q, in the major capsid protein VP1. These mutations render the virus partially resistant to the patient's immune response and potentially trigger altered tissue tropism and pathogenicity similarly to VP1 mutations in JCPyV (Peretti et al. 2018; Jelcic et al. 2015; Geoghegan et al. 2017).

1.2.2 APMAP – A Putative JCPyV Receptor

The adipocyte plasma membrane-associated protein APMAP was identified as putative receptor for JCPyV in pull-down assays (Atwood group, unpublished results).
APMAP, or C20orf3 derived from the gene location on open reading frame 3 encoded at human chromosome 20 (Deloukas et al. 2001; Albrektsen et al. 2001), represents a member of the lactonohydraolase super family. Protein expression of APMAP was demonstrated in the liver, glomerular and tubular structures of the kidney, as well as endothelial cells and arterial wall. The transcript coding for 416 amino acids is ubiquitously found in adult as well as in embryonic tissues, whereas in adult tissues the highest expression is found in the liver, placenta and the heart (Ilhan et al. 2008).
APMAP has been shown to interact with extracellular collagen cross-linking matrix protein oxidase-like 1 and 3, indicating its role as a novel regulator of extracellular matrix components (Albrektsen et al. 2001; Bogner-Strauss et al. 2010). The protein was shown to play an important role in the adipose differentiation process and expression is highly upregulated during adipogenic differentiation of various murine and human cell lines (Bogner-Strauss et al. 2010). Studies showed that APMAP expression was significantly decreased in omental adipose tissue from gestational diabetes mellitus (GDM) patients. The protein plays an important role in insulin resistance in GDM as was shown by the down-regulation of APMAP in 3T3-L1 adipocytes, which resulted in the activation of the inflammatory NFκB pathway and an impaired insulin signaling pathway in those adipocytes (Ma et al. 2016).
Additionally, APMAP is an endogenous inhibitor of amyloid-beta (Aβ), a major pathological hallmark of Alzheimer's disease, production in the brain. This function is mediated by the ability to bind both amyloid precursor protein (APP) and γ-secretase and by controlling the levels and the stability of APP-C-terminal fragments (APP-CTFs). APMAP impairs the formation of Aβ by co-localizing at least partially with γ-secretase and its substrate APP (Mosser et al. 2015). In mice, APMAP knockdown in both neuronal and glial cells increased Aβ levels in the hippocampus by 20-55%. According to a molecular hypothesis, APMAP would promote the transport of APP-CTFs from the endosomes to the lysosomes with the consequence being their degradation, thus reducing both APP-CTFs and Aβ levels. The delivery of APP-CTFs can be carried out via the endosomal-lysosomal pathway (heterophagy) or the authophagic pathway causing the degradation of the Aβ precursor proteins; thus, depletion of APMAP would lead to impaired degradation with the consequence of increased APP-CTFs and Aβ levels (Mosser et al. 2015).
APMAP encodes a 416 amino acid single-pass type-II glycosylated membrane protein that is implicated in the regulation of white adipocyte tissue differentiation. The protein exhibits a small N-terminal anchor (residues 1-40) and a predicted six-bladed β-propeller extracellular domain (residues 62-415), which displays a potential hydrolase activity and is involved in calcium binding (Bogner-Strauss et al. 2010). The protein

possesses two amino acid modifications with an N-acetylserine at position 2 and a phosphothreonine at position 16. Furthermore, position 160 and 196 feature two predicted glycosylation sites. The Asn196 glycosylation is exclusively present in humans (Albrektsen et al. 2001; Bogner-Strauss et al. 2010).
The human-specific glycosylation site together with the involvement in the endosomal-lysosomal pathway raise the possibility of APMAP being a potential receptor for JCPyV.

1.3 The Life Cycle of Polyomaviruses

The attachment of the virus particle to the host cell initiates the polyomavirus life cycle. This interaction induces virus internalization, followed by intracellular trafficking via early, maturating and late endosomes to the endoplasmatic reticulum lumen for initial uncoating and to the nucleus for viral gene expression and replication of the viral genome, and finally ends with the assembly and release of progeny virions (Figure 8). Vital for viral transcription and replication is the delivery of DNA into the nucleus. One major obstacle for viruses is to overcome the membrane barrier from the outside of the cell or an endocytic compartment in the cytosol. Enveloped viruses employ membrane-fusion in order to target their genome into the cell. Nonenveloped viruses, such as polyomaviruses have to engage other mechanisms to overcome this obstacle. Penetration of the membrane barrier often is accomplished by a series of conformational changes of the viral particle. In many cases, these changes are facilitated with the help of cellular factors. Polyomaviruses use caveolae-, lipid-raft and clathrin-mediated pathways for cell entry (Eash, Querbes, and Atwood 2004; Gilbert and Benjamin 2000; Gilbert, Goldberg, and Benjamin 2003; Moriyama and Sorokin 2008; Pelkmans and Helenius 2002).

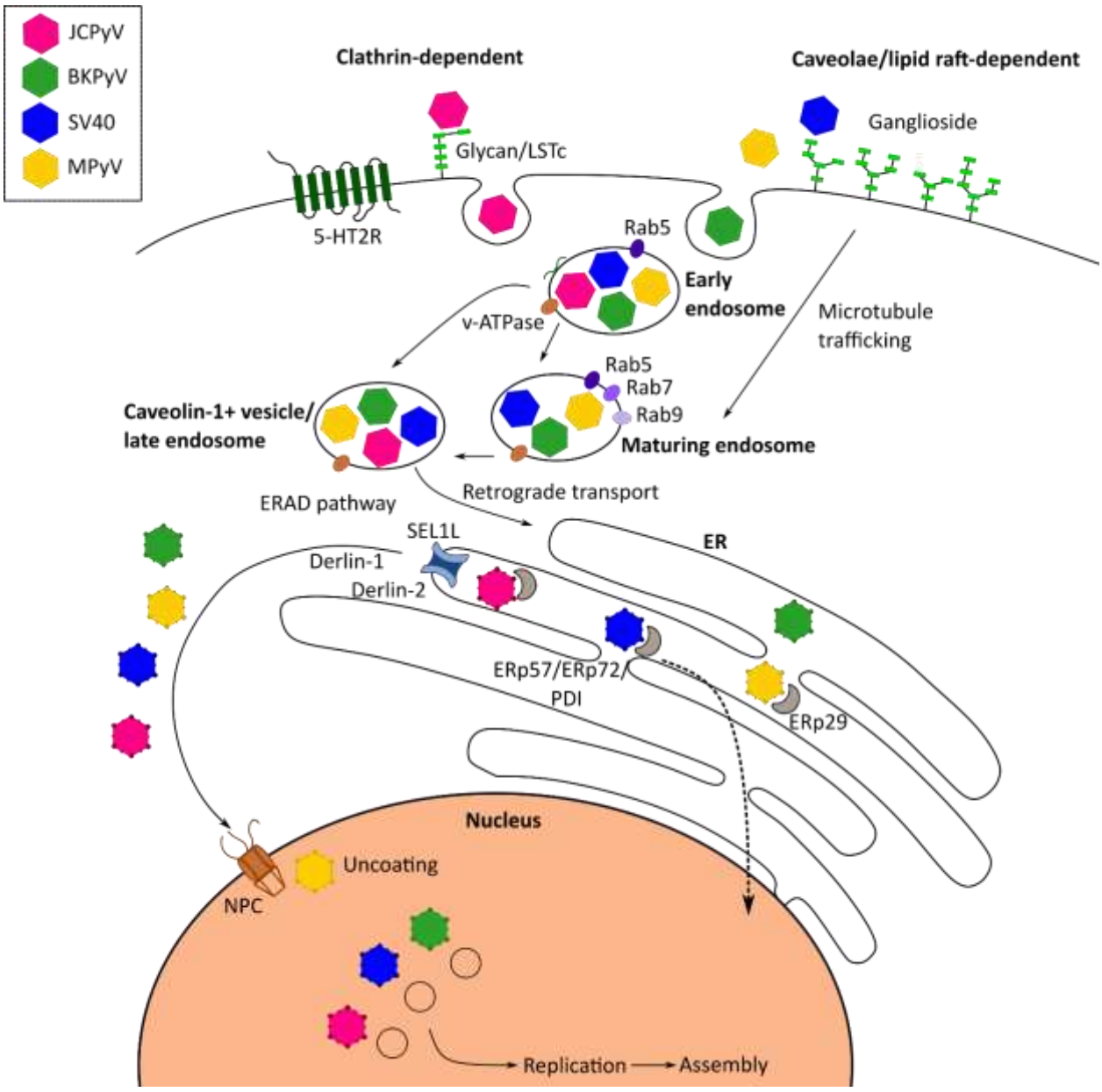

Figure 8: Schematic representation of polyomavirus infectious entry pathways. BKPyV, SV40 and MPyV enter cells via a caveolae-/lipid raft-dependent pathways, JCPyV utilize clathrin-dependent endocytosis. Polyomaviruses traffic to the ER for partial uncoating and then to the nucleus for replication and virus progeny.

1.3.1 Cell Entry of SV40, MPyV and BKPyV

SV40, MPyV and BKPyV enter cells via caveolae- and lipid raft-dependent endocytosis (Gilbert and Benjamin 2000; Eash, Querbes, and Atwood 2004; Gilbert and Benjamin 2004). Caveolae are lipid-raft-rich, flask-shaped, 50 – 100 nm invaginations present in the plasma membranes that are stabilized by VIP-21 or caveolins and contain mainly cholesterol and sphingolipids (Rothberg et al. 1992). Internalization of viruses is mediated by multivalent binding of the virus particle to

ganglioside receptors present on the outer leaflet of the plasma membrane, which induces a curvature of the membrane. This produces a tight-fitting invagination containing one virion (Tsai et al. 2003; Low et al. 2006; Ewers et al. 2010). In the case of SV40 and numerous other polyomaviruses, trafficking to the ER directly results from ganglioside binding and cholesterol-dependent endocytosis (Qian et al. 2009). Gangliosides do not only play an important role in cell surface binding, but also in the intracellular trafficking of polyomaviruses. The virus most likely stays attached to the gangliosides from the plasma membrane all the way to the ER as indicated by the isolation of gangliosides from ER fractions (Tsai et al. 2003).

Upon host cell attachment, polyomaviruses bind to more than one ganglioside due to the low affinity of an individual binding site in order to establish stable binding (Szklarczyk et al. 2013). Additionally, virus particles may recruit even more gangliosides during transport to the endolysosomes, clustering multiple molecules of gangliosides on the viral capsid during the transport process (Qian et al. 2009). This clustering might help in targeting the viral particle to the ER as has been shown for pentameric toxins such as cholera toxin (Wolf et al. 2008). Transport to the ER is a vital step for viral infection as blocking ER-resident factors such as ERp29 drastically decreases infection (Magnuson et al. 2005; Gilbert et al. 2006). In the following steps of the infectious entry, polyomavirus particles are transferred to maturing endosomes, late endosomes and endolysosomes via microtubules and microfilaments (Gilbert and Benjamin 2004; Eash and Atwood 2005; Qian et al. 2009; Zila et al. 2014).

Initially, studies suggested that SV40 and MPyV enter cells in so-called caveosomes, CAV1-rich, pH-neutral intracellular organelles (Pelkmans, Kartenbeck, and Helenius 2001). CAV1 belongs to the family of integral membrane protein and is a key component of caveolae (Williams et al. 2004). Recently, studies no longer considered caveosomes as independent organelles but rather modified late endosomes or endolysosomes in which forms of CAV1 accumulate after overexpression or after interference with caveolaer assembly (Hayer et al. 2010; Engel et al. 2011). Polyomaviruses colocalize with several endosomal Rab proteins, such as Rab5, which belong to a family of small GTPases and regulate membrane trafficking through effector protein recruitment (Querbes et al. 2006; Qian et al. 2009; Engel et al. 2011). Rab5 plays a role in formation, transport and fusion of vesicles to early endosomes, whereas Rab7 and Rab9 are markers of late endosomes. Internalized SV40 and MPyV viral particles have been found in Rab5-, Rab7-, as well as Rab9-positive endosomes. Furthermore, these viruses associate with the lysosomal-associated protein 1 (LAMP1), a marker of the endolysosomes (Engel et al. 2011; Qian et al. 2009). Conformational changes in the polyomavirus capsid are pH-dependent and acidification of endosomes and lysosomes is induced by the vacuolar ATPase (v-ATPase) (Qian et al. 2009; Engel et al. 2011). The following retrograde trafficking to the ER is vital for polyomavirus infection. Most extracellular ligands were found to be recycled at the plasma membrane after endocytosis rather than being transported to the ER (Querbes et al. 2006; Nelson et al. 2012).

After trafficking to the ER, the viral particle engages host-cell chaperones and protein disulfide isomerases (PDI) resulting in destabilization of the viral capsid. ERp29, ERp57, ERp72, the canonical PDIs and possibly ERdj5 catalyze the disruption of disulfide bonds, which stabilize the viral capsid. This results in partial exposure of VP2

and VP3 (Magnuson et al. 2005; Rainey-Barger, Mkrtchian, and Tsai 2007; Schelhaas et al. 2007; Nelson et al. 2012; Inoue et al. 2015). Polyomaviruses thus hijack a machinery in the ER that is normally responsible for the identification of misfolded proteins and for retro-translocation of these proteins through the ER membrane (Schelhaas et al. 2007; Lilley et al. 2006). Different polyomaviruses engage unique compositions of PDI proteins, which might result from differences in the disulfide network of the capsid (Gilbert et al. 2006; Walczak and Tsai 2011). The exposure of the hydrophobic and myristylated amino-terminal sequence of VP2 anchors the virus to the ER membrane possibly by insertion of a hydrophobic VP2 segment into the ER membrane. Hsp70 family member BiP in concert with the J-domain of the DNAJB11 are recruited to the newly-generated hydrophobic viral particle, which is prone to aggregation (Rainey-Barger, Mkrtchian, and Tsai 2007; Geiger et al. 2011; Goodwin et al. 2011; Dupzyk and Tsai 2018). Both BiP and DNAJB11 participate in ER-associated degradation (ERAD), a quality control process that removes misfolded proteins from the ER into the cytoplasm, where proteosomal degradation occurs (Goodwin et al. 2011; Gilbert et al. 2006; Vembar and Brodsky 2008; Lilley et al. 2006). BKPyV, SV40 and MPyV have been shown to interact with ERAD pathway after localization to the ER, which results in retrotranslocation of the virus to the cytoplasm (Inoue et al. 2015; Jiang et al. 2009; Lilley et al. 2006; Schelhaas et al. 2007). Members of the ERAD pathway such as Derlin-1 (Schelhaas et al. 2007), Derlin-2 (Lilley et al. 2006), SEL1 (Schelhaas et al. 2007), RMA1 and BAP29/BAP31 (Geiger et al. 2011) regulate the retrotranslocation to the cytoplasm. Furthermore, the cytosolic chaperone SGTA (small glutamine-rich tetratricopeptide repeat-containing protein α) is critical for transport of the virus from the ER membrane into the cytosol. SGTA associates with a chaperone complex of the J-proteins DnaJB14 (B14) and DnaJB12 (B12) at the ER membrane and is therefore positioned to act at the site of membrane penetration. During membrane penetration SGTA is released from the B14-B12 complex, which is reorganized into discrete foci in the ER membrane. These foci might act as ER exit sites for the virus (Goodwin et al. 2011; Walczak and Tsai 2011).

Nuclear translocation of polyomaviruses occurs through the nuclear pore complex (NPC). The transport depends on the interaction of the nuclear localization signal (NLS) of VP1 and minor capsid proteins VP2 and VP3 with cellular importins, namely importin α and importin β (Qu et al. 2004; Nakanishi et al. 2002b; Nakanishi, Itoh, et al. 2007b). More recently it has been shown that nuclear entry of SV40 mainly depends on the interaction of the NLS of minor capsid proteins with importins rather than interaction with the NLS of VP1 which is bound to the viral minichromosome (Bennett et al. 2015b). Entry of the nucleoplasm might also be possible directly from the ER by crossing the inner nuclear membrane by deformation (Butin-Israeli et al. 2011). Further downstream in the viral replication cycle, capsid proteins are produced in the cytoplasm and transported into the nucleus, where they accumulate in nuclear domain 10 (ND10) bodies for assembly into virions (Ishov and Maul 1996; Shishido-Hara et al. 2004). ND10 bodies, or also promyelocytic leukemia (PML) protein nuclear bodies are heterogeneous nuclear scaffolds, which are suggested to be sites of polyomavirus replication. These tubular structures with “budding” events at the end, which were termed “polyomavirus assembly factories”, represent assembly sites of progeny virions, although the loss of the PML protein itself seems not critical for this process

(Erickson et al. 2012). VP1 pentamers presumably polymerize into tubes around the viral chromatin or the chromatin later traverse into until eventually icosahedral particles bud off at the end. How the viral genome is identified and bound by the VP1 subunits remains unknown (Oppenheim et al. 1992; Dalyot-Herman et al. 1996; Carbone et al. 2004; Erickson et al. 2012). After assembly, agnoprotein together with VP2 and VP3 are mainly responsible for the necrosis resulting from polyomavirus infection by enhancing membrane permeability, which is required for the release of progeny virions (Suzuki et al. 2010; Daniels, Rusan, Wilbuer, et al. 2006). Agnoprotein itself is a regulatory protein required for efficient proliferation of the virus.
Noteworthy are the striking similarities between the polyomavirus trafficking to the ER and the ER targeting of pentameric bacterial toxins, such as cholera toxin or shiga toxin, which have been extensively studied (Ewers and Helenius 2011; Johannes and Popoff 2008; Johannes and Wunder 2011; Tsai and Qian 2010). These toxins traffic to the ER by attaching to gangliosides and relying on cholesterol-dependent endocytosis similar to MPyV, SV40 and BKPyV and other polyomaviruses. Furthermore, these toxins can also induce membrane curvature (Ewers et al. 2010; Romer et al. 2007), implying the orientation of oligosaccharide binding sites and their distance to one another on the pentamers promotes membrane invaginations. One major difference in the ER trafficking of polyomaviruses and bacterial toxins is that polyomaviruses are usually not found in the trans-Golgi network or the Golgi complex. This has also been observed for JCPyV, albeit with its different receptor usage (Engel et al. 2011; Nelson et al. 2012).

1.3.2 Cell Entry of JCPyV

Unlike for SV40, BKPyV and MPyV, infectious cell entry of JCPyV proceeds by clathrin-dependent endocytosis. This indicates that the endocytic pathway taken by different polyomaviruses is dictated by the engagement of the respective cell surface and entry receptor. JCPyV selectively binds to the oligosaccharide lactoseries tetrasaccharide c (LSTc) to attach to host cells and initiate infection (Neu et al. 2010). After viral attachment, entry is facilitated by the engagement of 5-hydroxytryptamine $(5\text{-HT})_2$ family of serotonine receptors via clathrin-dependent endocytosis (Elphick et al. 2004; Maginnis, Nelson, and Atwood 2015). 5-HT2Rs are transmembrane-spanning G protein-coupled receptors that are widely expressed on a variety of cell types, including brain cells such as glial cells and kidney cells, correlating with infection sites of JCPyV (Bonhaus et al. 1995). The expression of 5-HT2Rs on cells is not sufficient to drive JCPyV infection, conversely overexpression of these receptors does not affect the viral attachment to LSTc (Assetta et al. 2013). Serotonin inhibitors, such as chlorpromazine, clozapine or ketanserin reduce JCPyV infection in glial cells (Elphick et al. 2004; O'Hara and Atwood 2008), the same effect has been shown for 5-HT2AR and 5-HT2CR antibodies. Consistently, overexpression of 5-HT2Rs in poorly permissive cell lines enhances JCPyV infection (Elphick et al. 2004; Maginnis et al. 2010).
Recently it was shown that β-arrestin plays a major role in JCPyV internalization. Arrestins, a small protein family important for the regulation of signal transduction of G protein-coupled receptors, interact with 5-HT2AR and direct the receptor to the

clathrin-coated pit with the assistance of proteins including clathrin and adaptor protein 2 (AP2) (Gray and Roth 2001; DeWire et al. 2007; Smith et al. 2016). Inhibition of β-arrestin drastically reduced JCPyV internalization and infection (Mayberry et al. 2019). JCPyV infection is also reduced in glial cells and the kidney cell line HEK293 by the drug chlorpromazine, an inhibitor of clathrin-dependent endocytosis and antagonist of 5-HT2Rs, further indicating that viral entry is mediated clathrin-dependent uptake (Pho, Ashok, and Atwood 2000; Assetta et al. 2013; Maginnis, Nelson, and Atwood 2015).

Following receptor engagement on the cell surface, JCPyV is internalized by clathrin-dependent endocytosis involving 5-HT2Rs, β-arrestin and epidermal growth factor pathway substrate clone 15 (Eps-15), a clathrin adaptor protein (Pho, Ashok, and Atwood 2000; Querbes et al. 2004; Assetta et al. 2013; Mayberry et al. 2019). In the endocytic system, JCPyV co-localizes with Rab5 as soon as 15 min post-infection and 2 hours post-infection with Cav-1 (Querbes et al. 2006). Rab7, which plays an important role in endosomal maturation, co-localizes with several polyomaviruses such as SV40 and BKPyV, but has not been found to co-localize with JCPyV. This indicates that JCPyV does neither enter maturing endosomes nor endolysosomes (Querbes et al. 2006; Qian et al. 2009; Qian and Tsai 2010; Engel et al. 2011). It remains unclear whether the association between JCPyV and Cav-1 occurs in distinct endosomal compartments or in Cav-1-positive late endosomes (Querbes et al. 2006; Nelson et al. 2012). Recycling endosomes probably do not play a role in JCPyV infection, as deficiency of Rab11 has no effect on infectivity. Unlike other polyomaviruses, which engage ganglioside receptors for attachment and entry, differences in endosomal accumulation most likely occur due to different receptor usage of JCPyV. Nevertheless, large parts of intracellular pathways of JCPyV resemble those of other polyomaviruses. Although JCPyV rapidly accumulates in endosomes, ER accumulation of JCPyV virions occurs after 6 hours post-infection, comparable to the transport kinetics of SV40 (Schelhaas et al. 2007; Nelson et al. 2012). In the ER, JCPyV undergoes conformational changes induced by local proteins such as PDI, ERp57 and ERp72, which leads to the exposure of VP2. Mutations in the pore of the VP1 pentamer prevent the exposure of VP2 and hence inhibit infection (Nelson et al. 2015). The capsid size is only slightly changed upon ER entry and the size of viral particles ranges from 35 to 45 nm in diameter as has been shown for SV40 infection (Dupzyk and Tsai 2016). JCPyV particles can enter the nucleus after exiting the ER and gaining access to the cytosol. Notably, during no time at the entry process does JCPyV co-localize with the Golgi unlike seen for bacterial toxins like cholera toxin (Nelson et al. 2012). Golgi localization can be influenced by several factors: the different receptor usage for JCPyV, which binds to the receptor motif LSTc rather than GM1 for cholera toxin. Another factor might be avidity, which is much lower for single pentameric units than for complete virus particles. The higher avidity interaction of virus particle and receptor might lead to direct ER trafficking. Another reason for direct ER trafficking might be the sheer size of virions compared to cholera toxin (Nelson et al. 2012).

1.4 Antiviral Strategies

1.4.1 Antibodies

With polyomavirus infections being ubiquitous in the population worldwide, there is also a high prevalence of antibodies against the different species (Knowles 2006; Stolt et al. 2003; Barbanti-Brodano et al. 2006). Especially JCPyV and BKPyV infect the majority of the population, yet only few people will develop diseases arising from these polyomavirus infections, which will only arise in the presence of an compromised immune system (Diotti et al. 2013). For JCPyV, the occurrence of PML was very rare before the era of HIV and the application of immunomodulatory therapies for diseases like MS, suggesting that infection is well controlled by the immune system in healthy individuals.

Antibodies against both JCPyV and BKPyV are present in about 80% of the population with almost no region worldwide being free of anti-PyV antibodies (Brown, Tsai, and Gajdusek 1975; Hamilton, Gravell, and Major 2000; Hariharan et al. 2005; Knowles et al. 2003; Randhawa et al. 2006).

For children and newborns though, JCPyV antibody seroprevalence data are limited, with values ranging from 11 to 16% between 1 and 3 years of age (Chang et al. 2002; Stolt et al. 2003; Sroller et al. 2014). It was shown that the amount of JCPyV-specific IgG increased until the third month of life and then decreased until the sixth month. This might be explained by the fact that infants lose maternal antibodies during their first months of life and may become susceptible to primary JCPyV infection occurring between within the first three and six months of life. Following, there is a constant stimulus for antibody production against viral antigens since JCPyV establishes a lifelong infection of the host. By the age of ten, almost 65 - 90% of the children have acquired antibodies against JCPyV and about 90% of adults are seropositive for JCPyV antibodies (Knowles 2006).

The spreading infection of JCPyV and development of PML might be blocked in the critical time window opening after viral reactivation, which results in the transition of virus from the kidney to the CNS. After the virus enters the CNS, three events must occur in order to develop PML, the host immune system must be compromised, the viral NCCR must undergo changes allowing for increasing viral transcription and replication and DNA binding factors that bind to recombined NCCR sequence motif need to be present or upregulated in infected hematopoietic cells, B cells or glial cells (Diotti et al. 2013). The viral transition from the kidney to the CNS could be used for intervening with the spreading infection. Usually, this is accomplished by the constant presence of serum antibodies, which are sustained by persistent production from long-lived plasma cells and recurring immune activation of memory B-cells (Lindner et al. 2019). A minority of healthy JCPyV-seropositive subjects are deficient in serum antibodies capable of neutralizing JCPyV carrying characteristic PML mutations. Some individuals might show an unusually low diversity of plasma cells secreting effectively neutralizing antibodies, so that single point mutations in VP1 allow for virus neutralization escape.

Whether a humoral response is protective against PML strongly depends on the presence of JCPyV VP1 mutations, which are frequently found in addition to prototype

Mad-1 sequences in the CNS of PML patients (Gorelik et al. 2011; Reid et al. 2011). The characteristic PML mutations L54F, S266F and S268F might influence antibody responses and cause 'antibody recognition holes', which play an essential role in PML. These recognition holes are characteristics for PML patients, who fail to produce antibodies recognizing their 'own' mutant (Ray et al. 2015). Specific antibodies against JCPyV hence are vital in controlling JCPyV infection and presumably also in clearing the virus from the brain after PML onset. Impairment of T cell-mediated immunity in the CNS would probably lead to increased fitness of the virus, so antibody-mediated neutralization serves as last line of defense against neuropathic JCPyV replication.
Virus-neutralizing antibodies are characterized by their capability to inhibit virus infectivity by direct binding to the antigen *in vitro*. They can block viral infection either by interfering with attachment of the virus to the host cell or by preventing post-attachment events that would lead to successful infection. These antibodies typically bind to exposed surfaces on viral capsids with high affinity.
In a recent study, a panel of JCPyV VP1-specific, neutralizing monoclonal antibodies (mAbs) has been isolated directly from donors, including patients who successfully recovered from PML or PML-IRIS, respectively (Jelcic et al. 2015). These mAbs showed high specificity and affinity towards JCPyV, neutralized JCPyV infection in vitro and additionally exhibited cross-reactivity against the most common PML mutations. Noteworthy is that some of these mAbs were also able to bind to the closely related BKPyV. Some of these mAbs were structurally characterized to gain insights into the underlying mechanisms of mAb binding and neutralization of JCPyV and BKPyV. These antibodies exhibit varying affinities towards JCPyV, but also in their cross-reactive capacities towards characteristic PML-mutations.

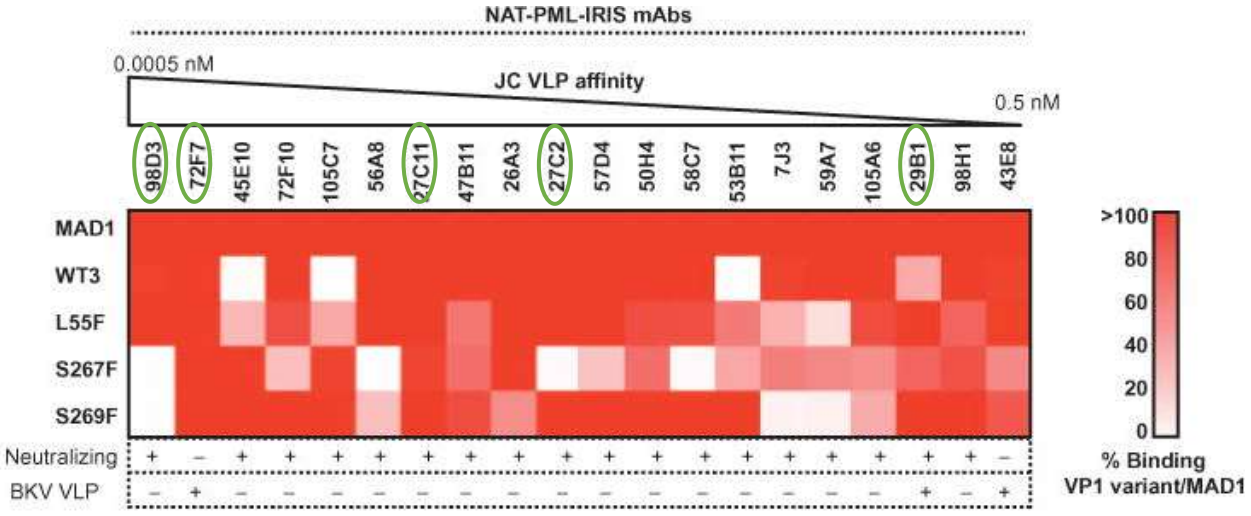

Figure 9: Binding profiles of isolated human monoclonal antibodies to JCPyV VP1 variants. Heat map of binding capacities of mAb towards JCPyV variants like JCPyV Mad-1 or WT3, as well as towards characteristic PML-mutations. Indication of neutralizing capacity and cross-reactivity towards BKPyV. Figure taken from Jelcic et al., 2015. Reprinted with permission from AAAS. Antibodies selected for JCPyV complex formation and crystallization are highlighted with green circles.

For structural studies of JCPyV VP1–antibody complexes, the antibodies were either produced as antibody fragment-antigen binding (Fabs) or single-chain fragments

(scFvs). Both antibody fragments can be obtained from whole antibodies. Antibody molecules consist of three equal-sized parts, which are loosely connected by a flexible tether and display an overall Y-shape. The most common type of serum antibodies in humans with about 75% is Immunoglobulin G (IgG). IgG antibodies are composed of four peptide chains with a total molecular weight of 150 kDa. They consist of two different kinds of polypeptide chain, the heavy chain of approximately 50 kDa and the light chain of approximately 25 kDa. Each IgG molecule is comprised of two heavy and two light chains, whereas the heavy chains are linked to one another via disulfide bonds. Furthermore, each heavy chain is linked to a light chain via another disulfide bond. The two heavy and light chains are identical, hence each antibody molecule harbors two identical antigen-binding sites (Figure 10). The antibody structure features three equal-sized parts, which are connected by a flexible hinge region. The trunk of the Y-shaped structure is composed of the carboxy-terminal halves of the heavy chains. The association of a light chain with the amino terminal half of a heavy chain make up each arm of the Y-shaped structure. Limited proteolysis with papain can cleave the antibody into three fragments. The fragments containing the antigen-binding activity are called Fragment antigen binding, Fab fragments, whereas each Fab fragment consists of the complete light chains together with the V_H and C_H1 domain of the heavy chains. Genetic engineering allows the construction of another antibody fragment, which consists of only the variable domains of heavy and light chain, which are joined by a flexible linker. This construct is called single-chain Fragment variable, or short scFv.

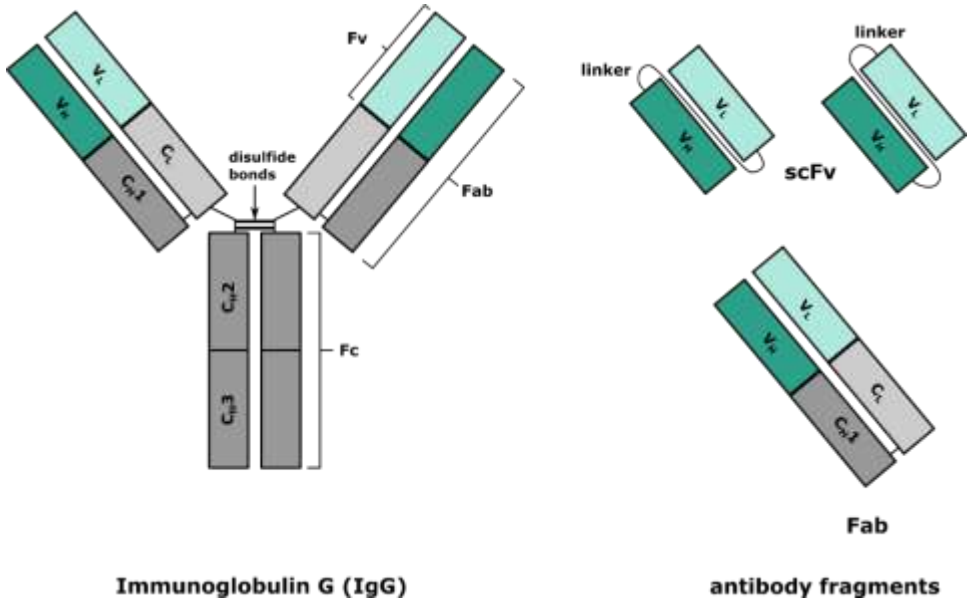

Figure 10: Schematic representation of an antibody (IgG) and antibody fragments (Fabs, scFvs). The most prominent member of antibodies is immunoglobulin G (IgG). The structure of an IgG antibody consists of two heavy chains (H) and two light chains (L). The two antibody halves are held together via disulfide bonds in the hinge region. The antibody fragment-antigen binding (Fab) can be obtained via proteolytic cleavage at the hinge region. Each heavy and light chain consists of a variable domain (Fv), V_H and V_L, which are colored in dark and light cyan, respectively, and a constant domain (C_H1 – C_H3 and C_L) shown in dark and light grey, respectively. The multiple heavy-chain constant regions are numbered starting from the N-terminal end of the carboxy-terminus.

The variable regions of the heavy and light chains can be fused together in two different orientations via linker to form single-chain variable fragments (scFvs).

Antibodies 98D3 and 27C2 were produced as Fabs in order to set up JCPyV-antibody complexes and determine their crystal structure. Antibody 27C11 was purified as scFv for structural characterization by x-ray crystallography. The first two antibodies were purified and characterized by Dr. Luisa Ströh, 27C11 by Felix Nagel and Dr. Luisa Ströh.

JCPyV VP1-Fab as well as scFv complexes consist of five copies of antibody fragments bound to a single JCPyV VP1 pentamer, signifying that each VP1 monomer is involved in identical interactions with the antibody fragments. All antibody binding sites cluster on top of the JCPyV VP1 pentamer overlapping with the LSTc binding site, albeit relying on different individual interactions. The binding interface covered by the antibodies ranges from 707 (98D3) to 981 Å^2 (27C11) and covers two neighboring VP1 monomers for all three studied antibodies (Figure 11).

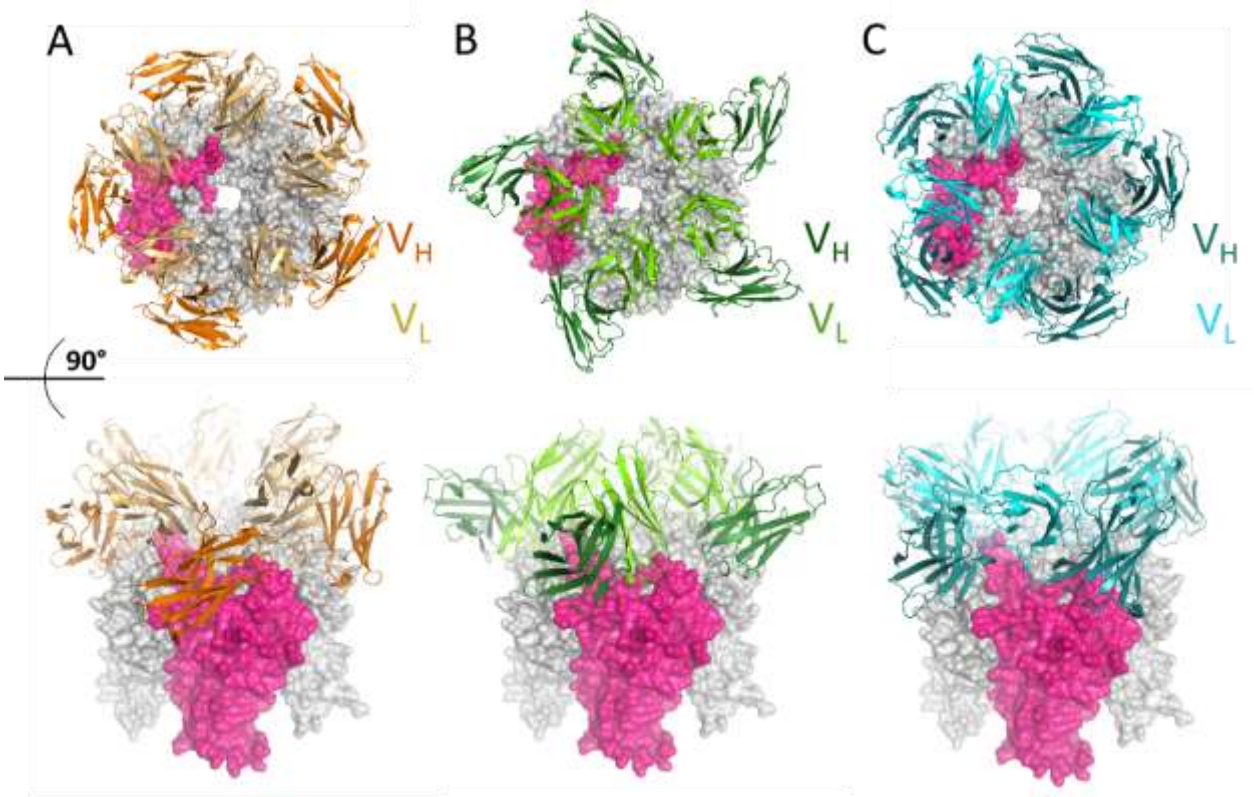

Figure 11: Overview of JCPyV VP1 antibody complexes. Surface representation of JCPyV VP1 pentamers with one monomer highlighted in pink. (A) JCPyV VP1 bound to antibody fragment 98D3 shown in cartoon representation, (B) bound to antibody fragment 27C2 and (C) antibody fragment 27C11. Darker and lighter colors represent heavy (V_H) and light chain V_L of the respective antibody (98D3: green, 27C2: blue, 27C11: orange). Constant chains of Fabs 98D3 and 27C2 (panel A and B) are not shown for better visualization. The bottom panels depict side views of the same structures.

1.4.2 Fragment-based Drug Discovery

Fragment-based drug discovery (FBDD) has been a powerful tool for discovering drug leads since the last two decades. A combination of random screening and structure-based rational drug design is applied, whereas the most common used characterization approaches in FBDD include NMR, x-ray crystallography and surface plasmon resonance (Hartshorn et al. 2005). In order to identify drug-like starting points for inhibitor design, small compounds are tested in a fragment screen. The affinity of these fragments is usually quite low with affinities in the mM range; nevertheless, fragment affinity can be enhanced in later steps. In analogy of Lipinski's 'rule of five' (Lipinski et al. 2001; Lipinski 2004), compounds now are supposed to apply to the 'rule of three' (molecular weight < 300 Da, cLogP value (clogP, a measure of lipophilicity) < 3, the number of hydrogen donors and acceptors < 3 and the number of rotatable bonds < 3). Furthermore, the solubility in water should be increased in order to screen at higher compound concentrations. Several approaches can be undertaken for a fragment screen; one early experimental approach being the co-crystallization of the target protein with organic solvents. These solvents explore hydrophobic pockets of the protein, which are often targeted by drug-like molecules (Ringe 1995). Later on, screening was performed with fragments ranging from 150 to 300 Da in size due to their low complexity and increased binding likelihood. Fragment-based NMR screening almost completely replaced this method due to its low false positive rate and high sensitivity (Edfeldt, Folmer, and Breeze 2011; Hajduk, Huth, and Fesik 2005). In ligand-observed NMR, fragments are screened against a target protein and changes in NMR observables such as chemical shift, line width and signal intensity are monitored upon binding. Fluorine-labeled fragments were shown to be useful due to the low abundance of fluorine in biological samples, which prevents the perturbation by background resonances. Furthermore, the fluorine spin is highly sensitive to changes in the chemical environment and hence, can easily be detected.

Fragment-based screening experiments were performed using ^{19}F and transverse relaxation time (T2)-filtered NMR methods in collaboration with Dr. Christoph Rademacher (Max Planck Institute of Colloids and Interfaces, Potsdam). Both methods are 1D ligand-based approaches, which rely on the chemical shift changes of the ^{19}F nucleus upon altering local chemical environments (Jordan et al. 2012; Chen et al. 2013; Dalvit, Fagerness, et al. 2003; Dalvit, Ardini, et al. 2003). All compounds selected for screening with JCPyV VP1 from the library consisting of about 300 low molecular weight compounds contained a monofluoro or trifluoromethyl group for the heteronuclear ^{19}F detection. In case of a positive binding to JCPyV VP1, a shift of the characteristic compound peak can be observed in the 1D NMR spectrum compared to the compound spectrum obtained without JCPyV VP1. In total, both NMR methods resulted in 40 double positive hits, which were subjected to crystal soaking experiments with JCPyV Mad-1 VP1 crystals. Ten compounds were already tested in preliminary work done by Dr. Luisa Ströh (Figure 12).

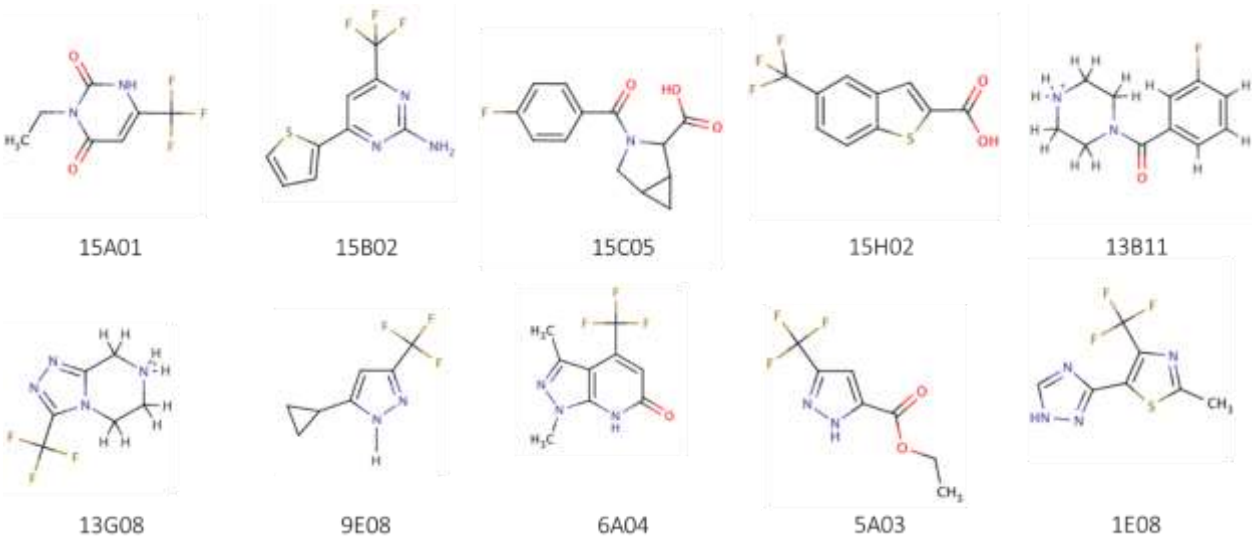

Figure 12: Fragments used for crystal soaking experiments (Part 1). Depicted are 10 out of 40 double-positive hits identified by 19F and T2-filtered NMR spectroscopy. The screening experiments were performed and analyzed by Dr. Christoph Rademacher and Jonas Aretz (Max Planck Institute of Colloids and Interfaces, Potsdam). The figure was prepared using ChemDraw 18.0 (PerkinElmer, Inc.).

Out of the tested compounds, one was shown to bind to JCPyV VP1. The compound 9E08 was shown to bind towards the inner side of the pentamer, with one compound binding to each VP1 monomer. The binding site is located next to β-strands E, F and the ccw G1 strand of the core CHEFG sheet.

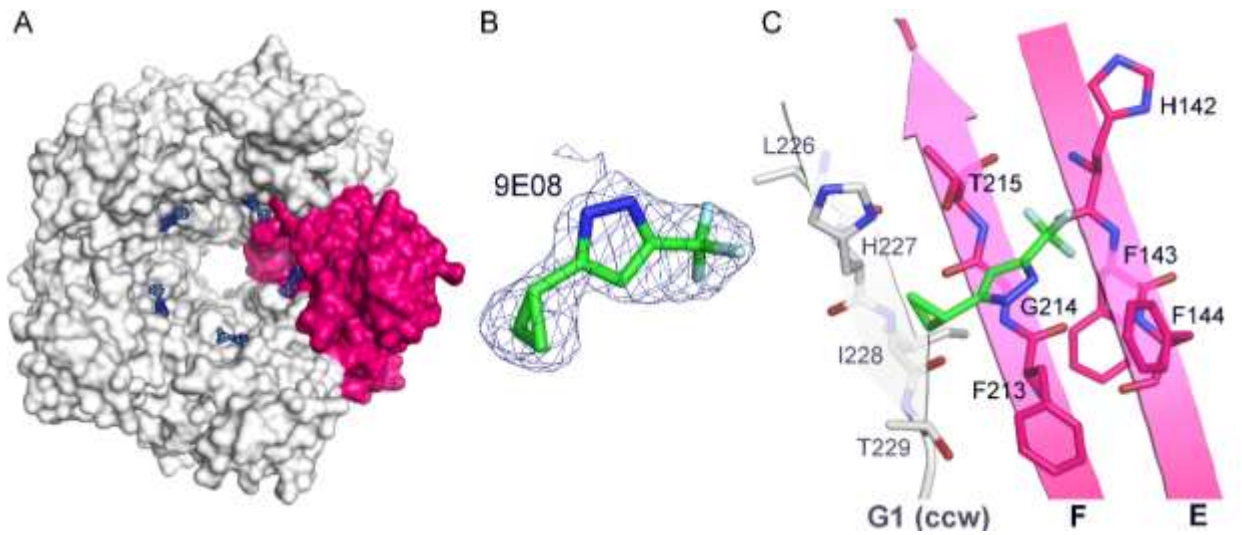

Figure 13: Binding details of compound 9E08 to JCPyV VP1. (A) View from the bottom of the JCPyV pentamer along the five-fold axis. One VP1 monomer is highlighted in pink. Each VP1 monomer binding site is occupied with compound 9E08. (B) The simulated annealed omit electron density map is contoured it at a σ level of 2.5 with a distance of 2Å around the ligand 9E08. (C) β-sheets E, F and the ccw G1 form the binding site for 9E08. The compound 9E08 is shown in stick representation, with carbons in green, nitrogens in blue and fluor in light blue (Figure prepared by Luisa Ströh).

2. Objectives

The focus of this thesis was the structural investigation of the JCPyV VP1 protein in complex with potential inhibitors, namely molecular fragments and neutralizing antibodies, and a putative JCPyV receptor, APMAP. JCPyV VP1 is responsible for binding to host cell-receptors. The protein harbors exquisite glycan receptor specificity and represents the target of the neutralizing antibody response.
Interactions between JCPyV VP1 and its cellular receptor LSTc are well studied, whereas only limited information is available about the putative JCPyV receptor APMAP. To date, little is known about neutralizing antibodies against JCPyV, in particular their mode of VP1 engagement and how they inhibit JCPyV infection. So far, no efficient cure is available for pathogenic JCPyV infection and the development of small molecule inhibitors against JCPyV VP1 would help in the advancement of potent drugs.
At the beginning of this study, high resolution structures were available for JCPyV VP1 alone as well as in complex with three neutralizing antibodies. However, structural information was missing for cross-neutralizing antibodies. The major objectives of this thesis were to:

- Establish a purification protocol for the cross-neutralizing antibodies 29B1 and 72F7
- Identify the epitope of antibodies 29B1 and 72F7
- Define the interactions of these antibodies with JCPyV VP1 as well as BKPyV VP1 on a structural basis to gain insights on the basis of neutralization
- Examine how JCPyV VP1 variants escape neutralizing antibody neutralization
- Identify potent small molecule inhibitors against JCPyV VP1
- Define the interactions of these compounds on a structural basis in order to develop new compounds with higher binding affinities
- Establish a purification protocol for the putative JCPyV receptor APMAP to allow for the structural analysis of this protein and to enable the characterization of JCPyV-APMAP complexes.

3. Materials and Methods

3.1 Chemicals

All chemicals used in this work were of analytical reagent grade and obtained from Roth (Karlsruhe, Germany), Sigma-Aldrich (Deisendorf, Germany), Merck (Darmstadt, Germany), GE Healthcare (Uppsala, Sweden), Molecular Dimensions (Newmarket, UK) and Hampton Research (Aliso Viejo, USA).

3.2 Bacterial Strains

The *Escherichia coli* (*E. coli*) strain XL 10 gold (Stratagene, USA) was used for amplifying plasmid DNA. Proteins were produced in *E. coli* BL21 (DE3) (Novagen, Darmstadt, Germany), SHuffle T7 Express (New England Biolabs, Inc., USA), Arctic Express (DE3) (Agilent Technologies, USA) and LEMO21 (DE3) (New England Biolabs, Inc., USA).

Table 2. *E. coli* strains.

***E. coli* strain**	**Genotypes**
XL 10 gold	endA1 glnV44 recA1 thi-1 gyrA96 relA1 *lac Hte Δ*(mcrA)183 Δ(mcrCB-*hsdSMR-mrr*)173 tet^R F'[proAB $lacI^qZ\Delta M15$ *Tn10*(Tet^R Amy Cm^R)]
BL21 (DE3)	F^- *ompT gal dcm lon* $hsdS_B(r_B^-m_B^-)$ λ(DE3 [*lacI lacUV5-T7p07 ind1 sam7 nin5*]) [$malB^+$]$_{K\text{-}12}$(λ^S)
Arctic Express (DE3)	F^- *ompT* hsdS(rB^- mB^-) dcm^+Tetrgalλ(DE3) endA Hte [cpn10 cpn60 Gentr]
LEMO21 (DE3)	*fhuA2 [lon] ompT gal (λ DE3) [dcm]* Δ*hsdS/ pLemo*(Cam^R) *λ DE3 = λ sBamHIo ΔEcoRI-B int::(lacI::PlacUV5::T7 gene1) i21 Δnin5*

3.3 Plasmids

Table 3.

Plasmid	**Resistance**	**Specifications**	**Origin**
pET-15b	Amp	T7 promotor, N-terminal His_6-tag, thrombin cleavage site, MCS	Novagen, Germany
pET-28a	Kan	T7 promotor, N-terminal His_6-tag, thrombin cleavage site, MCS	Novagen, Germany
pET-52b	Amp	T7 promotor, C-terminal Strep-tag II, HRV 3C cleavage site, C-terminal His_{10}-tag, thrombin cleavage site, MCS	Novagen, Germany

3.4 Commercial Crystallization Screens

Table 4. Commercial crystallization screens.

Screen	Company
Crystal Screens I, II	Hampton Research, Aliso Viejo, USA
Wizard I, II, III, IV	Emerald BioSystems, Bainbridge Island, USA
JCSG	Molecular Dimensions, Suffolk, UK
PEGIon	Hampton Research, Aliso Viejo, USA

3.5 Molecular Biology

3.5.1 Glycerol Stocks

E. coli culture glycerol stocks were prepared by mixing 500 µL of a bacterial overnight culture with 500 µL sterile filtered glycerol solution (50% v/v). The solutions were flash frozen in liquid nitrogen and stored at -80 °C.

3.5.2 Purification of Plasmid DNA

Plasmid DNA from *E. coli* cultures was isolated using the commercial miniprep kit (Promega, Mannheim, Germany) following the manufacturer's protocol. The final concentration of the purified DNA was determined with a Nanodrop using the absorbance at 260 nm (Nanodrop ND-1000, Thermo Fisher Scientific, Waltham, USA).

3.5.3 Transformation of Competent Bacteria Cells

Plasmid DNA was transformed into bacterial cells by adding 100 ng plasmid DNA to 50 µL competent bacteria cells and incubating the mixture for 20 min on ice. Afterwards, cells were heat-shocked at 42°C for 15 s followed by a 5 min incubation on ice. After addition of 950 µL of SOC medium, cells were grown at 37°C (30°C for *E. coli* SHuffle) at 450 rpm for 1 h. 100 µL of the cell suspension were spread on LB-Agar plates containing the corresponding antibiotic.

LB medium	**LB-Agar medium**	**SOC medium**
1% (w/v) tryptone	1% (w/v) tryptone	2% (w/v) tryptone
0.5% (w/v) yeast extract	0.5% (w/v) yeast extract	0.5% (w/v) yeast extract
1% (w/v) NaCl	1% (w/v) NaCl	10 mM NaCl
	6% Agar	2.5 mM KCl
		10 mM $MgCl_2$
		10 mM $MgSO_4$
		20 mM glucose

3.6 Microbiology Methods

3.6.1 Cultivation of *E. coli*

For setting up overnight cultures, 10 – 20 mL of LB medium supplemented with the corresponding antibiotic were inoculated with either bacteria from glycerol stocks, a single bacteria colony from bacterial selection plates or 500 µL transfection solution. Cultures were incubated at 37°C (30°C for *E. coli* SHuffle) overnight and subsequently used to inoculate 100 mL LB medium for test expression experiments and 1 - 4 L of LB medium for recombinant protein production (ratio 1:100). LB medium was supplemented with the corresponding antibiotic. Bacteria were grown to an OD_{600} of 0.6 – 0.8, before expression of target genes was induced with 0.4 – 0.8 mM IPTG. Bacteria grew 4 h – overnight after induction at 20°C and 110 rpm before they were harvested.

3.6.2 Cell Harvesting

Cells were harvested by centrifugation at 9200 g for 15 min at 4°C. Cell pellets were flash frozen in liquid nitrogen and stored at -80°C.

3.7 Protein Biochemistry

3.7.1 Discontinuous SDS-Polyacrylamide Gel Electrophoresis (SDS-PAGE)

SDS-PAGE was used to separate protein samples according to their molecular weight in an electrical field and to analyze protein purity. SDS-PAGE gels consisting of a separating gel with 12% SDS and a stacking gel with a 4% SDS content were cast. Samples were prepared by mixing with 4x SDS-sample buffer, heating them to 95°C for 2 – 5 min with a final centrifugation step at 14000 g for 2 min (Eppendorf centrifuge). Electrophoresis was set for 70 min at 150 V. Gels were stained in InstantBlue Protein Stain (Expedeon, Heidelberg, Germany) for up to 24 h on an orbital shaker.

Table 5. Composition of gels for SDS-PAGE.

4x SDS gels	4% stacking gel	12% separating gel
H_2O (mL)	6.1	5
1.5 M Tris pH 6.8 (mL)	2.5	
1.5 M Tris pH 8.8 (mL)		3.75
10% (w/v) SDS (µL)	100	150
30% Acrylamide-bisacrylamide (mL)	1.4	6
TEMED (µL)	10	7.5
10% (w/v) APS (µL)	100	150

Table 6. Composition of SDS sample buffer (4x).

4x SDS Sample Buffer
20 mL 1 M Tris pH 6.8

10 mL 10% SDS
1.63 mL 0.5 M EDTA pH 8.0
4 mL β-mercaptoethanol
20 mg bromophenol blue

3.7.2 Expression Test

Overnight cultures were added to 100 mL LB medium containing the respective antibiotics in a ratio of 1:10. Cells were grown to an OD_{600} of 0.6 – 0.8 at 37°C (30°C for *E. coli* Shuffle) before expression of target genes was induced with 0.2 – 1 mM IPTG. After induction, 1 mL samples were taken after 1h, 2h, 4h and overnight. The OD_{600} was determined before samples were centrifuged at 16,870 g for 5 min (Eppendorf centrifuge). The supernatant was discarded, and pellets were resuspended in a 1:1 ratio of lysis buffer 12 (Table 7) and sample loading buffer with respect to the determined OD_{600} value (OD_{600} of 1.0 equals 100 µL total resuspension volume). Samples were analyzed by SDS-PAGE.

3.7.3 Buffer Screening

For resuspension of 2 g of cell pellet (wet weight), 15 mL buffer A_{His} were used. The solution was divided into 1 mL aliquots and centrifuged at 16,870 g for 10 min at 4°C (Eppendorf centrifuge). The supernatants were discarded, and pellets were resuspended in 1 mL of lysis test buffers (Table 7). After sonification with an amplitude of 30% for a total pulse time of 30 s (0.5 s pulse on, 2.0 s pulse off) cells were centrifuged again at 16,870 g for 10 min at 4°C (Eppendorf centrifuge). Supernatants were analyzed by SDS-PAGE.

Table 7. List of lysis buffers for solubilization tests.

Lysis Buffer	Buffer Condition
1	100 mM Tris, pH 7.6; 10% glycerol
2	100 mM Tris, pH 7.6; 50 mM LiCl
3	100 mM KH_2PO_4, pH 4.3; 2.5 mM $ZnCl_2$
4	100 mM HEPES, pH 7.0; 100 mM KCl; 1% Triton- X-100
5	100 mM KH_2PO_4, pH 6.0; 50 mM $(NH_4)_2SO_4$
6	100 mM Tris, pH 8.2; 50 mM NaCl; 100 mM Urea
7	100 mM HEPES, pH 7.0; 100 mM Na-glutamate; 5 mM DTT
8	100 mM sodium acetate, pH 5.5; 1 M $MgSO_4$
9	100 mM HEPES, pH 7.0; 1 mM $MgSO_4$
10	100 mM Triethanolamine, pH 8.5; 50 mM LiCl; 20 mM imidazole
11	30 mM Tris, pH 7.5; 300 mM NaCl
12*	15 mM Tris, pH 6.6, 2% urea; 2.5% glycerol; 1% SDS
E	50 mM NaH_2PO_4; 300 mM NaCl; 10 mM imidazole; 1 mg/mL lysozyme
F	100 mM Tris, pH 8.2; 150 mM NaCl; 100 mM urea; 2.5% glycerol; 20 mM imidazole

* Solubilization buffer

Table 8: List of detergent-containing lysis buffers for solubilization tests.

Lysis Buffer	Buffer Condition
1	100 mM Tris, pH 8.2; 50 mM NaCl; 5% isopropanol
2	100 mM Tris, pH 8.2; 50 mM NaCl; 10% isopropanol
3	100 mM Tris, pH 8.2; 50 mM NaCl; 50 mM urea
4	100 mM Tris, pH 8.2; 50 mM NaCl; 1 M urea
5	30 mM Tris, pH 7.5; 300 mM NaCl; 20 mM imidazole; 0.1% NLS
6	30 mM Tris, pH 7.5; 300 mM NaCl; 20 mM imidazole; 0.5% NLS
7	30 mM Tris, pH 7.5; 300 mM NaCl; 20 mM imidazole; 0.1% Triton X-100
8	30 mM Tris, pH 7.5; 300 mM NaCl; 20 mM imidazole; 0.5% Triton X-100
9	30 mM Tris, pH 7.5; 300 mM NaCl; 20 mM imidazole; 1.0% Triton X-100
10	30 mM Tris, pH 7.5; 300 mM NaCl; 20 mM imidazole; 0.1% sodiumcholate
11	30 mM Tris, pH 7.5; 300 mM NaCl; 20 mM imidazole; 0.5% sodiumcholate
12	30 mM Tris, pH 7.5; 300 mM NaCl; 20 mM imidazole; 1.0% sodiumcholate
13	30 mM Tris, pH 7.5; 300 mM NaCl; 20 mM imidazole; 0.1% SDS
14	30 mM Tris, pH 7.5; 300 mM NaCl; 20 mM imidazole; 0.5% SDS
15	30 mM Tris, pH 7.5; 300 mM NaCl; 20 mM imidazole; 1.0% SDS
16	30 mM Tris, pH 7.5; 300 mM NaCl; 20 mM imidazole; 0.6% NLS
17	30 mM Tris, pH 7.5; 300 mM NaCl; 20 mM imidazole; 0.4% NLS
18	30 mM Tris, pH 7.5; 300 mM NaCl; 20 mM imidazole; 0.3% NLS
19	30 mM Tris, pH 7.5; 300 mM NaCl; 20 mM imidazole; 0.2% NLS

3.7.4 Cell Lysis

For resuspension, 5 – 10 mL of lysis buffer were used per g of cell pellet. The solution was supplemented with one EDTA-free Protease Inhibitor Cocktail tablet (Sigma Aldrich, Deisendorf, Germany) and 2 – 5 µL of Benzonase (Sigma Aldrich, Deisendorf, Germany). Cells were lysed by three cycles of sonification with an amplitude of 40% and an overall pulse time of 2 min (0.5 s pulse on, 0.5 s pulse off). Afterwards, cells were centrifuged at 34, 540 g for 40 min at 4°C. The supernatant was sterile filtered with a 0.22 µm filter.

3.7.5 Refolding of Inclusion Bodies

The cell pellet was resuspended in lysis buffer (Table 9) and left under agitation for 12 h at 4°C before lysis. After lysis, the suspension was centrifuged at 16,870 g for 30 min at 4°C. The pelleted inclusion bodies were resuspended and washed twice with 15 mL of buffer 1, buffer 2 and buffer 3. After each wash step, the suspension was centrifuged again at 16,870 g for 30 min at 4°C. After the last centrifugation step, the pelleted inclusion bodies were resuspended in 15 mL guanidium-HCl and left under agitation for 48 h at 4°C. The solubilized protein solution was centrifuged once more before half of the supernatant was added dropwise into 285 mL of refolding buffer over the course of one hour. After 12 hours, the remaining supernatant was added to the refolding buffer and the solution was allowed to slowly stir for 48 h at 4°C. Afterwards,

the total volume was concentrated to 70 mL in Amicon Ultra Centrifugal filter units (Merck, Darmstadt, Germany). The protein solution was dialyzed overnight in 2 L of dialysis buffer in spectral pore dialysis membranes (Spectrum Labs, Sancho Dominguez, USA). The protein solution was sterile filtered (0.22 µm) before being subjected to further purification steps, e.g. Ni-affinity chromatography.

Table 9: List of buffers used for protein refolding from inclusion bodies.

Protein	Buffer	Composition
APMAP	Lysis buffer	100 mM Tris-HCl, pH 8.0 2 mM EDTA 10 mM DTT 0.5 mg/mL lysozyme
	Buffer 1	50 mM Tris-HCl, pH 8.0 1 mM EDTA 1 mM DTT 100 mM NaCl 0.5% Triton X-100
	Buffer 2	50 mM Tris-HCl, pH 8.0 10 mM DTT 2 mM NaCl 2 mM urea
	Buffer 3	100 mM Tris-HCl, pH 8.0 2 mM EDTA 10 mM DTT
	Refolding buffer	100 mM Tris-HCl, pH 8.0 2 mM EDTA 0.9 M Arginine-HCl 0.1 M L-Arginine 6.3 mM Cysteamine 3.7 mM Cystamine
	Dialysis buffer	10 mM Tris-HCl, pH 8.0 100 mM NaH_2PO_4

3.7.6 Ni-Affinity Chromatography

Ni-affinity chromatography was used as a first purification step in the purification process of His_6-tagged proteins. For small-scale purifications, expression tests and buffer screens, 1 mL-columns (HisTrap FF Crude, GE Healthcare) were used. The column was equilibrated with ~ 10 column volumes of buffer A with a flowrate of 1 mL/min. The filtered supernatant was loaded onto the column with a flowrate of 0.5 mL/min. Afterwards the column was washed with 10 – 20 column volumes of buffer A. Protein was eluted from the column using a linear or step-wise gradient of buffer B.

Fractions were collected and analyzed by SDS-PAGE. The column was regenerated with 1 M imidazole.

Table 10: List of buffers used for Ni-affinity chromatography.

Protein	Buffer A	Buffer B
JCPyV VP1	50 mM Tris, pH 7.5 5% (v/v) glycerol 250 mM NaCl 10 mM imidazole	50 mM Tris, pH 7.5 5% (v/v) glycerol 250 mM NaCl 500 mM imidazole
scFv 29B1	100 mM triethanolamine, pH 8.5 100 mM LiCl 1 mM EDTA 20 mM imidazole	100 mM triethanolamine, pH 8.5 100 mM LiCl 1 mM EDTA 1 M imidazole

3.7.7 Dialysis

Dialysis was used in order to exchange the buffer system and remove minor impurities during the purification process.

Table 11. List of buffers used for dialysis.

Protein	Buffer	Composition
JCPyV VP1	Dialysis buffer	30 mM Tris, pH 7.5 5% (v/v) glycerol 150 mM NaCl
scFv 29B1	Dialysis buffer	30 mM Tris, pH 7.5 5% (v/v) glycerol 150 mM NaCl
APMAP	Dialysis buffer 1	100 mM Tris, pH 8.0 100 mM NaCl 10 mM $CaCl_2$
	Dialysis buffer 2	10 mM Tris, pH 8.0 50 mM $CaCl_2$
	Dialysis buffer 3	10 mM Tris, pH 8.0 10 mM $Ca(Ac)_2$ 5 mM TCEP
	Dialysis buffer 4	10 mM Tris, pH 8.0
	Dialysis buffer 5	10 mM Tris, pH 8.0 5 mM TCEP

3.7.8 His-tag Cleavage in Solution

In order to remove the His_6-tag from the protein constructs after Ni-affinity chromatography, the protein solution was mixed with either 10 U of thrombin solution per mg fusion protein, 1 mg of TEV protease or 1 mg HRV 3C protease per 10 mg fusion protein and incubated overnight at 4°C. Successful digestion was controlled by SDS-PAGE. A second Ni-affinity chromatography was performed to separate cleaved from uncleaved protein. Fractions from load and wash containing the cleaved protein portion were pooled.

3.7.9 Fab Generation with Papain agarose

Monoclonal antibodies (obtained from Neurimmune AG, Schlieren, Switzerland) were dialyzed against activation buffer for 2 hours at 4°C and for 2.5 hours against digestion buffer. A papain agarose solution with a concentration of 2 mg/mL in activation buffer supplemented with 15 mM cysteine was prepared and incubated for 10 min at 37°C for activation. Antibody digestion was initiated by adding the papain agarose solution to the mAb solution (4.45 mg/mL) with a ratio of 8:100 (papain agarose/mAb). Antibodies were incubated for digestion for 5-6 h at 37°C. The reaction was stopped by centrifugation and sterile filtration in order to remove papain agarose.

Fabs were purified via a Protein A column (GE Healthcare). The column was washed with 10 mL distilled water and equilibrated with 10 mL binding buffer. The sample was loaded onto the column with a flowrate of 1 mL/min. Afterwards, the column was washed with 5 mL binding buffer. Fractions of 1 mL were collected over the course of column loading and washing. Uncleaved mAbs and Fc fractions were eluted with 10 mL elution buffer. Fractions of 1.5 mL containing 400 µL neutralization buffer in order to adjust the pH to physiological values were collected. The column was regenerated with 5 mL elution buffer, 10 mL binding buffer and 10 mL distilled water and stored in 20% (v/v) ethanol at 4°C.

Buffer	**Composition**
Activation buffer	50 mM NaH_2PO_4, pH 8.0; 1 mM EDTA
Digestion buffer	50 mM NaH_2PO_4, pH 8.0; 15 mM cysteine; 1 mM EDTA
Binding buffer	20 mM HEPES, pH 7.5; 150 mM NaCl
Elution buffer	100 mM citric acid, pH 3.0
Neutralization buffer	1 M Tris-HCl, pH 8.8

3.7.10 Formation of scFv /Fab – JCPyV VP1 Complexes

JCPyV or BKPyV VP1 protein and 29B1 scFv or 72F7 Fab were purified according to the protocol and mixed in a molar ratio of 1 : 7. The mixture was incubated at 4°C for 1

h. Stable complexes were separated form excess scFv/Fabs by size-exclusion chromatography.

3.7.11 Size Exclusion Chromatography

Analytical size exclusion chromatography (SEC) was used for further protein analysis and characterization, whereas preparative SEC was applied as final protein purification step. For analytical SEC experiments a Superdex 200 Increase 3.2/300 column (GE Healthcare) connected to an ÄKTA Ettan System (GE Healthcare) was used with a 23 µL sample loop. The column was equilibrated with SEC buffer before the concentrated and sterile filtered (0.22µm) protein sample was loaded. Detection of eluting proteins was determined by simultaneous measurements of absorbance at 280 nm, 230 nm and 215 nm. The molecular weight of the eluted proteins was estimated based on a calibration curve with standard proteins (aprotinin, ribonuclease A, carbonic anhydrase, ovalbumin, conalbumin and Blue Dextran 2000).
For the preparative SEC a Superdex 200 Increase 10/300 GL column (GE Healthcare) connected to a BioLogic Duo Flow system (BioRad) was used with a 250 or 500 µL sample loop. The column was equilibrated with SEC buffer before the concentrated and sterile filtered (0.22µm) protein sample was loaded. Fractions were analyzed by SDS-PAGE and fractions containing the corresponding protein were pooled, concentrated and either kept at 4°C or flash-frozen and stored at -80°C.

Table 12. List of buffers and colums used for protein purification via size exclusion chromatography.

Protein	SEC buffer	Column
JCPyV VP1 – scFv complexes	20 mM HEPES, pH 7.5 150 mM NaCl	Superdex 200 Increase 10/300
BKPyV VP1 – scFv complexes	20 mM HEPES, pH 7.5 150 mM NaCl	Superdex 200 Increase 10/300
APMAP	10 mM Tris, pH 8.0	Superdex 200 Increase 10/300

3.7.12 Protein Concentration Determination

The protein concentration was determined by measuring the absorbance of the protein solution at 280 nm using a NanoDrop spectrophotometer (Thermo Fisher Scientific, Waltham, USA). The concentration was determined using the Lambert-Beer law with taking the theoretical extinction coefficients at this wavelength (ε) and the length of the light path (l) into account.

$$A = \varepsilon \cdot l \cdot c$$

Equation 1: Lambert-Beer law

3.7.13 Precipitation Test

In order to find a suitable protein concentration for crystallization trials, a precipitation test with dilution series of five different ammonium sulfate (1.5–3 M) and five different PEG 4,000 (10–30 %) concentrations was performed at 20°C. A volume of 0.5–1.0 µL sterile filtered (0.22 µm) protein solution was pipetted onto a glass cover slide and an equal volume of the highest precipitant concentration was added. The drop was analyzed using a light microscope. If precipitation did not occur within ~ 3 min, the protein solution was further concentrated. Upon light to medium granular precipitation, the lowest precipitant concentration was tested next. The protein concentration was set when the protein precipitated in a timeframe of 3–5 min within the highest two to three precipitant concentrations.

3.8 Crystallographic Methods

The information in this chapter is based on the textbooks “Biomolecular Crystallography” by Bernhard Rupp (Rupp, 2009) and “Crystallography Made Crystal Clear” by Gale Rhodes (Rhodes, 2006), unless stated otherwise.

3.8.1 Protein Crystallization and Cryoprotection

Protein crystals are an assembly of repeating, regular patterns of protein molecules held together through a network of intermolecular interactions. The three-dimensional structure of the protein making up this crystal can be determined by x-ray diffraction. A commonly used method for protein crystallization is sitting or hanging drop vapor diffusion, achieving crystallization of proteins from a supersaturated solution by slowly increasing protein and precipitant concentration. Different salts, alcohols or polymers such as polyethylene glycols (PEGs) can be used. For crystallization to occur, several trials with different concentrations and buffer systems may be needed. Generally, the protein solution is mixed with the precipitant solution and a small drop is placed in a closed system containing a larger reservoir solution with higher precipitant concentration. During vapor diffusion, both precipitant and protein concentration increase through water diffusion from the drop and thus, supersaturation can be achieved. This in turn leads to the formation of crystallization nuclei, which initiates crystal growth. Protein molecules from the solution accumulate at the existing nucleus and assemble in an ordered fashion, thus driving crystal growth. Generally, low supersaturation favors controlled crystal growth, whereas high supersaturation is required for spontaneous nucleation of crystal nuclei.
Seeding is another method, which can be performed to induce heterogeneous nucleation at low supersaturation. Here, solid material, such as small or crushed crystals can be transferred to the crystallization drop and act as crystallization nuclei. Seeding can be subdivided into micro- and macroseeding. For microseeding, a dilution series of crushed crystal fragments is introduced into the crystallization drop. Another possibility to introduce the microseeds into the droplet is the so-called streak seeding, where thin fibers, for example a cat-whisker, are dipped into the seed crystal solution and then streaked through the new drop. In macroseeding experiments a single, well-

formed, protein crystal is transferred into the pre-equilibrated protein solution in order to scale up the crystals to diffraction size.
Both sitting- and hanging drop vapor diffusion experiments were used in order to obtain protein crystals. Sitting drop experiments with commercially available screens in a setup of 96-well sitting drop crystallization plates (INTELLI-PLATE 96 Well, Art Robbins Instruments, USA) were performed as initial crystallization trials. Two robot systems were used for the automated crystallization plate setup: the Tecan Evo robot for mixing drops containing 300 nL protein and 300 nL reservoir volume and pipetting reservoir volumes of 100 µL and the Crystal Gryphon LCP (Art Robbins Instruments) for mixing 200 nL protein and 200 nL reservoir volume and pipetting a reservoir volume of 50 µL. This system was also used for microseeding experiments. Crystallization plates were incubated at 4 or 20°C.
In order to optimize first crystallization hits, a wide range of different pH-values were screened against increasing precipitant concentration in a sitting drop vapor diffusion setup. Hits were then scaled up in hanging drop vapor diffusion experiments in 24-well crystallization plates (VDX plate, Hampton Research). Here, the drop volume varied from 1-2 µL, the reservoir volume (500 µL) was increased as well. Crystal plates were checked for crystal growth in regular intervals using a light microscope.
For data collection, crystals were harvested, transferred into a solution containing MPD or glycerol as cryoprotectant, before being flash-frozen in liquid nitrogen.

3.8.2 Preparation of Crystal Seeding Stocks

JCPyV VP1 Mad-1 crystals were grown for at least one day before 10 – 12 crystals were transferred into a drop of 1 µL of mother liquor solution. The drop was pipetted into an Eppendorf tube with additional 40 µL of mother liquor solution and crystals were crushed with a seed bead (Seed-bead kit, Hampton Research, USA). The seeding stock solution was aliquoted (2 µL), flash frozen in liquid nitrogen and stored at -80°C.

3.8.3 Crystallization and Crystal Soaking Experiments

Compounds for crystal soaking experiments were commercially available and purchased from Vitas-M Laboratory Ltd. (Champaign, USA), Key Organics (Camelford, UK), Alinda Chemical Ltd. (Moscow, Russia), Combi-Blocks, Inc. (San Diego, USA) and Sigma Aldrich (St. Louis, USA). Stock solutions of the compounds were prepared in DMSO and soaked into the JCPyV VP1 crystals with a final concentration of 25% (v/v). JCPyV VP1 crystals were shown to tolerate concentrations of dimethyl sulfoxide (DMSO) of up to 30% (v/v) prior to the crystal soaking experiments. Higher concentrations of DMSO resulted in crystal cracking and diffraction to only low resolutions (> 3.5 Å). The soaking time was influenced by the fragment solubility that varied from one up to 24 hours depending on the crystal stability in the presence of the respective compound.
Table 13: Soaking experiments with 20 hits from the fragment-based screening. JCPyV VP1 Mad-1 crystals were grown for at least one day before being transferred into drops with the harvesting solution supplemented with

compound stock solution. Prior to flash freezing in liquid nitrogen, protein crystals were transferred for a few seconds in a soaking solution containing 30% (v/v) glycerol as cryoprotectant.

Compound ID	Compound [mM]	DMSO [%]	Soaking time [h]
2D05	100	25	1, 6, 16, 24
3D03	100	25	16, 24
3H01	100	25	8
4A07	100	25	16
5G06	100	25	16
6C02	100	25	8
6G04	100	25	1, 6, 16, 24
7D04	100	25	8
7D06	100	25	16
8A02	100	25	6, 16, 24
12F08	100	25	16
13A05	10, 50, 100	25	24
13A06	100	25	6, 16, 24
13A09	100	25	16, 24
13B03	100	25	1
13B04	100	25	6, 16, 24
13H04	100	25	6, 16, 24
13H07	100	25	1, 2, 6, 16, 24
14A05	100	25	6, 16
14H04	100	25	6, 16, 24

The next set of compounds, which was obtained from the molecular modeling studies in collaboration with Prof. Dr. Frank Böckler (Pharmazeutische Chemie, Eberhard Karls Universität Tübingen), was prepared as stock solution in DMSO. The final compound concentration for crystal soaking experiments had to be decreased to 10 mM and a DMSO concentration of 10% (v/v) due to the limited compound solubility and harshness towards the JCPyV VP1 crystals. The soaking time was further decreased and ranged from 15 to 60 minutes. Soaking times > 60 minutes lead to complete disintegration of protein crystals.

Table 14: Soaking experiments with six hits from the molecular modeling studies. JCPyV VP1 Mad-1 crystals were grown for at least one day before being transferred into drops with the harvesting solution supplemented with compound stock solution. Crystals were set into soaking solution supplemented with 30% (v/v) glycerol before being flash frozen.

Compound ID	Compound [mM]	DMSO [%]	Soaking time [min]
889	10	10	15, 30, 60
558	10	10	15, 30, 60
2527	10	10	15, 30, 60
2530	1; 10	10	15, 30, 60
2041	10	10	15, 20, 30, 40, 60
1710	10	10	15, 20, 30, 40, 60

JCPyV VP2 derived peptides were designed with N-terminal acetylation and C-terminal amidation (Table 15) and obtained from GenScript (Central, Hong Kong). Stock solutions of both peptides were prepared in DMSO. The final peptide

concentration for crystal soaking experiments with JCPyV VP1 was 1 mM and a DMSO concentration of 25%. The soaking time varied from one up to 16 hours depending on crystal stability.

Table 15: Designed JCPyV VP2 derived peptides. Peptides were designed in two different lengths (short version 14 aa, long version 20 aa) and contained an N-terminal acetylation and a C-terminal amidation.

Peptide ID	Molecular weight [g/mol]	Sequence
VP2 short (14 aa)	1613	[COOH]-APQWMLPLLLGLYG-[NH_2]
VP2 long (20 aa)	2227	[COOH]-GANQRSAPQWMLPLLLGLYG-[NH_2]

Table 16: Soaking experiments with two JCPyV VP2-derived peptides. JCPyV VP1 Mad-1 crystals were grown for at least one day before being transferred into drops with the harvesting solution supplemented with peptide stock solution. Crystals were set into soaking solution supplemented with 30% (v/v) glycerol before being flash frozen.

Peptide ID	Peptide [mM]	DMSO [%]	Soaking time [h]
VP2 short	1	25	1, 2, 4, 16
VP2 long	1	25	1, 2, 4, 16

3.8.4 Co-crystallization

Compounds from the second set were further screened in co-crystallization experiments with JCPyV VP1 Mad-1 in addition to crystal soaking experiments due to their low solubility and the limited crystal stability. The final compound concentration was set to 1.25 mM with a final DMSO concentration of 1.42% (v/v). The final compound concentration was achieved by a serial dilution with SEC buffer. The compound solution was incubated with JCPyV VP1 solution (concentration of 6.5 mg/mL) at a molar ratio 1:7 at 4°C for one hour. Initial fine screens were used to find suitable crystallization conditions. Crystals grew within 24 hours and were harvested subsequently.
Stock solutions of the peptides were prepared in crystal mother liquor with a peptide concentration of 10 mM. The solutions were incubated at 60°C for one hour to increase the solubility of the peptide. Insoluble excess of peptide was removed by centrifugation. The exact peptide concentration amounted to slightly less than 10 mM. For co-crystallization, the peptide solution was diluted to a final concentration of 2 mM before setting up crystal plates with a 1:1 ratio of JCPyV VP1 solution and peptide solution. Crystals grew at 20°C within 24 hours and were harvested subsequently.

3.8.5 Data Collection and Data Processing

X-rays are scattered by electrons of the protein crystal. Diffraction of scattered electromagnetic waves can only be observed when the path difference between two

distinct waves with the angle Θ is an integer multiple of the applied wavelength (Equation 2), which leads to constructive interference. Otherwise scattered waves cancel each other out by destructive interference. Constructive interference is maximized by superposition of waves in phase and diffraction can be perceived as discrete maxima on a detector.

$$n\lambda = 2d\,\sin\theta$$

Equation 2: Bragg's law.

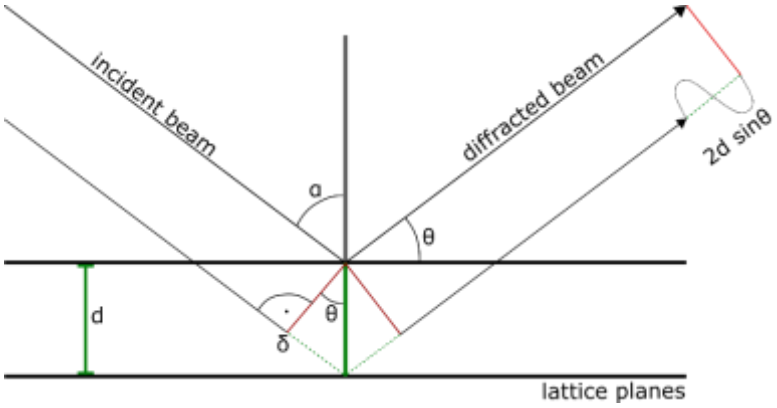

Figure 14: Graphical representation of Bragg's law. For constructive interference, the path difference of two waves diffracted at parallel crystal lattice planes must be an integer multiple of the incoming wavelength. d: distance between two lattice planes, θ: angle of incidence.

The scattering of x-rays by a single molecule is too small to be measured, hence, a highly ordered arrangement of many molecules in a periodic lattice is needed for amplification and discrete sampling of the molecular scattering function. These small repeating units, the so-called unit cells, that form the crystal lattice are defined by the length of the axes a, b and c and by the angles α, β and γ between the respective axes. Each identical unit cell contains the same number of identically arranged molecules, which can be transformed into each other by symmetry operations such as rotation or translation. Symmetry operations, such as inversions or mirror operations, involving changes within the motifs are strictly excluded for chiral molecules such as proteins. The unit cell is further divided into the asymmetric unit (ASU) by these symmetry operations. The ASU of a unit cell contains all the necessary information to generate the complete unit cell of a crystal by the underlying symmetry operations. The ASU can contain molecules related by additional symmetry, the so-called non-crystallographic symmetry (NCS). Two molecules related by NCS do not necessarily

need to be completely identical, there can be small differences, such as loop conformations.
The space group of the crystal itself is defined by the geometry of the unit cell and the crystallographic symmetry operators.

For each lattice in real space R, a corresponding lattice in the reciprocal space R* can be generated by an inverse relationship. The reciprocal lattice is a formality to simplify the treatment of diffraction geometry. Sets of parallel and equidistant lattice planes are defined by the three Miller indices h, k and l, which are integer numbers indicating the number of intercepts of a set of lattice planes with each of the unit cell axes. Each set of lattice planes *hkl* corresponds to a reciprocal lattice point with a reciprocal lattice vector d^*_{hkl} perpendicular to the set of planes *hkl*.
A graphical representation of reciprocal lattice points that can fulfill Bragg's law is called Ewald sphere. It shows that diffraction only occurs when a reciprocal lattice point *hkl* intersects the Ewald sphere with the radius 1/λ (Figure 15). Only few reflections can be observed at affixed crystal orientation, hence, the crystal and thus its reciprocal space are rotated during data collection. This results in the intersection of different lattice points at the Ewald sphere, which can be recorded. The amount of unique data to be recorded for a complete data set is dependent on the symmetry of the crystal.

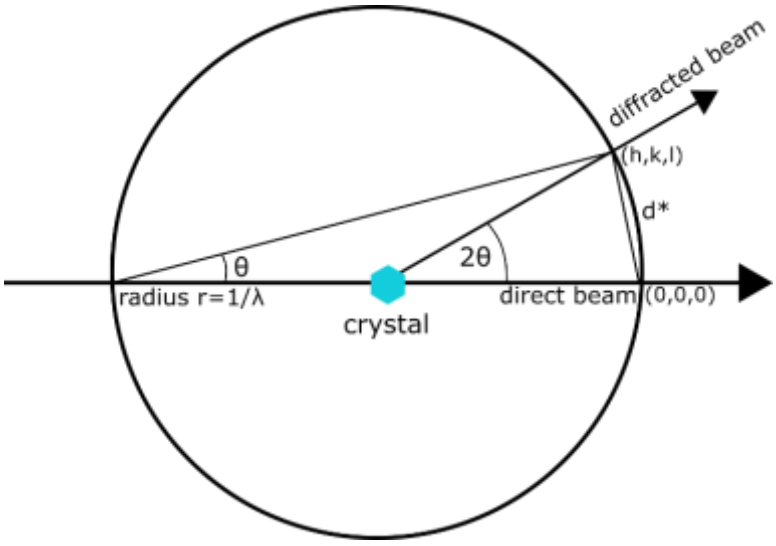

Figure 15: Graphical representation of Ewald sphere. Ewald sphere with annotations; r: radius of the sphere 1/λ, (h,k,l): coordinates of the reflection in reciprocal space, d*: 1/d.

In case of the lowest symmetry group P1 at least 180˚ have to be recorded for a full dataset with 2-fold redundancy. This only applies in the case of the fulfillment of Friedel's law, which is the absence of anomalous signal. In Friedel's law, each reflection (h, k, l) has a related reflection with equal intensity (-h, -k, -l). This in turn means that the diffraction pattern becomes centrosymmetric by definition, even if there is no center of symmetry for the according space group. The geometry of the crystal defines the direction and amount of reflections, but intensities and phase of these

reflections are determined by the molecules in the unit cell. The structure factor F_{hkl}, a complex number, can be described by the amplitude $|F_{hkl}|$ and phase φ_{hkl} (Equation 3).

$$F_{hkl} = |F_{hkl}| \cdot (cos\varphi_{hkl} + isin\varphi_{hkl}) = |F_{hkl}|\exp(i\varphi_{hkl})$$

Equation 3: The structure factor as a complex number.

The Fourier transformation links amplitude and phase of the scattered beams with the content of the unit cell. Amplitude and phase for every reflection can be calculated if the position and the electron distribution dependent scattering factor f_n are known.

$$F_{hkl} = \sum_{n=1}^{N} f_n \cdot exp[2\pi i(hx_n + ky_n + lz_n)]$$

Equation 4: Fourier transformation of atomic coordinates to structure factors.

Known amplitudes and phases allow for the calculation of the electron density ρ(x, y, z) at each point of the unit cell.

$$\rho(x,y,z) = \frac{1}{V}\sum_{hkl} F_{hkl} \cdot exp[-2\pi(hx + ky + lz)]$$
$$= \frac{1}{V}\sum_{hkl} |F_{hkl}| \cdot exp[-2\pi(hx + ky + lz) + i\varphi_{hkl}]$$

Equation 5: Fourier transformation for conversion of structure factors into electron density.

Structure factor amplitudes $|F_{hkl}|$ can be extracted from the diffraction data, however phases cannot be determined from the diffraction experiment. Thus, the so-called phase problem has to be solved via indirect methods, a vital part of structure determination by means of x-ray crystallography.
Data processing yields information about crystal geometry and numerical values about reflection intensities. Possible unit cell parameters for individual lattice types and the orientation of the unit cell in the experimental setup can be calculated taking detector distance and orientation and spot positions into account. During indexing, reflections are assigned their indices h, k and l. For this process only a subset of images is used, while for integration of the data the intensity for each reflection in the complete data set is determined. The same reflection could have been recorded at different values during data collection due to factors such as radiation damage or intensity fluctuations of the x-ray beam. In order to correct for these effects, scaling procedures are applied, which make use of scaling factors to minimize the differences between the same reflections. Partial reflections that were not completely recorded on a single image are added and symmetry-related reflections are merged. The scaling output consists of a list of all unique reflections (h, k, l) with their intensities, information about the best determined values for the unit cell and data collection parameters as well as statistics for data quality valuation.

The data processing R-factors quantify the overall quality of the intensity data by calculating the consistency of repeated measurements. The merging R-factor R_{merge} quantifies the ratio between the sum over the deviations of each redundant reflection from the mean intensity value for this reflection and the sum over the intensities of all redundant reflections (Equation 6). The value increases with higher redundancy, because a low-redundant dataset shows lower variance than a high-redundant dataset. The mean intensity of a reflection should be determined more precisely with increasing multiplicity. The redundancy-independent R-factor R_{meas} corrects for the inadvertent rise of the R-factor with increasing redundancy (Equation 7) (Diederichs and Karplus 1997). While the R-factors generally increase with higher resolution, the signal to noise ratio I/σI, decreases due to the fact that the impact of small irregularities within a crystal increases.

$$R_{merge} = \frac{\sum hkl \sum_i^n \left| I_{hkl,i} - \bar{I}_{hkl,i} \right|}{\sum hkl \sum_i^n I_{hkl,i}}$$

Equation 6: The linear merging R-factor.

$$R_{meas} = \frac{\sum hkl \sqrt{\frac{n}{n-1}} \sum_i^n \left| I_{hkl,i} - \bar{I}_{hkl,i} \right|}{\sum hkl \sum_i^n I_{hkl,i}}$$

Equation 7: The redundancy-independent R-factor with n (number of independent measurements), I (measured intensities) and $\bar{I}$ (average of symmetry- related observations of a unique reflection)

Another data quality indicator, the correlation coefficient $CC_{1/2}$, is determined by dividing the data into two equal parts, whereas each part contains a random half of the measurements of each unique reflection (Karplus and Diederichs 2012). The Pearson correlation coefficient between the average intensities of each subset is determined. At low resolution, the value for $CC_{1/2}$ is close to 1.0 and decreases to 0 at high resolution. The Student's t-test can indicate the end of statistical significance.
Quality indicators such as R_{meas} and $CC_{1/2}$ are commonly used to determine the resolution cut-off in order to discard weak data, for which the inclusion would result in a quality loss of the calculated model.
The space group of the crystal is determined after scaling. It depends on symmetry operators within the unit cell and cannot be derived from the lattice type. If the merging R-factor is low in a given space group, only reflections that are truly related by symmetry operators have been merged. Merging of reflections that are in fact not symmetry-related leads to high R-factor even at low resolution.
The plot of the mean intensity against the resolution expressed as $\sin^2/\lambda$ yields a characteristic curve (Wilson plot), with the intensity generally decreasing with higher resolution. Solvent effects cause a minimum near 5 Å and a maximum can be found in the range of 4 to 3.5 Å due to the numerous interatomic distances in proteins having this length. At resolutions higher than 3.5 Å, the intensity falls in a linear fashion, whereas the slope of linear regression in this region determines the Wilson B-factor. It

represents the decrease in diffraction due to thermal vibration and crystal disorder, having a greater effect at high resolution.

3.8.6 Structure Determination and Refinement

The electron distribution inside the unit cell determines the intensity and the phase of a reflection (h,k,l). Every scattered wave leading to a reflection (h,k,l) can be expressed as a structure factor F_{hkl} containing its amplitude $|F_{hkl}|$ and phase ϕ_{hkl}. The structure factor F_{hkl} is a complex number and can be described as a vector in the Gaussian plane (Equation 3). Its length and angle correspond to its amplitude and phase.
A Fourier transformation links the amplitudes and the phases of the scattered beams to the scattering matter of the unit cell with the sum over all atoms n, the atomic scattering factor of atom n (f_n) and its position along dimensions x, y and z (Equation 4).
Phase and amplitude of each scattered x-ray beam contain information about all atoms in the unit cell. The molecular structure can be reconstructed from diffraction data by Fourier transforms of determined amplitude and phase for each F_{hkl}. The structure factor amplitudes can be determined from the diffraction data by the intensity I_{hkl}. The intensity of scattered x-rays is proportional to the squared structure factor amplitude F^2. Phases cannot be determined from the diffraction experiment and have to be determined via indirect phasing methods. These methods include molecular replacement (MR), single or multiple isomorphous replacement (SIR/MIR), single-wavelength or multi-wavelength anomalous diffraction (SAD/MAD).

3.8.7 Molecular Replacement

Molecular replacement can be applied in case a known structure model, similar to the protein of interest, is available. The model is rotated and translated to be placed in the new unit cell or asymmetric unit until the solution with the best fit between calculated diffraction data from the replaced model and the observed data from the unknown structure is obtained.
The Matthews coefficient V_M gives an estimate on the probability of the presence of multiple copies of a molecule in the asymmetric unit (Matthews 1968). In general, protein structures have a solvent content of ~ 25-80%, with proteins diffracting to high resolution tending to have lower solvent content. Hence, V_M generally lies between 1.5 and 6 $Å^3\ Da^{-1}$ and is calculated by taking the volume of the unit cell V_{unit} cell, the molecular weight of the molecule M_W, the number of asymmetric units in the unit cell n_{ASU} and the number of molecules in the asymmetric unit z into account (Equation 8).

$$V_M = \frac{V_{unit\ cell}}{M_W \cdot n_{ASU} \cdot z}$$

Equation 8: Matthews coefficient [Å^3/Dalton].

The correct orientation of the search model is determined via independent rotation and translation in Patterson space. The Patterson function is the Fourier transform of $|F_{hkl}|^2$ and the calculated map is equivalent to the convolution of the electron density with itself. The vectors themselves can be calculated from an existing atomic model since they are independent from the phases of scattered x-rays, and are alike between closely-related structures.
The Patterson function of the experimental data and of the search model are calculated. If the orientation of the Patterson maps correlate with each other, rotation of the search model around all three axes results in a peak within the rotation function. Only intramolecular vectors, which are independent from translation, are considered for the rotation function. For the translation function only intermolecular vectors are used to translate the model along the three axes. These vectors are considerably longer than intramolecular ones. The translation function exhibits a peak for the correct translation vector.
An initial electron density map can be calculated using the initial phases derived from the search model together with the structure factor amplitudes from the diffraction experiment (Equation 5). The electron density ρ at a given position in the unit cell xyz can be determined via the unit cell volume V and the structure factors F_{hkl}.

3.8.8 Structure Refinement

Structural refinement is performed in an iterative manner. Here, the atom coordinates and temperature factors are improved to optimize the fit of the built model and the experimental data. The overall fit between diffraction data and model is numerically quantified by a global linear residual value, R-factor, between observed (F_{obs}) and calculated (F_{calc}) structure factor amplitudes.

$$R = \frac{\sum_{hkl} |F_{obs}(hkl) - F_{calc}(hkl)|}{\sum_{hkl} F_{obs}(hkl)}$$

Equation 9: Crystallographic R-factor.

For perfect agreement between the observed and calculated structure factor amplitudes, the value for R would be 0. For any random structure model, the value for R is close to 0.6. By introducing more refinement parameters and thereby overfitting, the R-value can be decreased. This problem is addressed by cross-validation and the cross-validation R-value, R_{free} (Brunger 1992). A small fraction (5-10%) is flagged as “free” and excluded from subsequent refinement. The larger set of reflections (“working”) is referred to as R_{work}. Since R_{free} is an unbiased estimate of the improvement of the structure model, it is usually higher than the value for R_{work}. Changing the model towards more realistic physical attributes will improve both R_{work}

and R_{free}, while simple cosmetic changes will only lower R_{work} and leads to an increase in the gap of the values for R_{work} and R_{free}.

3.8.9 Data Collection and Data Processing

Diffraction of produced crystals was first tested at an in-house x-ray system equipped with the x-ray generator MicroMax-007HF (Rigaku) and a MAR345 dtb image plate detector at CuKα-radiation (λ=1.5418 Å). Pretested crystals with decent diffraction were taken to the synchrotron Swiss Light Source (Paul Scherrer Institute, Villigen, Switzerland). Here, data sets were collected at the PXIII beamline equipped with a PILATUS (Pixel Apparatus for the SLS) detector at a wavelength of 1 Å.
Molecular replacement was performed for all structures solved in this thesis to overcome the phase problem. For this, the program Phaser (McCoy et al. 2007) of the CCP4 package (Collaborative Computational Project 1994) was used. Data sets were indexed, integrated and scaled using XDS (Kabsch 2010). Alternating model building and refinement cycles were performed. Coot was used for model building, structural refinement was done with the programs REFMAC5 (Murshudov et al. 2011) or phenix (Adams et al. 2002).

Construct	**Search model**	**Source**
JCPyV VP1 – 13A06 ligand	- residues 23-290 of JCPyV VP1 (Mad-1)	PDB ID: 3NXG
JCPyV VP1 – 29B1 scFv	- residues 23-290 of JCPyV VP1 (Mad-1) - scFv of 27C11	PDB ID: 3NXG
BKPyV VP1 – 29B1 scFv	- residues 31-301 of BKPyV VP1 - scFv of 29B1	PDB ID: 4MJ1

4. Results

4.1 Fragment-based Screening with JCPyV

Fragment-based screening experiments were performed using ^{19}F and transverse relaxation time (T2)-filtered NMR methods in collaboration with Dr. Christoph Rademacher (Max Planck Institute of Colloids and Interfaces, Potsdam). Both methods are 1D ligand-based approaches, which rely on the chemical shift changes of the ^{19}F nucleus in altering local chemical environments (Jordan et al., 2012: Chen et al., 2013). All compounds selected for screening with JCPyV VP1 from the library consisting of about 300 low molecular weight compounds contained a monofluoro- or trifluoromethyl group. In case of a positive binding to JCPyV VP1, a shift of the characteristic compound peak can be observed in the 1D NMR spectrum compared to the compound spectrum obtained without JCPyV VP1. In total, both NMR methods resulted in 40 double positive hits, which were subjected to crystal soaking experiments with JCPyV Mad-1 VP1 crystals. Ten compounds were already tested in preliminary work done by Dr. Luisa Ströh. One compound, 9E08, was shown to bind to JCPyV VP1.
20 additional compounds were tested in crystal soaking experiments with JCPyV VP1 crystals (Figure 16).

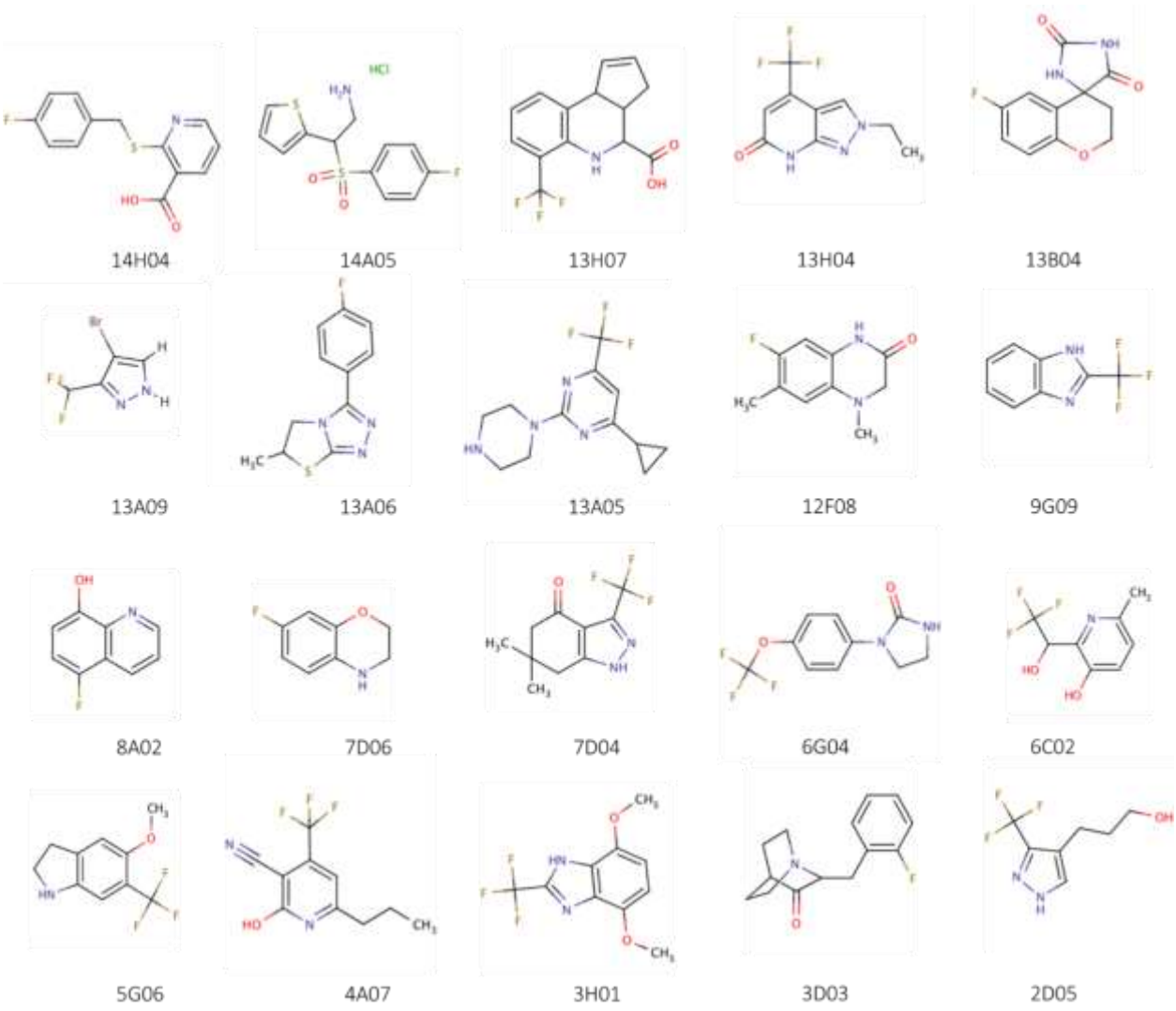

Figure 16: Fragments used for soaking experiments (Part 2). Displayed are additional 20 out of 40 double-positive hits identified by 19F and T2-filtered NMR spectroscopy. The fragment screening was performed analyzed by Dr. Christoph Rademacher and Jonas Aretz (Max Planck Institute of Colloids and Interfaces, Potsdam). The figure was prepared using ChemDraw 16.0 (PerkinElmer Inc.).

Crystals of JCPyV VP1 soaked with the 20 different compounds grew in space group C2 with one monomer in the asymmetric unit like native crystals and diffracted to atomic resolution ranging from 1.55 – 2.70 Å. Additional electron density in the simulated annealing electron difference map could only be observed for one out of the 20 tested compounds in the crystal soaking experiments with JCPyV VP1. Fragment 13A06 could be built into the additional electron density of all data sets taken, yet only the best diffracting data sets was chosen for further refinement (Table 17). The additional electron density could not be observed in simulated F_{obs} – F_{calc} electron density maps of native JCPyV VP1 or crystals soaked with other compounds.

Table 17: Statistics of data collection and refinement. Values in parentheses account for the highest resolution shell.

	13A06 (100 mM; 6 h)
Data Collection	
Beamline	SLS X06DA
Space group	C2
a, b, c [Å]	149.6, 95.8, 128.5
β [°]	110.3
Resolution [Å]	44.5-1.87 (1.99–1.87)
Unique reflections	268490 (39691)
Total reflections	936464 (132782)
R_{meas} [%]	11.5 (58.9)
I/σI	10.1 (2.3)
$CC_{1/2}$ [%]	99.6 (81.7)
Completeness [%]	97.7 (89.3)
Wilson B-factor [Å^2]	18.85
Refinement	
R_{work}/R_{free} [%]	18.4 / 21.1
No. of atoms	
Protein	10482
Ligand	160
Water	705
B-factor [Å^2]	
Protein	22.1
Ligand	22.2
Water	26.9
R.m.s.d.	
Bond length [Å]	0.008
Bond angles [°]	1.14
Ramachandran [%]	
Favored	96.7
Outliers	0.1

Compound 13A06 was shown to bind to the inside of the JCPyV VP1 pentamer with all five binding sites being occupied. Highly interesting is the fact that compound 13A06 binds to JCPyV VP1 in two distinct conformations, while each conformation can be explained with a ligand occupancy of 0.5. The binding site is located next to the strands E, F and ccw G1 of the core CHEFG1-sheet (Figure 17). This particular binding site has already been identified for compound 9E08. The binding of compound 13A06 is neither characterized by strong hydrogen bonds nor charged interactions, which also was observed for compound 9E08. Rather, the binding site is surrounded by non-polar residues F144 and F213 together with hydrophobic parts of side chains from residues H142, T215, H227ccw and T229ccw and forms a shallow, rather hydrophobic groove.

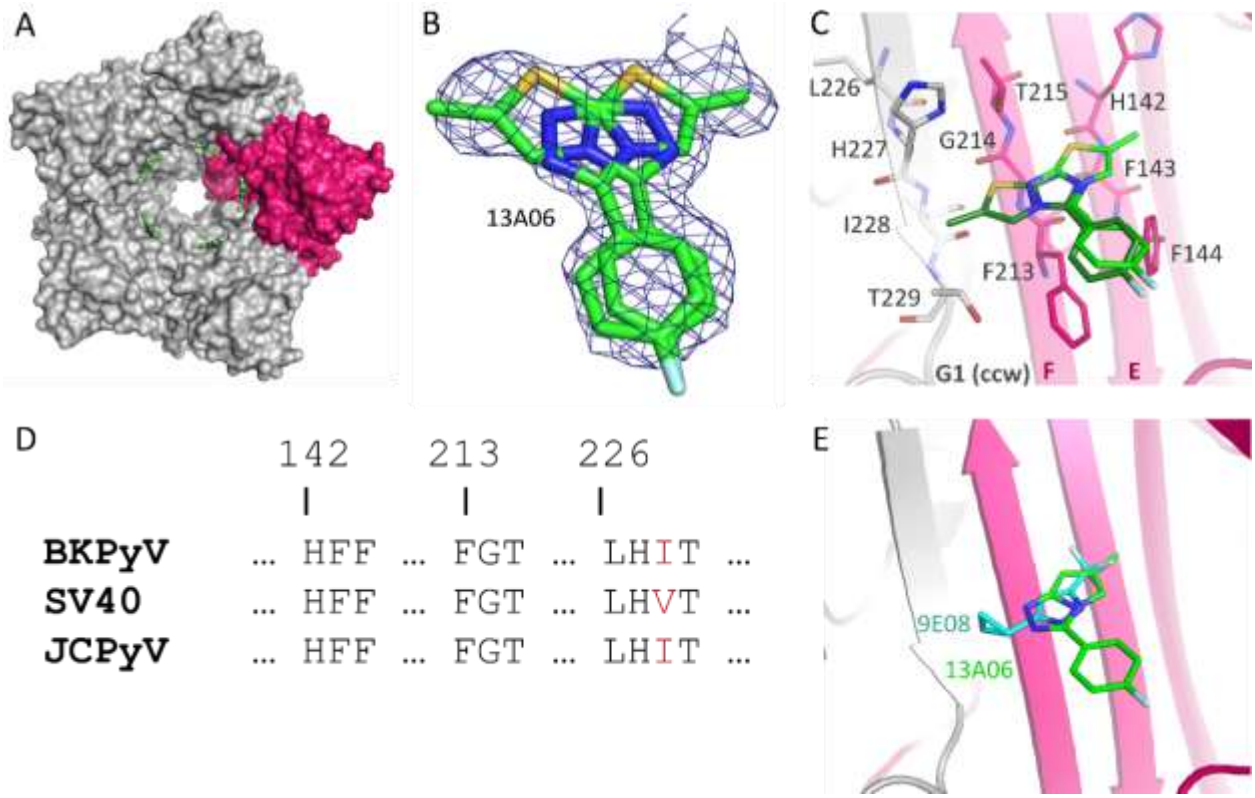

Figure 17: Binding details of compound 13A06 to JCPyV VP1. (A) View from the bottom of the JCPyV pentamer along the five-fold axis. One monomer highlighted in pink. Compound 13A06 is highlighted in green stick presentation. (B) The simulated annealed omit electron density map is contoured it at a σ level of 2.5 with a distance of 2 Å around the ligand 13A06. Compound 13A06 is binding with two possible conformations as indicated by the simulated annealed omit electron density map. (C) The binding site for compound 13A06 is formed by β-sheets E, F and the ccw G1. The compound 13A06 is shown in its double conformation with one conformation in lighter green, the other one in darker green. Carbons are colored in green, nitrogens in blue, sulfur in yellow and fluor in light blue. (D) A sequence alignment shows high conservation of the residues comprising the ligand binding site among different polyomaviruses. Non-conserved residues are highlighted in red. (E) Overlay of compounds 9E08 and 13A06 in the JCPyV VP1 binding site. Compound 9E08 is colored in cyan and compound 13A06 in green.

Since the fragment screen was targeted to identify compounds, which interfere with virus assembly or inhibit viral receptor attachment and the identified fragments did not bind at a location near the receptor binding site of JCPyV, the actual binding site was further analyzed upon potential virus assembly inhibition. Unlike for MPyV, structural and molecular information about JCPyV VP1 and VP2 interactions are not known. Yet, the interactions between the major capsid protein VP1 and the minor capsid proteins VP2 and VP3 are critical for polyomavirus entry (Nelson et al., 2015). In conclusion, the lack of the minor capsid proteins renders JCPyV non-infectious (Gasparovic et al., 2006). The mainly hydrophobic core of JCPyV VP1 is structurally conserved and an alignment between MPyV and JCPyV structures shows good agreement particularly with respect to the compound binding site (Figure 20). The superimposition with the MPyV VP1-VP2 complex structure furthermore highlighted the aspect that the compound binding site for 9E08 and 13A06 might overlap with the VP2 binding site. The protruding arm of VP2 inside the VP1 pentamer stretches along the compound

binding site (Figure 20). A sequence alignment between the VP2 sequences of MPyV and JCPyV showed only partial conservation. The C-terminal part of VP2, which was well resolved and involved in interactions with VP1 in the complex structure, exhibited good conservation between MPyV and JCPyV (Chen, Stehle, and Harrison 1998). However, side chains are not visible since they could not be modeled in the electron density, hence, it remains challenging to make any predictions on interactions between VP2 residues and VP1. Nevertheless, another interesting feature of the compound binding site of 9E08 and 13A06 is the high sequence conservation among prominent polyomaviruses, such as JCPyV, BKPyV, SV40 as well as MPyV (Figure 17). This suggests the importance of these residues in the context of JCPyV VP1 – VP2 interactions and the possibility of blocking these interactions with high-affinity compounds.

In order to enhance the low millimolar affinity from the two identified compounds 9E08 and 13A06, computational docking studies in collaboration with Prof. Dr. Frank Böckler (Pharmazeutische Chemie, Eberhard Karls Universität Tübingen) based on the results of the crystal soaking experiments were performed. These molecular modeling studies were based on the binding mode and chemical structure of the compounds identified via crystallographic soaking experiments, but also the outline of the binding pocket with its surrounding residues, which could play a role in stabilizing the ligand in the binding site by definite interactions like the formation of hydrogen bonds. In order to establish definite interactions, the compound and the binding site in JCPyV VP1, residue N276 was vital to the molecular modeling studies in establishing a hydrogen bond with the compound in the otherwise shallow and hydrophobic binding pocket. Virtual screening was performed with a library of > 1,000,000 compounds applying the GOLD (Genetic Optimisation for Ligand Docking) algorithm. Docking 3D coordinates of a ligand into low energy states of a protein binding site is commonly used for pose prediction. The docking algorithm furthermore ranks the quality of the docking by providing a score a score for the individual pose. Constraints, like the fulfillment of specific hydrogen bonds, were taken into account as well as the elimination of unfavorable ligand conformations by utilizing customizable torsion angle distributions (Cambridge Structural Database). These docking studies have limited accuracy on predictions whether a compound binds to the target protein. This had to be confirmed in crystal soaking and co-crystallization experiments. About 100 compounds were identified in the molecular modeling studies as positive hits for binding to JCPyV VP1. The six highest ranked hits were selected for crystal soaking and co-crystallization experiments (Figure 18).

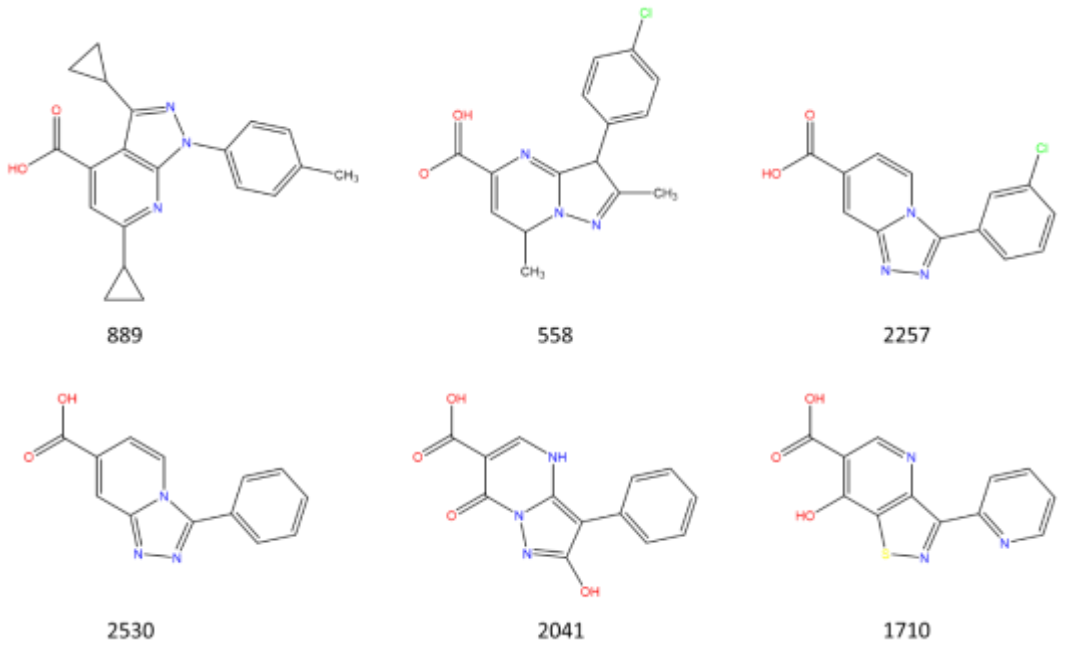

Figure 18: Fragments used for soaking and co-crystallization experiments (Part 3). Displayed are six hits identified by computational docking studies. The screening was performed and analyzed by Dr. Frank Boeckler and Andreas Lange (Pharmazeutische Chemie, Karl Eberhards Universitaet Tuebingen). The figure was prepared using ChemDraw 16.0 (PerkinElmer, Inc.).

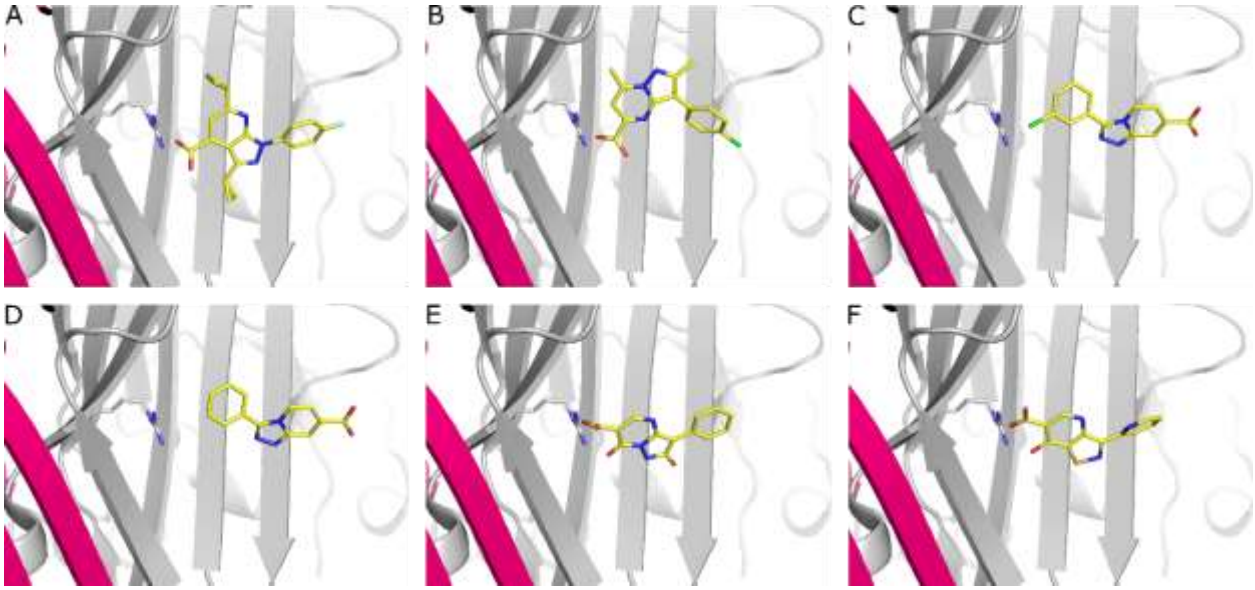

Figure 19: Results of the computational docking studies with postulated JCPyV VP1 binding. Displayed are the six selected compounds in context of JCPyV VP1 binding (A: compound 889, B: compound 558, C: compound 2257, D: compound 2530, E: compound 2041, F: compound 1710). One JCPyV VP1 monomer is shown in grey, the neighboring monomer in pink. Residue N276, which was selected as interaction anchor point in the molecular modeling studies, is displayed in stick presentation. The individual compounds are also highlighted in stick presentation with carbon in yellow, nitrogen in blue, oxygen in red, sulfur in light yellow and chlorine in green.

JCPyV VP1 crystals soaked with six different compounds and co-crystals of JCPyV VP1 and the respective compound all grew in space group C2 with one monomer in the asymmetric unit similar to native crystals and diffracted to atomic resolution ranging from 1.49 – 1.80 Å. Additional electron density in the simulated annealing electron difference map could not be observed for any of the tested compounds in neither crystal soaking nor co-crystallization experiments with JCPyV VP1.
Since none of the potential compounds identified in molecular docking studies were shown to bind JCPyV in crystal soaking and co-crystallization experiments, although they were the highest ranked hits of the computational studies, a new strategy was pursued. VP2 derived peptides were designed in order to block the VP2 binding site, which is essential for JCPyV infectivity. The sequence alignment between MPyV and JCPyV VP2 showed good conservation in the C-terminal region, hence the design of a VP2 analog peptide was based on this alignment (Figure 20). Two peptides with different lengths and N-terminal acetylation and C-terminal amidation were selected for crystal soaking and co-crystallization experiments with JCPyV VP1 to confirm binding.

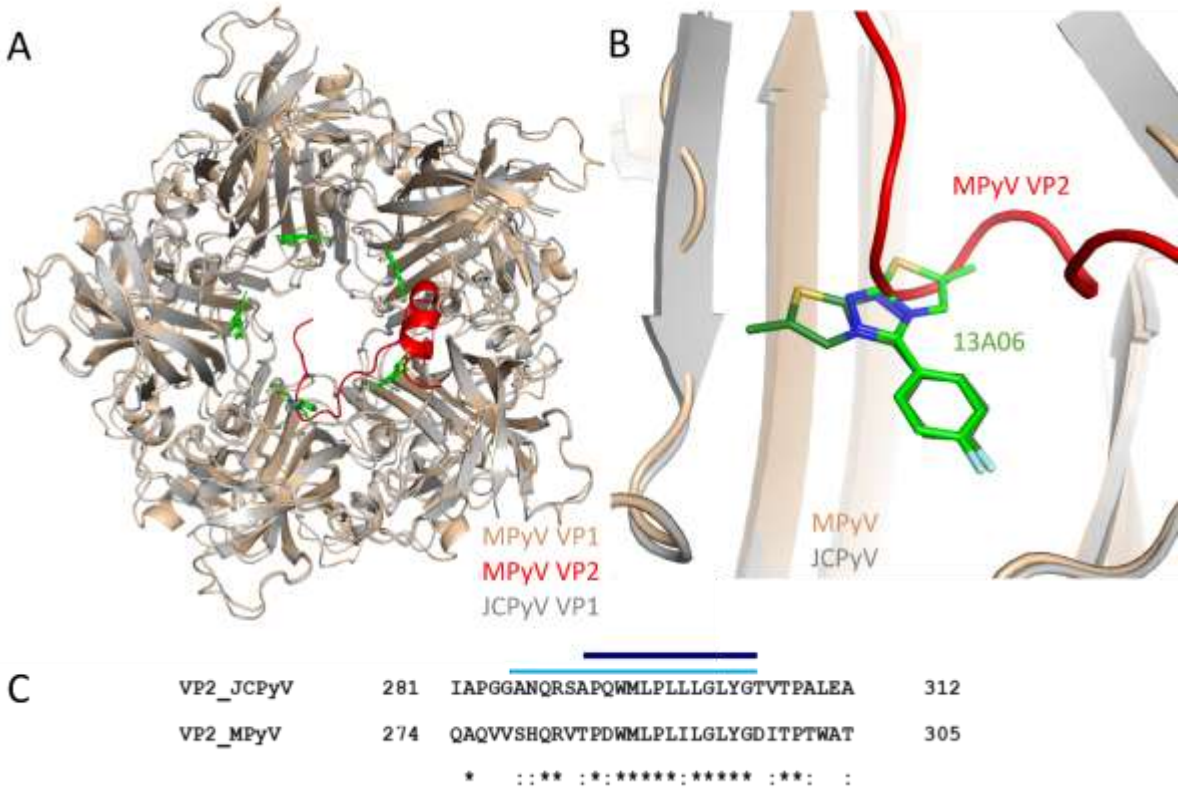

Figure 20: The 13A06 binding site shows overlap with the binding site of VP2. (A) Superimposition of the JCPyV VP1–13A06 structure with the MPyV VP1-VP2 complex structure (PDB code 1CN3) viewed from the bottom of the pentamer along the five-fold axis. Cartoon representations are colored in grey for JCPyV and wheat for MPyV, whereas MPyV VP2, which was visible in the MPyV complex structure, is highlighted in red. Compound 13A06 is shown in green stick representation. (B) Close-up view of the JCPyV VP1 binding site of 13A06, which overlaps with the VP2 binding site of the MPyV VP2 complex structure. Compound 13A06 is shown in the bound double conformation with one conformation colored in light green and the other one in dark green. Nitrogen is colored in blue, sulfur in yellow and fluor in light blue. The JCPyV VP1 binding site of 13A06 is located within the region of VP1 that contacts the N-terminal part of VP2 in the MPyV VP1-VP2 complex structure. (C) Sequence

alignment of VP2 from the MPyV strain PTA and JCPyV strain Mad1. Sequence alignment was performed with Clustal Omega 1.2.4 (EMBL-EBI). Conserved residues are highlighted with an asterisk, chemically similar ones with a colon. The conserved C-terminal region, which was also visible in the MPyV VP1-VP2 complex structure, was selected for the design of two VP2 derived peptides differing in their length. The sequence chosen for the longer derived (20 residues) is highlighted with a light blue bar above the respective JCPyV VP2 sequence, the sequence for the shorter construct (14 residues) with a dark blue bar.

JCPyV VP1 crystals were soaked and co-crystallized with the VP2 derived peptides. Crystals grew in space group C2 and diffracted from 1.3 to 2.4 Å. For JCPyV VP1 crystals soaked with the designed peptides, no additional electron density was observable in the simulated annealing electron difference map, hence, it can be stated that the peptides did not bind to JCPyV VP1 in this experimental setup. For co-crystals of JCPyV VP1 and the VP2 derived peptides, additional electron density could be observed in the simulated annealing electron difference map compared to native JCPyV VP1 crystals. This additional density was located inside of the VP1 pentamer along the five-fold symmetry axis. Yet, the difference omit map could not be assigned to any peptide structure in any of the data sets this density and therefore binding of the peptides to JCPyV VP1 could not be confirmed.

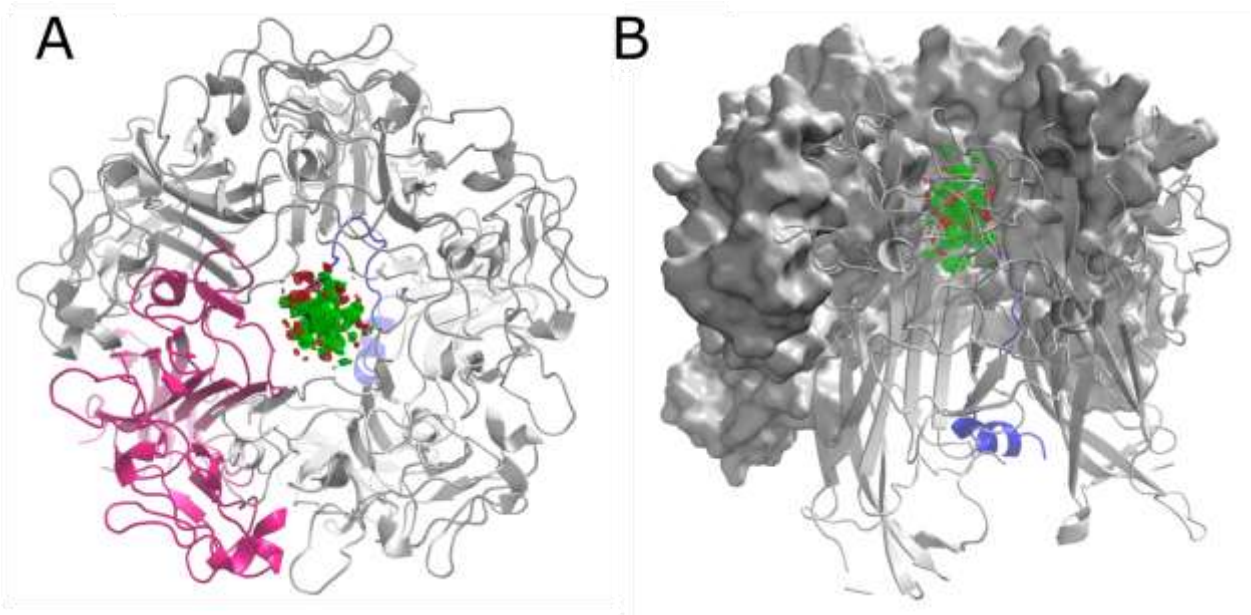

Figure 21: Omit electron density for JCPyV VP1 – VP2 derived peptides. (A) Superimposition of the simulated annealed omit electron density map of the co-crystal structure of JCPyV VP1 and VP2 derived peptide (long construct) with the MPyV VP1-VP2 complex structure. $f_o - f_c$ map (green/red) contoured at ± 3 σ is shown around 6 Å around points along the fivefold axis of JCPyV VP1 viewed from the top. JCPyV VP1 is shown in stick representation with one monomer highlighted in pink. VP2 is shown in blue and partially overlaps with the omit electron density. (B) Superimposition of the MPyV VP2 complex structure with the JCPyV VP1 structure showing the omit electron density as viewed from the side. The back three monomers in the pentamer are shown in surface presentation, the two in the front in cartoon representation to highlight the omit electron density and MPyV VP2 in the inner part of the VP1 pentamer.

4.2 Development of a Purification Strategy for a Putative JCPyV Receptor -APMAP

4.2.1 APMAP Constructs

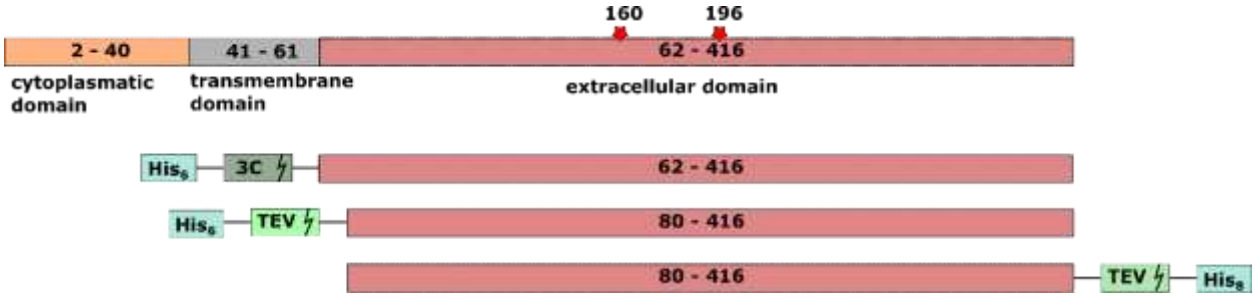

Figure 22: Overview of APMAP constructs. The upper panel depicts the original construct with cytoplasmatic domain, transmembrane domain and extracellular domain. The extracellular domain comprising residues 62 – 416 contains two N-glycosylation sites, which are highlighted with red stars (position 160 and 196). Three constructs were designed based on the original sequence comprising just the extracellular part of the protein. His-tags are shown in cyan, 3C-cleavage site in darker and TEV-cleavage site in lighter green.

4.2.2 Protein Structure Prediction of APMAP Fold

The tertiary structure of the extracellular domain of APMAP containing the two glycosylation sites was assessed and modeled with SWISS-MODEL, a protein structure homology-modelling server (Waterhouse et al. 2018). The model was calculated based on the highest sequence identity of a structurally characterized protein. For APMAP, the protein with the highest sequence identity (29%) in the PDB is strictosidine synthase (STR1) from *Rauvolfia serpentina*, an Indian medicinal plant. It features a six-bladed β-propeller with each blade containing a twisted four-stranded antiparallel β-sheet. The blades are radially arranged around a pseudo six-fold axis (Figure 9) (Ma et al. 2006). STR1 is expressed in the plant as a precursor protein and was shown to be glycosylated (Pfitzner and Zenk 1989). *E. coli* was used as expression system for the purification of STR1 and the subsequent crystallization (Ma et al. 2004).

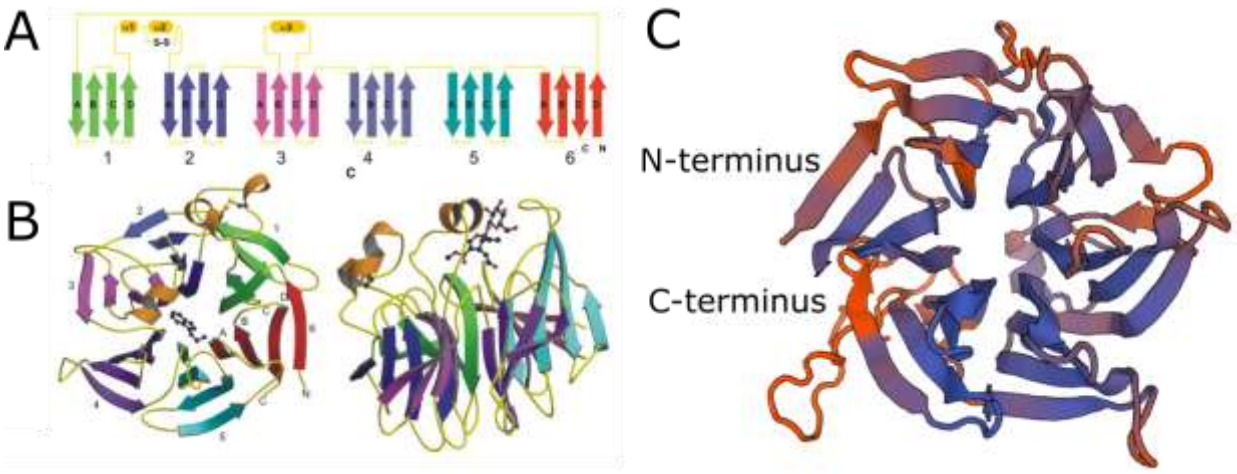

Figure 23: APMAP structure model. The structure of the extracellular domain of APMAP was modelled based on the sequence of Strictosidine Synthase STR1 (PDB code: 2V91) (B). The sequence identity between both proteins is 29%. The tertiary structure exhibits a six-bladed β-propeller fold, in which each blade consists of four antiparallel β-strands (A). Regions of good sequence coverage and local quality estimates are colored in blue, regions with worse quality estimated are colored in red (C). The model was calculated by SWISS-MODEL. Figure panels A and B are taken from (Ma et al. 2006). Material is copyright by American Society of Plant Biologists.

The homologous superfamily of six-bladed β-propellers or TolB-like proteins represents domains that can be found in TolB proteins, in soluble quinoprotein glucose dehydrogenases, in calcium-dependent phosphotriesterases and in serine/threonine protein kinase (PknD) NHL repeat domains. The propeller structure is a stable scaffold with the top, bottom, side faces and the central channel capable of forming protein-protein interactions (Chen, Chan, and Wang 2011).

4.2.3 Purification of Construct His_6-3C-APMAP (62-416)

The APMAP construct comprising amino acids 62-416 in vector pET-28a was initially expressed in *E. coli* SHuffle T7 Express cells. Expression tests with varying IPTG concentrations at different temperatures were performed to check for successful overexpression of APMAP. Overexpression of the corresponding protein, as indicated by the appearance of bands in an SDS-PAGE gel corresponding to the molecular weight of the protein, was monitored over a period of time. Subsequent solubility tests were performed in order to find suitable buffer conditions, which showed that the protein was not soluble in any of the tested conditions (Table 7). Test Ni-affinity chromatography showed that the protein is highly insoluble in the chosen buffer and does not shown binding to the column. Solubility tests were additionally performed with protein expressed in *E. coli* BL21 (DE3) cells (Figure 24A+B).

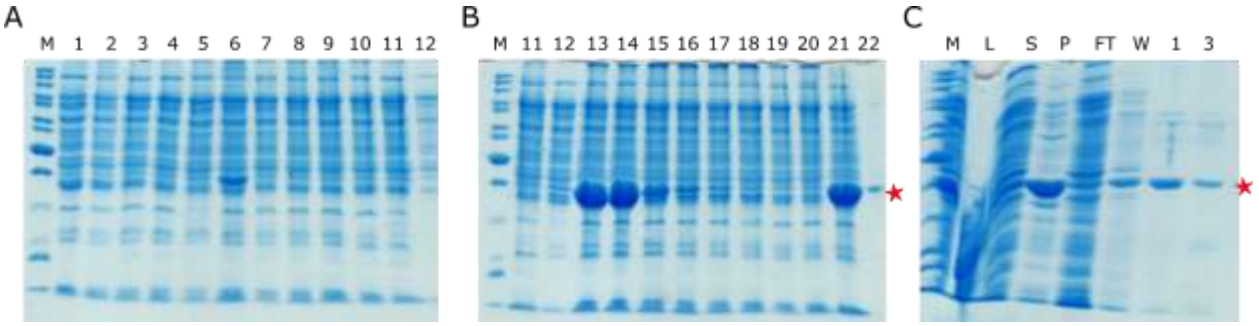

Figure 24: Solubility test of APMAP and initial purification trial. (A+B) SDS-PAGE gels of solubility tests of APMAP expressed in *E. Coli* BL21 (DE3). The buffer composition is listed in Table 7. A band at ~40 kDa corresponds to the molecular weight of the target protein and is marked with a red star. (C) Initial purification trial. For the initial purification trial buffer 17 was chosen. After lysis (L), the soluble fraction (S) shows a prominent band at ~40 kDa and the pellet fraction (P) an even thicker band at the corresponding molecular weight. The protein of interest and other proteins eluted in flow-through (FT) and wash fractions (W). The protein of interest already eluted with 10 mM imidazole (fractions 1 and 3).

All buffers screened contained detergents. Here, APMAP was found to be soluble in several conditions. A test Ni-affinity chromatography performed at 20°C showed that the protein exhibits low affinity to the Ni-column and elutes at very low imidazole concentrations. Nevertheless, eluted protein was decently pure and fractions containing APMAP were pooled in order to be analyzed via analytical SEC (Figure 24).

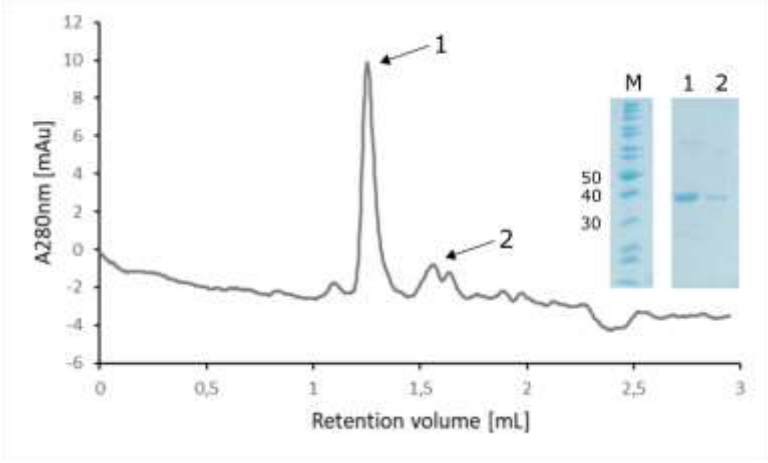

Figure 25: Analytical SEC of elution fractions. Size exclusion chromatogram with the absorbance shown at 280 nm. The two peaks both contain the protein of interest. The first peak corresponds to an oligomeric version (hexamer), while the second one corresponds to a monomeric version.

SEC with an SD200Increase 3.2/200GL (GE Healthcare) resulted in two single peaks indicating two distinct species: A main species corresponding to a MW of about 240 kDa (elution volume 1.26 mL) and a second one with an elution volume corresponding to a MW of 40 kDa (elution volume 1.55 mL). The second species would approximate the monomeric version of APMAP, whereas the major species indicates an oligomeric version (hexamer) of APMAP.

The pooled fractions from Ni-affinity chromatography were dialyzed, but the protein aggregated completely after a short time presumably due to the lack of detergent in the dialysis buffer.

Preparative SEC performed with buffer supplemented with detergent resulted in a single peak corresponding to oligomeric APMAP (Figure 25). Peak fractions were analyzed via SDS-PAGE and showed decent purity. They were pooled and concentrated in order to set up commercial crystallization screens.
Small crystals were obtained after 14 days in a condition containing 0.2 M $MgCl_2$, 0.1 M Tris, pH 8.5, 20% PEG 8000. They were evaluated at the in-house x-ray-source and at the synchrotron facility. Test shots revealed only few reflections lacking a defined diffraction pattern. Therefore, the obtained crystals are most likely crystallized salt from the crystallization condition.
Protein used for crystallization was further subjected to analysis via DLS (Figure 26).

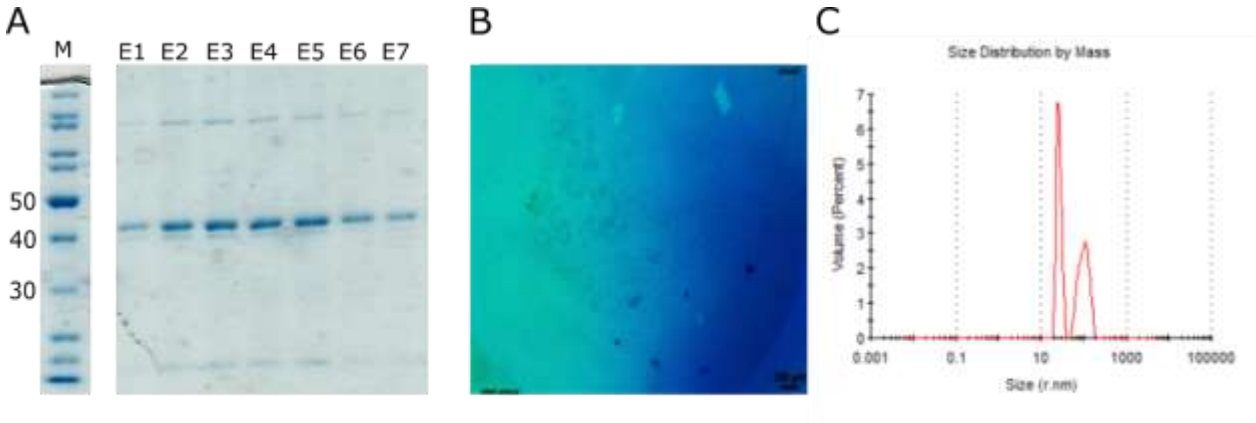

Figure 26: Purification and crystallization of APMAP and DLS measurement. (A) SDS-PAGE gel of fractions collected from preparative size exclusion chromatography. A band at ~40 kDa corresponds to the molecular weight of the protein. (B) Crystals of APMAP in 0.2 M $MgCl_2$, 0.1 M Tris, pH 8.5, 20% PEG 8,000. (C) Dynamic light scattering experiments of APMAP utilized for crystallization. The size distribution profile shows a polydisperse system, with an estimated molecular weight between 752,000 and 17,300,000 kDa.

The results from DLS do not show a monodisperse peak and the estimated MW of the measurement does correlate neither with the monomeric version of APMAP (40 kDa) nor with the oligomeric species (240 kDa). Rather, the estimated MW of the measurement ranges between 752,000 and 17,300,000 kDa, implying the presence of protein aggregate and/or micelles formed by the accompanying detergent. The formation of micelles should have been circumvented by staying below the critical micelle concentration (CMC) of NLS with 14.57 mM. With an NLS concentration of 0.4% equaling 13.63 mM, the CMC was theoretically not exceeded.

4.2.4 Purification of Construct His_6-TEV-APMAP (80-416)

Due to persistent solubility and stability problems of the first APMAP construct, new constructs containing N-terminally truncated versions of the extracellular domain of APMAP were designed (Figure 22). The APMAP construct comprised of amino acids

80-416 of the extracellular domain in vector pEt-28a was initially expressed in in *E. coli* SHuffle T7 Express and *E. coli* BL21 (DE3) cells. Expression tests with varying IPTG concentration showed good protein overexpression in both *E. coli* strains (Figure 27A). Solubility tests of APMAP expressed in BL21 cells revealed several buffer conditions (Table 7), which exhibited decent solubilization capabilities of APMAP (Figure 27B). Buffer 6 and buffer 13 were chosen for initial purification trials. Here, it could be shown that the majority of the expressed protein is still insoluble, and soluble protein does not exhibit any affinity to the Ni-column (Figure 27C).

Figure 27: Expression test, solubility test and initial purification trial. (A) SDS-PAGE gel of expression tests performed in *E. coli* BL21 (DE3) and SHuffle T7 Express. In comparison to the sample taken pre-induction (p-Ind) with IPTG, a prominent band appears at ~40 kDa corresponding to the molecular weight of the target protein. (B) SDS-PAGE gel of solubility tests of APMAP expressed in *E. Coli* BL21 (DE3). The buffer composition is listed in Table 7. A band at ~40 kDa corresponds to the molecular weight of the target protein and is marked with a red star. (C) Initial purification trial. For the initial purification trial buffer 12 was chosen. After lysis (L), the soluble fraction (S) shows a prominent band at ~40 kDa and the pellet fraction (P) an even thicker band at the corresponding molecular weight. The protein of interest and other proteins eluted in flow-through (FT) None of the protein could be found in the wash fraction (W) nor in the fractions eluted with an imidazole gradient (fractions 1 and 3).

Further solubility tests were performed with APMAP expressed in *E. coli* SHuffle T7 Express cells to find a suitable buffer system for a large-scale purification. These results showed good solubility of the protein in buffer 3, which was selected for purification trials (Figure 28A). Initial purification trials after upscaling of the expression culture revealed that APMAP remains completely insoluble in the chosen buffer system (Figure 28B).

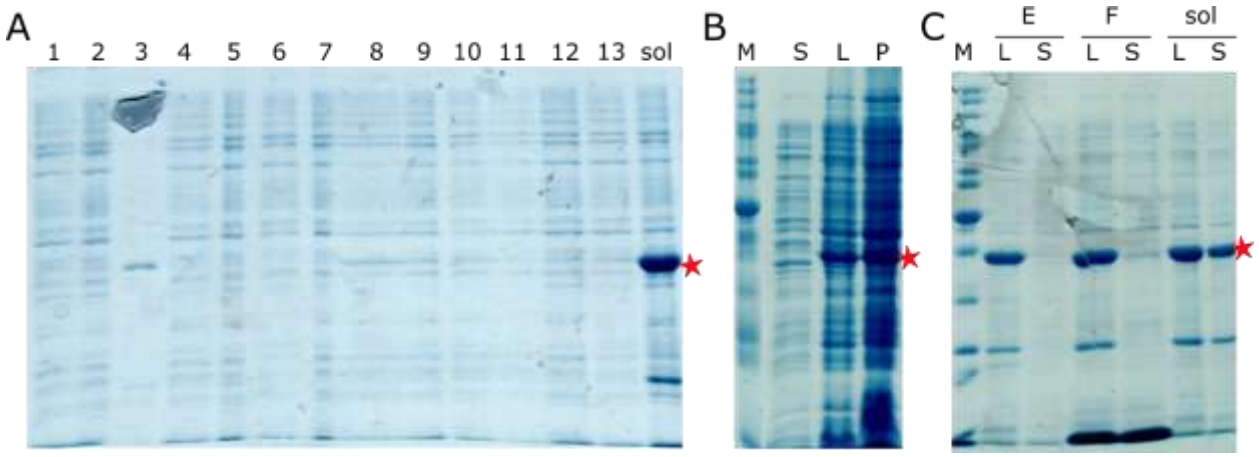

Figure 28: Solubility tests of APMAP expressed in *E. coli* SHuffle T7 Express. (A) SDS-PAGE gel of solubility tests performed in *E. coli* SHuffle T7 Express. The composition of the buffers is listed in Table 7. Results are comparable with solubility tests performed with protein expressed in *E. Coli* BL21 (DE3) cells. (B) Buffer 3 was chosen for an initial purification trial. The SDS-PAGE gel shows that the protein is not soluble in the chosen buffer as indicated by the supernatant fraction (S). (C) Additional solubility tests with protein expressed in *E. Coli* SHuffle T7 Express. Buffer E was not suitable for the solubility of the protein. However, buffer F was able to get some protein into solution as indicated by the weak band for the supernatant fraction (S).

Since none of the tested buffers were able to solubilize APMAP beyond small-scale expression, two different buffers were tested (buffers E and F, Table 7). Buffer E is supplemented with 1 mg/mL lysozyme, which has been proven to work in the purification of the protein STR1 (30% sequence identity with APMAP)(Ma et al. 2004). Buffer F contains urea and glycerol as additives in order to increase protein solubility. This buffer was able to get small amounts of APMAP into solution (Figure 288C).
Yet, purification experiments performed with buffer F showed no affinity to the Ni-column of the soluble fraction of APMAP and the elution exhibited only contaminants (Figure 29A). These contaminants, eluting at distinct imidazole concentrations, were analyzed via MALDI-TOF mass spectrometry (MALDI-TOF MS). Here, it could be shown that both contaminants are chaperones (60 kDa chaperonin 1 and Chaperone protein DnaK).
In order to activate and remove the chaperones, which were found to be co-expressed and co-purified with APMAP, additional wash steps were introduced into the conventional purification protocol. The first wash step consisted of the original buffer A supplemented with 5 mM MgATP, while the second step involved Buffer A with 10% glycerol and high amounts of salt. The purification shows that indeed the contaminants were removed via the additional wash steps (Figure 29B).

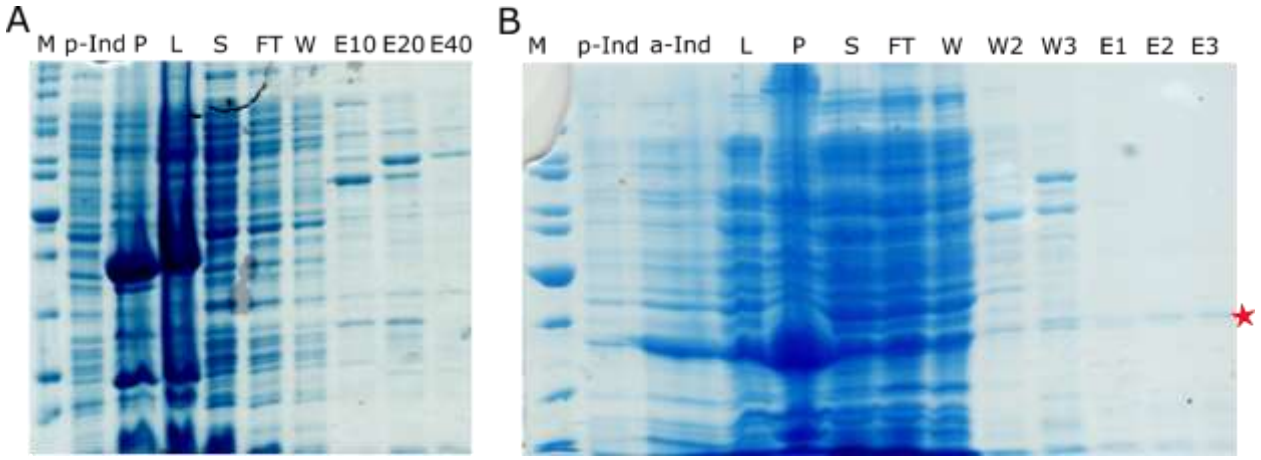

Figure 29: Purification trials of APMAP. (A) SDS-PAGE gel of purification trial performed with Buffer F. After lysis (L), most of the protein has to be found insoluble in the pellet fraction (P). Decent amounts were soluble in the supernatant fraction (S). The protein of interest eluted in the flow-through (FT) and wash fraction (W). Only contaminants eluted in the fractions with different concentrations of imidazole (E10, E20 and E40). (B) SDS-PAGE gel of purification trial performed with Buffer F including additional wash steps with MgATP (W2) and 10% glycerol and high salt concentrations (W3). Minor amounts of protein eluted from the column at imidazole concentrations of 100 mM (E1-E3).

4.2.5 Purification of Construct APMAP (80-416)-TEV- His_6

Since the poor solubility of APMAP and the low affinity of the protein to the Ni-column pose major problems for the purification, a third protein construct was designed comprising the same stretch of amino acids of the extracellular domain with a C-terminal His_8-tag. The aforementioned results might hint to an inaccessibility of the N-terminal His_6-tag or affinity to the Ni-column is impaired due to an insufficient length of the tag. Switching the location of the tag and additionally extending the length aims at circumventing these problems.
Expression tests of the new construct in a pET-28a-vector in *E. coli* Arctic Express cells showed no good overexpression of the protein indicated by the band at around 40 kDa, which is already present before induction with IPTG and only showed significantly increase at the highest IPTG concentration (600 mM) after overnight expression (Figure 30A).
Initial purification tests confirmed this result with a band at around 40 kDa almost as prevalent for the pre-induction sample as for the post-induction (Figure 30B). The majority of expressed protein is insoluble, as indicated by the dominant band in the pellet sample. The soluble protein fraction again does not show any binding to the Ni-column as it is eluting off the column in flow-through and wash fractions.

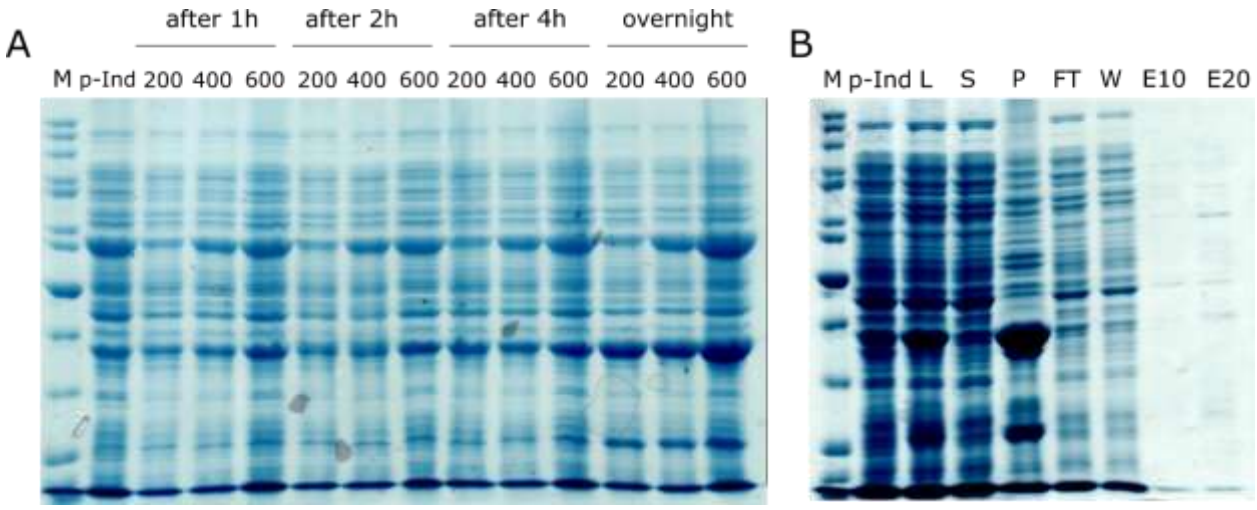

Figure 30: Expression test and initial purification trial. (A) SDS-PAGE gel of expression tests performed in *E. coli* Arctic Express cells. The band at ~40 kDa, corresponding to the molecular weight of the protein, can already be seen in the sample taken before the induction with IPTG (p-Ind). Samples were induced with different concentrations of IPTG (200 mM, 400 mM, and 600 mM) and harvested for analysis after different time points. (B) Initial purification trial of sample induced with 600 mM IPTG and harvested after 4 hours. For the initial purification trial buffer 12 was chosen. After lysis (L), the soluble fraction (S) shows a prominent band at ~40 kDa and the pellet fraction (P) an even thicker band at the corresponding molecular weight. The protein of interest and other proteins eluted in flow-through (FT). The protein of interest cannot be found in the wash fractions or fractions eluted via imidazole gradient (W, E10 and E20).

4.2.6 Inclusion Body Purification and Refolding of His_6-TEV-APMAP (80-416)

Constructs of APMAP have been shown to be prone to insolubility and inclusion body formation, hence purification from inclusion bodies was conducted. For this strategy, the construct comprised of residues 80-416 of the extracellular domain of APMAP including the N-terminal His_6-tag and TEV-cleavage site was used.
The protein was expressed in *E. coli* SHuffle T7 Express cells at 20°C after induction with 400 mM IPTG overnight and was purified after refolding from inclusion bodies. For the next purification step, the protein was concentrated before being subjected to dialysis. This buffer exchange led to almost quantitative protein aggregation. After removal of the protein aggregate, the remaining protein solution was applied to a Ni-column. The protein eluted from the Ni-column at a concentration of 200 mM imidazole. Fractions collected during the elution showed impurities in the first fractions, which were successfully removed towards the later fractions. The concentration of the pooled peak fraction was too low (0.15 mg/mL) to allow for analysis via analytical SEC, hence the protein solution was concentrated. However, the protein showed irrevocable binding to the concentrator membrane, resulting in complete protein loss.

In order to avoid serious protein aggregation, the dialysis was omitted for the next purification. Instead, the protein solution was immediately subjected to Ni-affinity chromatography after refolding. Since the refolding buffer contained 2mM EDTA, loading these high volumes onto the column (>100 mL) led to the removal of Ni-ions off the agarose column resin. Even a preceding dialysis against refolding buffer

without EDTA did not prevent this with the protein eluting off the column during flow through and wash, concurrently with the Ni-ions. Nevertheless, the protein showed decent purity in the wash fractions collected. Analytical SEC with the modified refolding buffer was performed to analyze the wash fraction. Although multiple peaks were observed, the peak at a retention volume of 1.57 mL corresponds to a MW of approximately 49 kDa and therefore to monomeric APMAP. This result was confirmed for a preparative SEC with a peak at a retention volume of 14.3 mL, indicating the elution of monomeric APMAP. Peak fractions analyzed via SDS-PAGE showed a single band at the corresponding MW of APMAP (Figure 31C), suggesting successful purification of the protein.

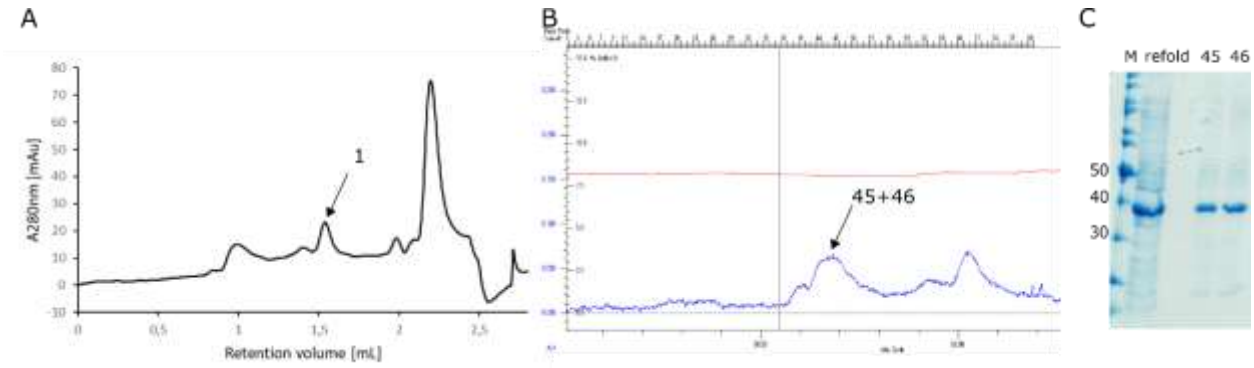

Figure 31: Purification of refolded APMAP. (A) Analytical size exclusion chromatography of refolded APMAP in refolding buffer. The peak at a retention volume of 1.57 mL corresponds to the molecular weight of the protein of interest. (B) Preparative size exclusion chromatography of refolded APMAP. The peak at a retention volume of 14.3 mL corresponds to the molecular weight of the protein of interest. Peak fractions (45+46) were collected and analyzed via SDS page (C). The band at ~40 kDa for the peak fractions indicates successful purification of the protein. Contaminants present in the sample before gelfiltration (refold) were removed.

For crystallization attempts, this buffer system is rendered as not suitable due to the additives such as L-Arginine. A preparative SEC attempt with SEC buffer no longer showed a peak at the corresponding retention volume, instead a peak implying protein aggregation occurred.
Small-scale dialysis attempts were made using different buffer systems. Buffers 1 and 4 (Table 11) showed only minor traces of protein aggregation and were suitable for APMAP stability in solution (Figure 32). Buffer 4 has been utilized as dialysis buffer in the purification protocol for STR1 (Ma et al. 2004).

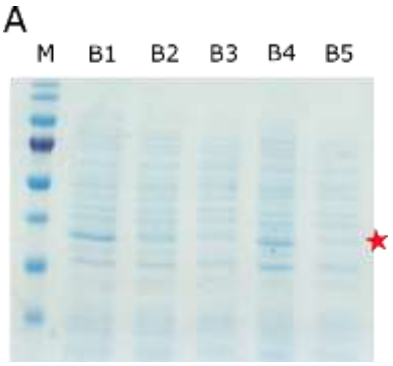

Figure 32: Dialysis of refolded APMAP in different buffers. SDS-PAGE of refolded APMAP samples dialyzed against different buffers for 24 h. Buffer system 1 and 4 show a band at the corresponding molecular weight (marked with a red star), indicating these are suitable buffers for APMAP.

Protein dialyzed in buffer 4 was analyzed via CD spectroscopy for proper protein folding (Figure 33).
CD spectra revealed a proper protein folding with a high beta-sheet content (Louis-Jeune, Andrade-Navarro, and Perez-Iratxeta 2012). The local minima at around 218 nm and local maxima at 195 nm indicate well-defined β-sheets. A high degree of disorder would be indicated by very low ellipticity above 210 nm and negative bands near 195 nm (Greenfield 2006).

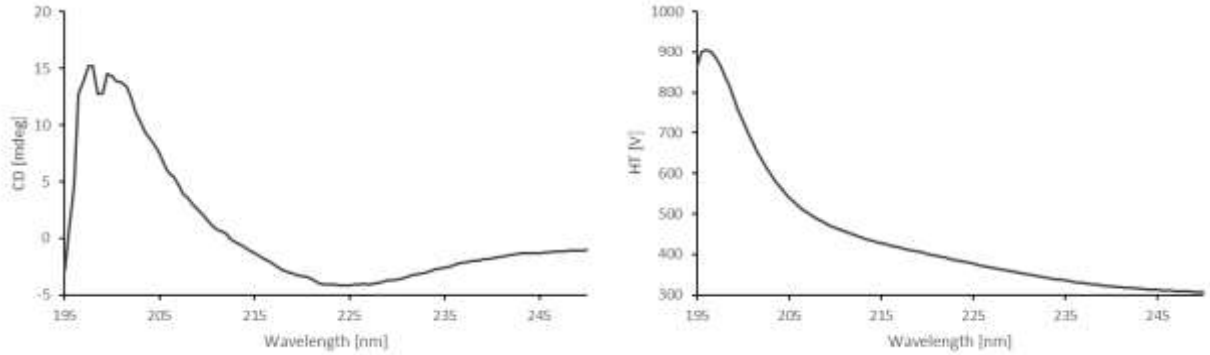

Figure 33: CD spectra of APMAP. CD spectra recorded of APMAP dialyzed in 10 mM Tris, pH 8.0. The negative bands at around 218 nm and positive bands at 195 nm indicate well-defined antiparallel β-sheets.

Based on these results, the chosen buffer system is rendered suitable for APMAP purification and pursuing further experiments. Concentration of the protein above to concentrations above 0.8 mg/mL has so far been unsuccessful. For precipitation tests of APMAP, the concentration is too low to obtain any precipitation, hence, crystallization screens can so far not be set up.

4.3 Neutralizing Monoclonal Antibodies against JCPyV

4.3.1 Interactions between scFv 29B1 and JCPyV and BKPyV VP1

Experimental Design

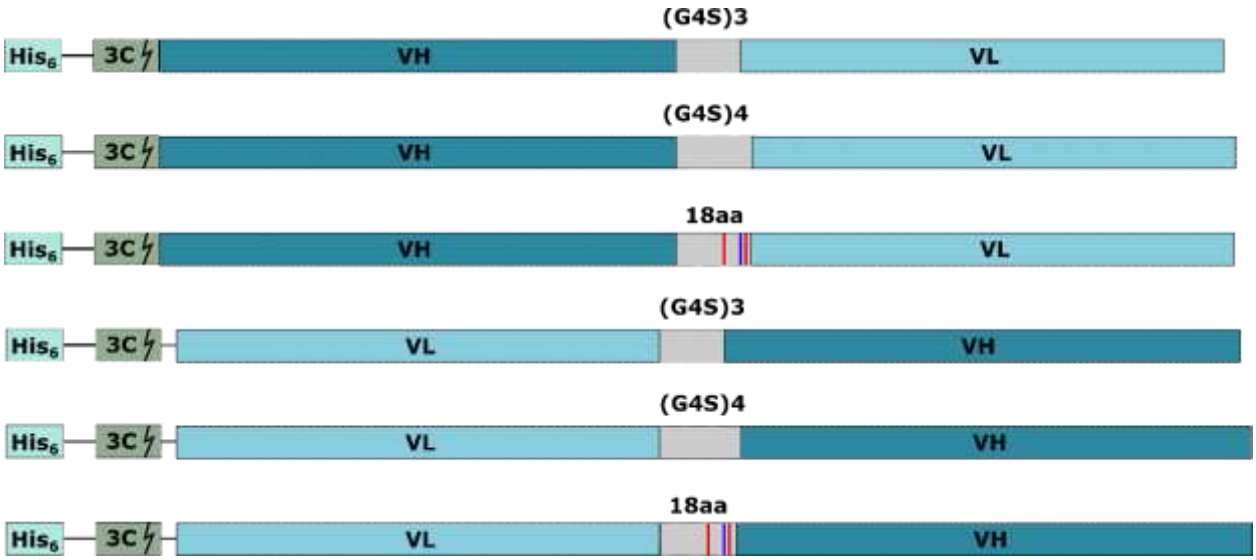

Figure 34: Schematic representation of 29B1 scFv constructs. All constructs were cloned into a pET47b vector and are comprised of V_H, V_L and a variable linker. The linker varied in length (15-20 aa) as well as in amino acid composition. The constructs containing the 18 aa linker contained three charged residues; two lysines shown in red and a glutamate shown in blue.

Antibody 29B1 was designed as scFv with two different orientations of V_L and V_H (V_L – linker – V_H and V_H – linker – V_L) to ensure that neither linker nor His-tag would interfere with antibody binding to VP1 (Figure 34). The constructs contained different types of linker, which varied in length (ranging from 15 to 20 aa) and amino acid composition. Charged residues were included to enhance protein solubility (Whitlow et al. 1993).
After expression and solubility tests of the designed scFv-constructs, construct V_L-V_H (18aa) was chosen for purification and crystallization experiments. Based on the solubility tests, buffer 12 (Table 7) was selected for the following purification experiments.

Purification and Characterization of scFv 29B1
Ni-affinity chromatography was performed as the first purification step. The elution profile (Figure 35B) shows elution of the protein of interest at an imidazole concentration of 100 mM. Elution peak fractions hardly show any impurities as indicated by the samples analyzed via SDS-PAGE (Figure 35A). Fractions were pooled and subjected to HRV 3C protease cleavage. Complete cleavage of the 29B1 scFv was achieved by using a ratio of 1 mg of protease per 10 mg of fusion protein.

Cleaved protein was separated from uncleaved protein via a second Ni-affinity chromatography step.

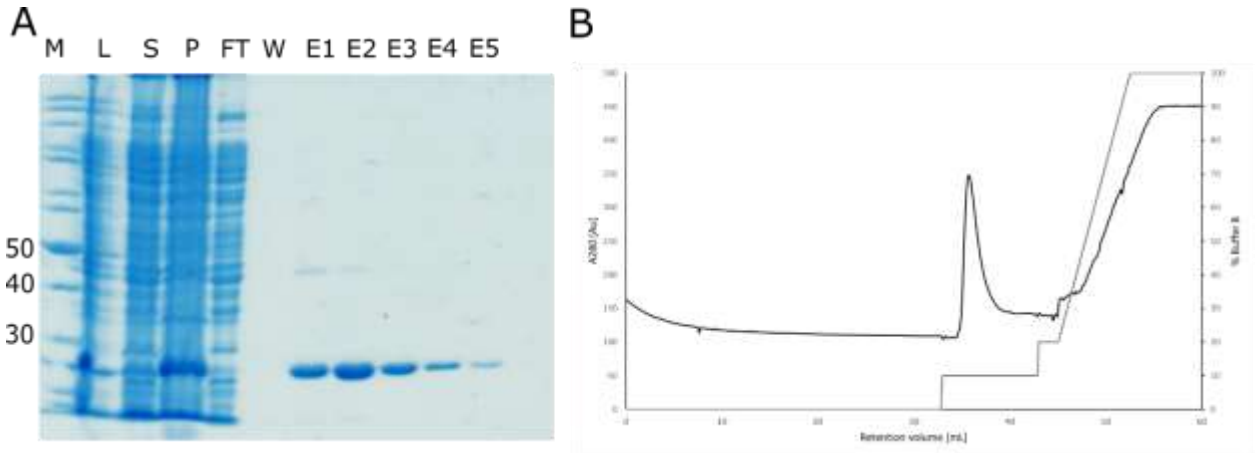

Figure 35: Purification of the 29B1 scFv V_L-V_H (18aa). (A) SDS-PAGE analysis of purification trial of scFv 29B1. After lysis (L), the majority of the protein remains insoluble in the pellet fraction (P), however, decent amounts were soluble in the chosen buffer system (S) and subjected to Ni-affinity chromatography. Contaminants were removed in flow-through (FT) and wash step (W) and protein of interest eluted at about 100 mM imidazole as indicated by the thick band at the corresponding molecular weight (E1-E5). (B) Elution profile of Ni-affinity chromatography. Protein of interest eluted at about 100 mM imidazole.

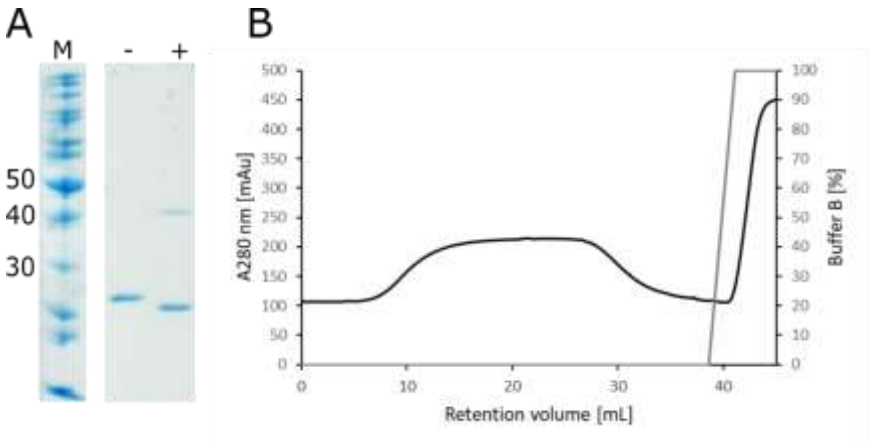

Figure 36: His-tag cleavage of scFv 29B1. (A) SDS-PAGE of HRV 3C cleavage of scFv 29B1. The His-tag was successfully removed as indicated by the shift of the band towards lower molecular weight values (- : before cleavage; + : after cleavage). (B) Wash profile of 2nd Ni-affinity chromatography of cleaved scFv 29B1. The absorbance is shown at 280 nm.

Complex Formation with JCPyV VP1 and Crystallization

Stable complexes of purified scFv 29B1 were formed with JCPyV VP1 and separated from free scFv via SEC. Protein crystals of the JCPyV VP1–29B1 scFv were set up and obtained at complex concentrations of 1.6 – 2.9 mg/mL in various conditions using the sitting-drop vapor diffusion method. A dataset at 3.1 Å was obtained for crystals grown in a condition containing 0.2 M trimethanolamine N-oxide, 0.1 M Tris (pH 8.5), 20% PEG 2,000 with a complex concentration of 2.92 mg/mL. Mother liquor

supplemented with 20% (v/v) glycerol was used as cryoprotectant. Diffraction data were processed, and structure determination was performed via molecular replacement using JCPyV VP1 (PDB ID: 3NXG) and the recently solved crystal structure from scFv 27C11.

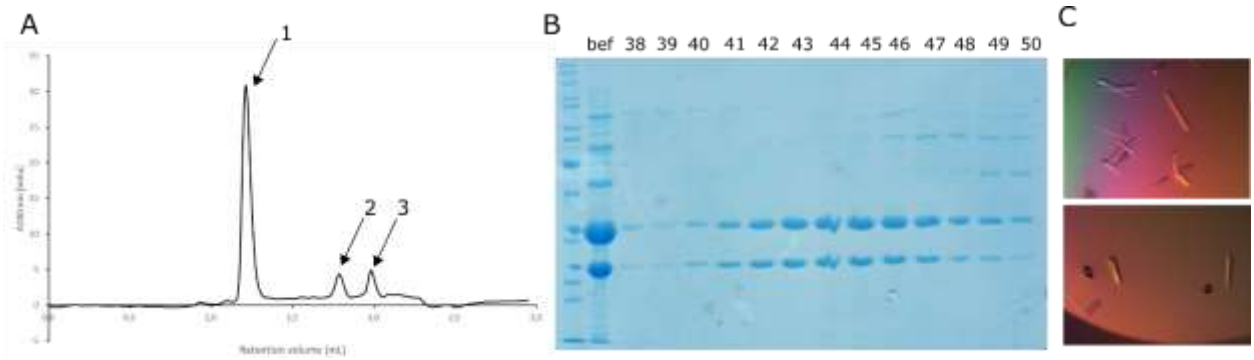

Figure 37: Purification and crystallization of JCPyV VP1 – scFv 29B1 complex. (A) Analytical size exclusion chromatogram of JCPyV VP1 – 29B1 complexes. The absorbance is shown at 280 nm. The complex could be purified as indicated by peak 1. Peak 2 and 3 contain unbound JCPyV VP1 and excess scFv 29B1. (B) SDS-PAGE of preparative SEC of JCPyV VP1 – 29B1 with a sample before SEC (bef) and samples of complex fractions. (C) Crystals of JCPyV VP1 – 29B1 complex in 0.2 M sodium thiocyanate, 20% PEG 3,350 at 20°C.

Crystal Structure of JCPyV VP1–29B1 Complexes

The complex structure of JCPyV VP1–29B1 was determined at a resolution of 3.1 Å in space group $P2_1$ with two JCPyV VP1–29B1 complexes in the asymmetric unit. One complex consists of one VP1 pentamer with five scFv bound to each of the VP1 monomers.

Table 18: Data collection and refinement statistics of JCPyV VP1 – scFv 29B1 complex

	JCPyV VP1 – 29B1
Data Collection	
Beamline	SLS X06DA
Space group	$P12_11$
a, b, c [Å]	124.1, 172.5, 159.7
β [°]	104.5
Resolution [Å]	48.5-3.1 (3.18–3.10)
Unique reflections	261376 (41722)
Total reflections	933910 (148603)
R_{meas} [%]	24.5 (63.8)
I/σI	7.2 (2.5)
$CC_{1/2}$ [%]	97.3 (76.4)
Completeness [%]	99.9 (99.6)
Wilson B-factor [Å^2]	36.4
Refinement	
R_{work}/R_{free} [%]	21.5 / 23.3
No. of atoms	
protein	37924
B-factor [Å^2]	

JCPyV VP1	38.0
scFv 29B1	61.8
R.m.s.d.	
Bond length [Å]	0.005
Bond angles [°]	1.13
Ramachandran [%]	
Favored	99.7
Outliers	0.3

The scFv V_H and V_L are well ordered and the interaction surface with JCPyV VP1 is well defined in the electron density map. The total surface area of 29B1 covers 835 Å^2 with the light and heavy chains contributing similarly to the binding interface (439 Å^2 and 394 Å^2, respectively).

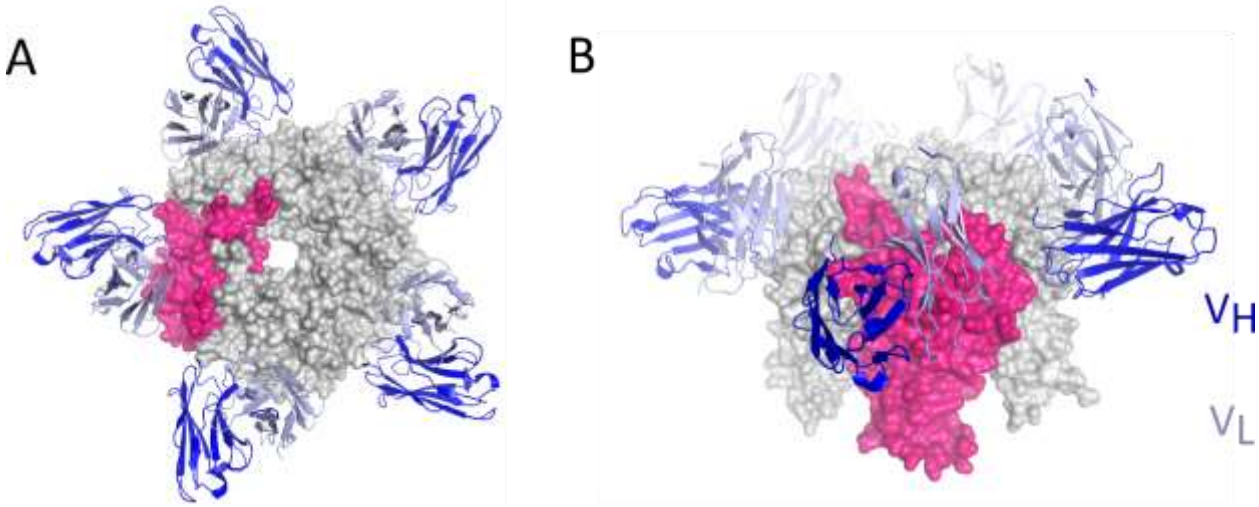

Figure 38: Crystal structure of JCPyV VP1 in complex with 29B1 scFvs. JCPyV VP1 is shown in surface representation with one monomer highlighted in pink. 29B1 is shown in cartoon representation with the light and heavy chain shown in light and dark blue, respectively. (A) Top view along the five-fold-axis of VP1. Five scFvs of 29B1 bind to the VP1 pentamer. (B) Side view, showing that 29B1 binds not on top of the VP1 pentamer, but rather towards the side.

JCPyV VP1 is exclusively contacted by the complementary-determining regions (CDRs) of 29B1. Five of the six CDRs are involved in binding to JCPyV VP1, only H1 is not involved in any of the interactions (Figure 39A). The body of the light chain V_L domain and its L1, L2 and L3 contact the underside of the BC2-loop and straddle the EF-loop. Substantial contacts are furthermore contributed by H3. Here, the surface packs flat against the VP1 EF-loop and interactions mainly involve several hydrogen bonds as well as salt bridges (Figure 39B). Furthermore, H3 residue F225 inserts into a small crevice lined by residues D49, E52 and R55 and interacts with the hydrophobic portions of these side chains. Hence, it augments the contacts formed by H3 (Figure 39C).

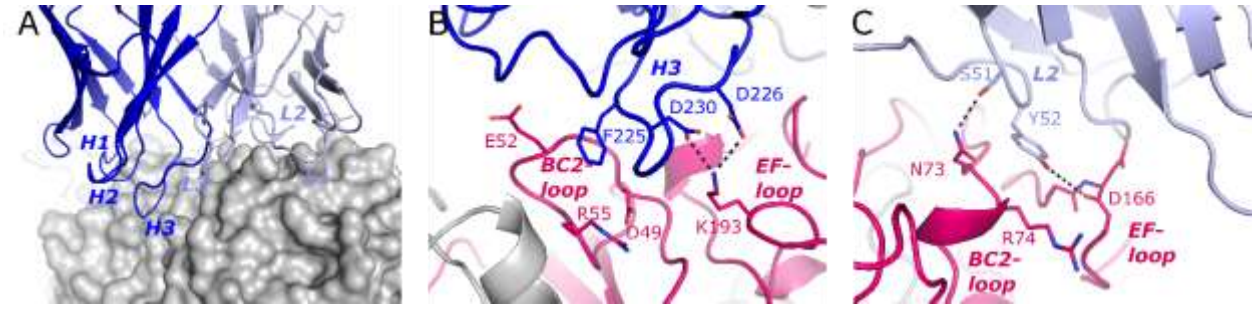

Figure 39: Contacts between JCPyV VP1 and scFv 29B1. JCPyV VP1 is shown in grey with one monomer highlighted in pink. Heavy chains of 29B1 are colored in dark blue, light chains in light blue. (A) Main interactions between JCPyV VP1 and CDRs of 29B1. All light chain CDRs (L1, L2 and L3) are involved in interactions with VP1, for the heavy chain CDRs only H1 is not part of the interactions. (B) Interactions between H3 and VP1 loops BC2 and EF. Several hydrogen bonds and salt bridges form a stable net of interactions. (C) Interactions between L2 residues S51 and Y52, which interact with N73 of the BC2-loop and D166 of the EF-loop, respectively.

Complex Formation with BKPyV VP1 and Crystallization

Stable complexes of purified scFv 29B1 were formed with BKPyV VP1 and separated from free scFv via SEC. Crystals of the BKPyV VP1–29B1 scFv were set up and obtained at complex concentrations of 3.5 mg/mL in various conditions using the sitting- and hanging-drop vapor diffusion method. Streak-seeding was performed to improve crystal quality using crystals from a condition containing 0.1 M sodium malonate (pH 5.5) and 14.4% PEG 3,350. Multiple datasets obtained resulted in pseudo-translation and could not be processed. A dataset without pseudo-translation at 2.6 Å was obtained for crystals grown in a condition containing 0.1 M sodium malonate (pH 5.25) and 14.4% PEG 3,350. Mother liquor supplemented with 20% glycerol was used as cryoprotectant. Diffraction data was processed, and structure determination was performed via molecular replacement using BKPyV VP1 (PDB ID: 4MJ1) and the recently solved crystal structure from scFv 29B1.

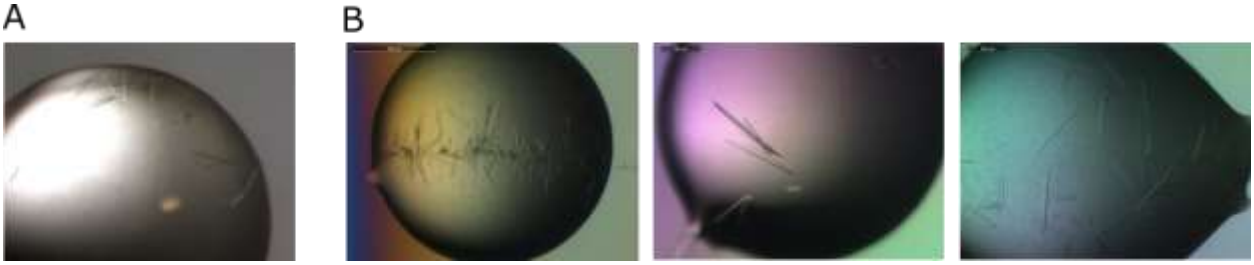

Figure 40: Crystals of BKPyV VP1–29B1 complex. (A) Initial crystal hits of BKPyV VP1–29B1 complex in 0.1 M sodium malonate, pH 5.5 and 14.4% PEG 3,350. (B) Crystal hits of BKPyV VP1–29B1 complex in 0.1 M sodium malonate, pH 5.25 and 14.4% PEG 3,350 obtained with streak seeding.

Crystal Structure of BKPyV VP1 – 29B1 Complexes

The complex structure of BKPyV VP1 – 29B1 was solved at a resolution of 2.94 Å in space group $P2_1$ with two JCPyV VP1 – 29B1 complexes in the asymmetric unit. As seen for the complex structure with JCPyV VP1, one complex consists of one BKPyV VP1 pentamer with five scFv bound to each of the VP1 monomers.

Table 19: Data collection and refinement statistics of BKPyV VP1 – scFv 29B1 complex

	BKPyV VP1 – 29B1
Data Collection	
Beamline	SLS X06DA
Space group	P1
a, b, c [Å]	114.6, 114.6, 142.3
β [°]	92.3, 106.0, 111.4
Resolution [Å]	49.2-2.65 (2.81–2.65)
Unique reflections	352876 (55527)
Total reflections	638907 (94181)
R_{meas} [%]	17.5 (73.9)
I/σI	5.86 (1.38)
$CC_{1/2}$ [%]	98.1 (61.8)
Completeness [%]	94.8 (92.4)
Wilson B-factor [Å^2]	34.0
Refinement	
R_{work}/R_{free} [%]	27.5 / 25.1
No. of atoms	
Protein	37679
B-factor [Å^2]	
BKPyV VP1	35.8
scFv 29B1	50.7
R.m.s.d.	
Bond length [Å]	0.011
Bond angles [°]	1.46
Ramachandran [%]	
Favored	95.2
Outliers	0.4

The binding mode of 29B1 in complex with BKPyV VP1 is almost identical to that seen in the JCPyV VP1 complex structure (Figure 41A). When the two VP1 pentamers are superimposed, the root mean square deviation (RMSD) between the bound scFvs in both complexes is only 0.60 Å^2. The total surface area buried upon scFv 29B1 - BKPyV VP1 complex formation is, with 830 Å^2, identical to the area buried in the JCPyV VP1-29B1 complex (835 Å^2). Only subtle differences characterize the binding of 29B1 to BKPyV VP1 compared to JCPyV VP1. Interactions differ only in two residues; JCPyV VP1 features an asparagine at position 73, which interacts with N55 of L2 of 29B1. This residue is replaced to a glutamate in the case of BKPyV VP1, hence the interaction is abolished (Figure 41B). JCPyV VP1 residue K193 interacts with H3 residues D226 and D230, BKPyV VP1 residue N201 cannot engage in these interactions (Figure 41C).

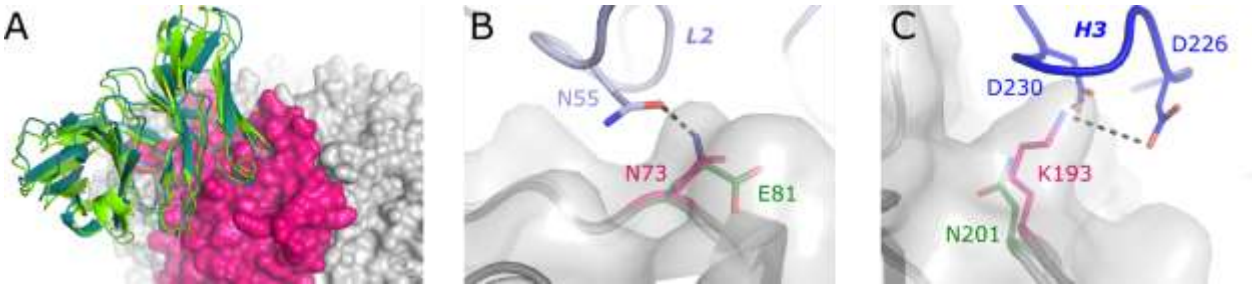

Figure 41: Binding of scFv 29B1 to BKPyV VP1 compared to JCPyV VP1. JCPyV and BKPyV VP1 are shown in surface representation in grey with one monomer highlighted in pink. 29B1 is shown in cartoon representation. (A) Superposition of 29B1 – JCPyV VP1 and 29B1 – BKPyV VP1 complex structures, with the JCPyV-bound scFv 29B1 shown in deep teal and the BKPyV-bound scFv 29B1 colored in chartreuse. (B) Residue N73 of JCPyV VP1 (shown in pink) is involved in interactions with L2 residue N73. BKPyV VP1 E81 (shown in green) cannot engage in this interaction. (C) Residue K193 in JCPyV VP1 (shown in pink) interacts with residues D226 and D230 of H3 of 29B1. BKPyV VP1 N201 (shown in green) cannot engage in these interactions.

4.3.2 Interactions between Fab 72F7 and JCPyV VP1

Experimental Design

For the purification strategy of 72F7, a similar approach was conducted as for 29B1. Several scFv constructs were designed with different V_L and V_H orientations as well as varying linker lengths and compositions. However, none of these constructs could be successfully purified. For some constructs, protein overexpression could not be achieved, for other constructs good overexpression was achieved, but they later failed to show solubility in any of the tested buffers. Eventually, different purification strategies could be tested for one construct, involving different *E. coli* strains and expression conditions, various buffer systems and supplements, different affinity columns (Ni-resin, Co-resin, CaptoL-resin) and co-purification with JCPyV VP1, but none of these strategies resulted in the successful purification of scFv 72F7.

Hence, for 72F7, the already established purification protocol for Fabs was adopted. Stable Fabs of 72F7 were produced and used for complex formation with JCPyV VP1 (Figure 42A). Complexes were purified and separated from excess Fabs by SEC (Figure 42B).

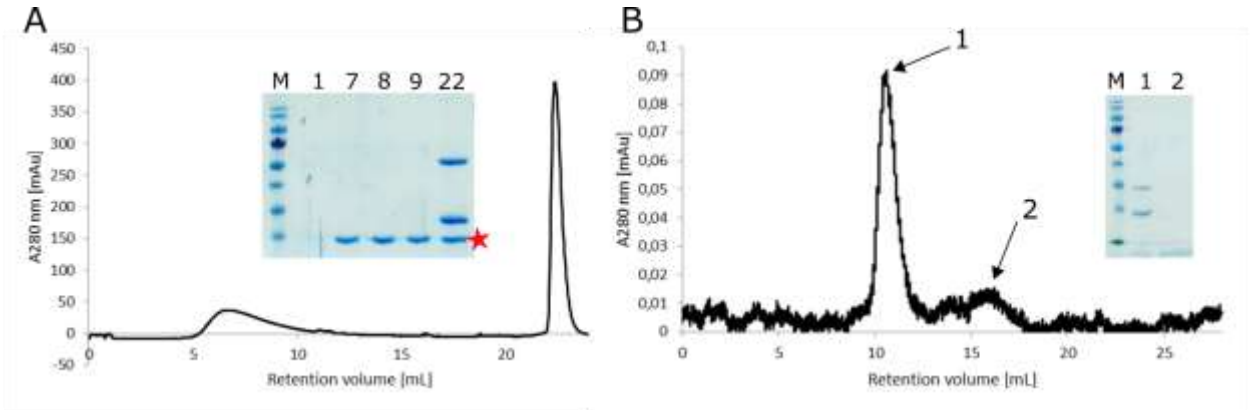

Figure 42: Purification of 72F7 Fabs and JCPyV VP1-72F7 Fab complexes. (A) Protein A chromatogram of papain-digested mAb 72F7 with the absorbance shown at 280 nm. The first peak (fractions 7, 8 and 9) contains the purified Fab and the second peak (fraction 22) all antibody fragments including Fc. Results were confirmed via SDS-PAGE. Light and heavy chain have a molecular weight of ~24 kDa. (B) Size exclusion chromatogram with the absorbance shown at 280 nm. The JCPyV VP1-72F7 Fab complex peak (peak 1) is separated from excess Fabs (peak 2). The SDS-PAGE shows bands at the corresponding molecular weights. Light and heavy chain of 72F7 have molecular weights of ~24 kDa, a monomer of JCPyV VP1 has a molecular weight of ~32 kDa.

Commercial crystallization screens were set up with purified JCPyV VP1-72F7 complexes and micro-seeded with crystals obtained in 0.06 M divalent ions, 0.1 M buffer system 2, pH 7.5, 37.5% (v/v) precipitant mix 4 (Morpheus HT screen, Molecular Dimensions) and yielded several conditions with crystal hits (Figure 43).

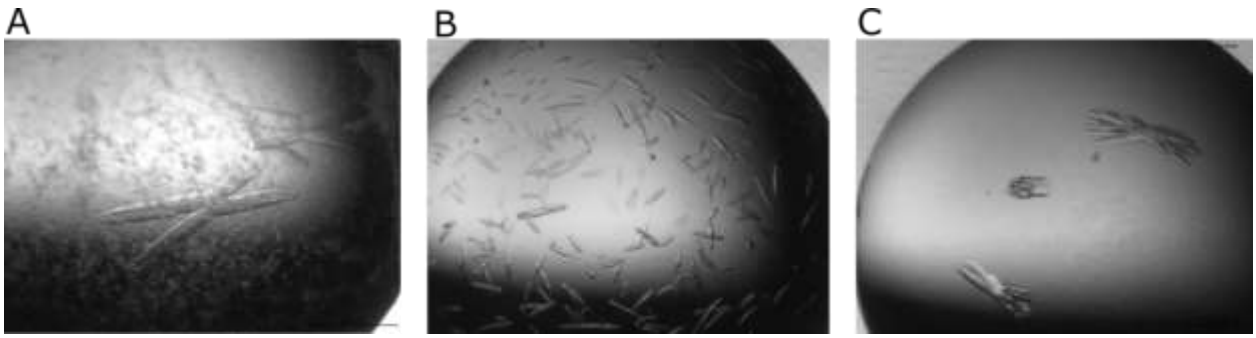

Figure 43: Crystals of JCPyV VP1–72F7 complex. (A) Crystal hits of JCPyV VP1–72F7 complex in 0.09 M NPS, pH 5.5, 0.1 M buffer system 3, pH 8.5 and 30% precipitant mix 3 (Morpheus screen, Molecular Dimensions). (B) Crystal hits of JCPyV VP1–72F7 complex in 0.05 M citric acid, pH 5.0 and 16% PEG 3,350 (PEG/Ion screen, Hampton Research). (C) Crystal hits of JCPyV VP1–72F7 complex in 0.1 M succinic acid, pH 7.0 and 12% PEG 3,350 (PEG/Ion screen, Hampton Research).

5. Discussion

5.1 Fragment-based Screening with JCPyV

Knowledge of the structure of a protein target can guide the design of new therapeutic agents through FBDD. This approach is used in the identification of ligand fragments and subsequent design of high-affinity ligands that bind to a critical site and thereby inhibit protein function. A prominent example are the FDA-approved drugs Vemurafenib, a B-Raf enzyme inhibitor for the treatment of late-stage melanoma, and Venetoclax, a treatment for chronic lymphocytic leukemia (Bollag et al. 2012; Hortobagyi et al. 2016; Singh, Tam, and Akabayov 2018).

Drugs targeting viral receptor proteins block the first events in the viral replication cycle and are less constrained by intracellular delivery or metabolism. Preventing the virus from entering the host cell inhibits its replication and possible mutation that could translate into drug resistance (De Clercq 2002; Munch et al. 2007; Dwyer et al. 2007).

The major capsid protein VP1of JCPyV harbors the receptor binding site for LSTc and thus represents a potential target for antiviral compounds. Compounds 9E08 and 13A06 were shown to bind to JCPyV VP1. Both compounds share the same binding site located on the inside of the JCPyV VP1 pentamer, rather than near the receptor binding site on the surface-exposed loops on the outside of the virion. However, attempts to design more potent compounds based on these results or based on the VP2 sequence resulted in compounds binding to JCPyV VP1.

X-ray crystallography is the preferred method for elucidating the three-dimensional structure of protein-ligand complexes. It provides information about where and how the ligand binds to the protein, however it can be challenging due to following aspects. In order to resolve the electron density for the screened ligand, a reasonably high resolution (1.5-2.5 Å) is needed. Conversely, this requires high concentrations (25-100 mM) (Jhoti et al. 2007) and/or long soaking times of the compound to overcome the low binding affinity. Achieving high concentrations is hampered due to the inherent poor solubility of many compounds in aqueous solutions. Higher soaking times in turn bear the risk of damaging the crystal resulting in weaker diffraction.

Generally, limited binding constants of ligands cause binding sites to be only partially occupied, leading to proportionally weaker electron density. Additionally, binding sites have the tendency to scavenge all kinds of molecules present in the purification or crystallization environment (e.g. buffer molecules or ions), resulting in weak density of unknown origin that is not suitable for placing a model. This is also the case for the apo-structure of JCPyV VP1, which generally exhibits some electron density in the binding site for 9E08 and 13A06. This existing electron density could overlay the weak electron density for partially bound ligands. The mistake of placing a ligand in poorly defined electron density can simply be avoided by critical examination of the existing density for the ligand at a reasonable contour level.

Yet, only tightly bound parts of the ligand may have distinct density, where ligands could be modeled in. If compounds are present in multiple conformations, as has been observed for compound 13A06, this could further decrease the electron density levels.

All these considerations lead to a high rate of false-negatives in crystallography for weak affinity fragments, in particular with the compound-soaking approach. The success rate in crystallography of compounds identified in NMR compound screens is about 5-10% (Chilingaryan, Yin, and Oakley 2012; Mashalidis et al. 2013; Hajduk and Greer 2007; Wielens et al. 2013). This rate is even lower from hits identified via computational methods, explaining the underlying results for this research projects, where only 2 out of 30 tested compounds identified in NMR screening experiments could be confirmed in binding JCPyV VP1 in crystal soaking experiments and none of the six tested from molecular docking studies. Compounds 9E08 and 13A06 were tested for their anti-viral activities in JCPyV pseudovirus infectivity assays in SVG-A cells. Compound 9E08 significantly blocked infection at a concentration of 10 mM. Compound 13A06 showed some inhibition, which was however not significant. Two additional compounds, 2D05 and 7D04, which did not show binding to JCPyV VP1 in crystal soaking experiments, demonstrated no activity in the inhibition of JCPyV pseudovirus (Walter Atwood, personal communication).

Since the compound binding site on JCPyV VP1 overlays with the proposed VP2 binding site, another approach employed the design of small peptides covering the C-terminal sequence of JCPyV VP2. These VP2 derived peptides were subjected to crystal soaking and co-crystallization experiments with JCPyV VP1. For co-crystals of JCPyV VP1 and the VP2 derived peptides, additional electron density could be observed in the simulated annealing electron difference maps. This additional density was located inside of the VP1 pentamer along the fivefold symmetry axis, indicating binding had occurred. Yet, the difference omit map was not traceable and could not be assigned to any peptide structure due to the averaging of the electron density in the five-fold symmetry. It is therefore impossible to conclude something about the binding mode of the peptide or the specific interactions utilized for binding.

In order to lock the VP2 derived peptides in their binding position, it might be useful to elongate the peptide sequence. The elongated peptide structure could serve as an anchor binding to the outside of the VP1 pentamer and thereby locking the peptide in its binding position. If the resulting crystal packing is then asymmetric, this in turn would prevent averaging of the electron density in the five-fold symmetry.

Identifying specific interactions mediating peptide binding to JCPyV VP1 would help in the design of more potent fragments, which could compete with JCPyV VP1 and VP2 binding. The ultimate goal is to find compounds that are able to block virus receptor interactions or interfere with virus assembly. The LSTc binding pocket is not targeted by any of the screened components, however, the binding site of fragments which showed binding to JCPyV was located on the inside of the VP1 pentamer involving the proposed VP2 binding site.

5.2 Adipocyte Plasma Membrane-Associated Protein

The adipocyte plasma membrane-associated protein APMAP was identified as a putative receptor for JCPyV by the group of Walter Atwood, Brown University. Little is

known about this 46 kDa glycosylated type II transmembrane protein with potential hydrolase activity and calcium binding (Bogner-Strauss et al. 2010).
The extracellular domain of APMAP, which contains the two glycosylation sites, is predicted to adopt a six-bladed β-propeller with each blade containing a twisted four-stranded antiparallel β-sheet. The blades are radially arranged around a pseudo-six-fold axis.
Analysis of the sequence architecture from earlier studies revealed four segments: two non-globular segments (region 1-40 and the proline-rich linker 62-89), a predicted transmembrane helical region (amino acids 41-61) and a predicted C-terminal globular domain starting with residue 90. This globular domain is assigned two enzymatic domains with conflicting properties. The first predicted domain is a calcium-binding superficial gray layer full domain and the second prediction is the strictosidine synthetase domain fragment, a domain without metal ions. Alignment of APMAP orthologues in animal genomes reveals four conserved sites at position E103, N201, N260 and D306/N307 that are predicted to be necessary for calcium-binding in the active site (Bogner-Strauss et al. 2010). Although the C-terminal domain of APMAP is predicted to fold into a six-bladed β-propeller, the protein does not belong to the family of strictosidine synthetase-type enzymes. The conservation of functional residues necessary for calcium-binding clearly indicate a hydrolase structure with a calcium binding active site and not that of Rauvolfia strictosidine synthetase that is known not to bind any metal ions.
In order to elucidate the structure and function of the molecule, the goal was to establish a purification and crystallization protocol for the extracellular domain of APMAP, the part of the transmembrane protein that would be expected to act as the putative JCPyV receptor. Three constructs comprising the extracellular domain of APMAP were designed and subjected to expression tests, solubility tests and initial purification trials. While the first construct (62-416) could be expressed and purified, this could only be achieved by the usage of detergents. Crystallization of the protein resulted in crystals, which diffracted to low resolution and lacked a clearly defined diffraction pattern. Thus, these crystals could not be used for structural analysis.
Although structure prediction programs render residue 62 and following residues as part of the extracellular domain, there is still a slight chance that these N-terminal residues of the construct belong to the transmembrane part of the protein or show strong hydrophobic characteristics, having stark tendencies to adhere to membranes. Therefore, two additional constructs starting further upstream at residue 80 were designed to exclude this possibility. In order to establish a stronger binding to the Ni-column, the His-tag was extended. The second construct (80-416) with a C-terminal His_8-tag did not show any overexpression after the addition of IPTG, indicating leaky expression, and hence was rejected for further experiments. Finally, the third construct (80-416) with N-terminal His_8-tag showed promising results by the application of a refolding protocol from inclusion bodies (protocol adopted from (Ponassi, Cantoni, Biassoni, Conte, Spallarossa, Pesce, et al. 2003; Ponassi, Cantoni, Biassoni, Conte, Spallarossa, Moretta, et al. 2003)).
Expression at low temperature conditions leads to the increase of stability and correct folding patterns due to the fact that hydrophobic interactions determining inclusion body formation are temperature dependent (Khow and Suntrarachun 2012). In the

case of APMAP, the protein was prone to form inclusion bodies even at low expression temperatures, resulting in selecting a refolding purification strategy from inclusion bodies. This protocol resulted in high yields of refolded protein, yet, the composition of the refolding buffer presented several challenges regarding the next purification steps. Since neither dialysis in the proposed buffer system (Ponassi, Cantoni, Biassoni, Conte, Spallarossa, Moretta, et al. 2003) nor Ni-affinity chromatography could be applied, different buffer systems were sampled in a small-scale dialysis set-up. The protein was stable and showed only minor aggregation in a buffer without any supplied salts adapted from the purification protocol of STR1 (Ma et al. 2004).

For its role as putative JCPyV receptor, the two glycosylation sites of APMAP could be required for the interaction with the viral protein. Protein glycosylation is common in eukaryotic cells and is of particular importance in protein-protein interactions. Glycans are abundant on host cells and the majority of mammalian virus receptors are N-glycosylated (Zhang et al. 2019). The N-glycosylation sites of HTR2A, the receptor for JCPyV, are reported to be important for viral infection (Maginnis et al. 2010). Furthermore, studies showed that protein glycosylation might have an effect on protein folding and stability (Mitra et al. 2006; Shental-Bechor and Levy 2008; Xu and Ng 2015), however, the effect of glycosylation is not elucidated in the case of recombinantly expressed APMAP.

Protein glycosylation often contributes to high protein solubility and increases its stability against proteolysis. Not only could the glycosylation of APMAP aid in protein solubility and folding, it might also play a role in the attachment to JCPyV VP1. One major disadvantage of the recombinant protein expression in the prokaryotic system *E. coli* is not only the protein segregation into inclusion bodies, which could be overcome by protein refolding, but the limited eukaryotic post-translational machinery function, involving the complex process of glycosylation. Hence, adaptation to a eukaryotic expression system for the recombinant protein production of APMAP should be pursued in the future.

5.3 Neutralizing antibodies against JCPyV and BKPyV

Interactions of neutralizing antibodies with JCPyV VP1

JCPyV VP1 and BKPyV VP1 share 78% sequence identity, with lower conserved regions located on top of the VP1 pentamer comprising the receptor binding site and surface-exposed loop regions. Higher conserved regions can be found towards the side of the pentamer (Figure 44). Three of the four studied antibodies were shown to bind towards the top of the VP1 pentamer. MAbs 98D3, 27C2 and 27C11 interact with the less conserved regions of JCPyV VP1 involving the receptor binding site. 29B1 binds to an epitope at the side of VP1 that is highly conserved between JCPyV and BKPyV VP1. In contrast to antibodies 98D3, 27C2 and 27C11, the 29B1 epitope does not overlap with the glycan binding site, which is formed by the protruding BC1-, BC2, and DE- and HI-loops on the outer surface of the pentamer (Figure 45). Nevertheless, all of the studied antibodies exhibit neutralizing capacities against JCPyV. Antibodies

98D3, 27C2 and 27C11 presumably neutralize by directly blocking the LSTc binding site, whereas the neutralizing capabilities of 29B1 could be mediated by sterical hindrance, which would occlude the virus from reaching and engaging the receptor.

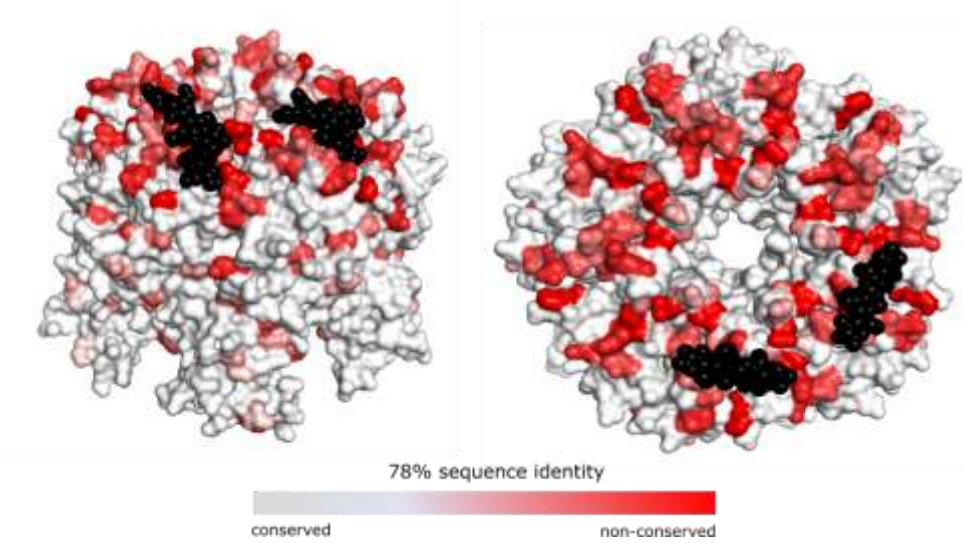

Figure 44: Surface conservation between JCPyV and BKPyV VP1. Surface representation of JCPyV VP1 with residues colored according to their level of conservation, with grey indicating highly conserved residues and red signifying non-conserved residues. LSTc is shown in black spheres.

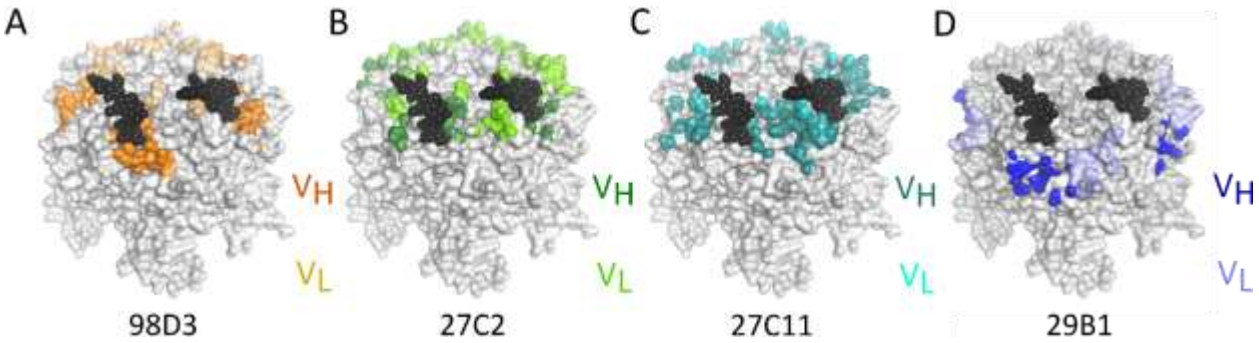

Figure 45: Comparison of interaction surfaces of 98D3, 27C2, 27C11 and 29B1 and position of the receptor binding site. JCPyV VP1 pentamers are shown in surface representation (grey) with the bound LSTc glycan shown in black sphere representation. Epitopes on the surface are color-coded by V_H and V_L chain of antibody 98D3 (panel A), 27C2 (panel B), 27C11 (panel C) and 29B1 (panel D) within a range of 4.5 Å.

The individual interactions with JCPyV VP1 differ among the investigated antibodies, whereas antibodies directly blocking the receptor binding site all involve a hydrophobic pocket on JCPyV VP1 that normally harbors the N-acetyl group of the terminal sialic acid moiety of LSTc.

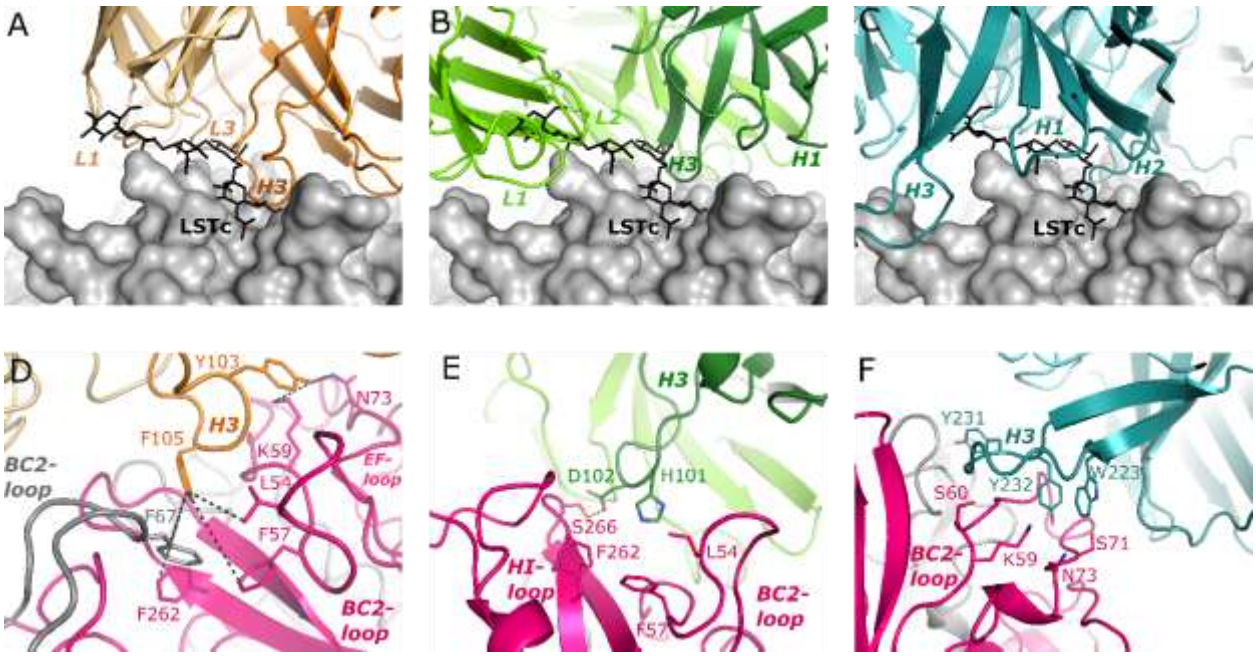

Figure 46: Key interactions of 98D3, 27C2 and 27C11 with JCPyV VP1. (A, B, C) Surface representation of JCPyV VP1 colored in grey with LSTc shown in black stick representation. The heavy and light chains of 98D3 (A), 27C2 (B) and 27C11 (C) are color coded with darker and lighter colors. (A) V_H and V_L of 98D3 are shown in dark and light green, respectively. Fab loops L1, L3 and H3 cover the receptor-binding pocket, blocking LSTc recognition. (B) V_H and V_L of 27C2 are shown in dark and light blue, respectively. Fab regions L1, L2, H1 and H3 cover the receptor-binding site, blocking LSTc recognition. (C) V_H and V_L of 27C11 are shown in cyan and deep teal, respectively. The three heavy chain CDRs H1, H2 and H3 straddle the BC2-loop. (D) Key interactions are shown between L1 and L3 of 98D3 and the DE- and HI-loop as well as the DE-loop of the neighboring VP1 monomer as black dashed lines. (E) Interactions between H3 and the HI- and BC2-loops of JCPyV VP1. Residue H101 at the tip of H3 inserts into the hydrophobic pocket of JCPyV VP1 that is lined with residues L54, F57, F262 and S266. Residue D102 in H3 furthermore forms a hydrogen bond with the side chain of S266 in the VP1 HI-loop. (F) Interactions between residues of H3 of 27C11 and the BC2-loop residues of JCPyV.

The human antibody 98D3 mainly interacts with JCPyV VP1 via H2 and H3, with H3 inserting into the hydrophobic pocket. Here, residue F105 at the tip of H3 is involved in hydrophobic interactions with phenylalanines F57, F67 and F262 as well as L54 of VP1. Hydrophobic interactions can also be observed between H3 residue Y103 and the side chain of residue K59 of VP1. Vital interactions between JCPyV VP1 and LSTc are mediated by residues 54, 57, 59 and 67 of VP1. Further interactions involve hydrogen bonds between L1 and L3 and the DE- and HI-loops of JCPyV VP1. The contacts bridge two VP1 monomers with residue N31 (L1) and residue (L3) interacting with residue R265 in the VP1 DE-loop and S93 in the DE-loop from the neighboring monomer, respectively.

For antibody 27C2 key contacts with JCPyV VP1 are formed by L1 and L3 and H1 and H3 of 27C2. Again, H3 inserts into the hydrophobic pocket with residue H101 at its tip placed above the pocket lined with residues L54, F57, F67 and F262. H3 residues form hydrogen bonds with the HI-loop of JCPyV VP1and the DE-loop of the neighboring VP1 monomer, hereby bridging the two VP1 subunit. A major contact is between H3 residue D102 and HI-loop residue S266, which is a major PML-mutation hotspot. Additional contacts are formed between several H1, L1 and L2 residues and

the BC1- and BC2-loop. One of these interactions is a hydrogen bond between L1 residue N32 and VP1 residue K59.
All three heavy chain CDRs of mAb 27C11 clasp the BC2-loop of JCPyV VP1, with H3 again approaching the sialic acid binding site, albeit not protruding deeply into the hydrophobic pocket like it is seen for 98D3 and 27C2. Rather, the mAb interacts with a cluster of surface-exposed residues (K59, S60, S71 and N73) through polar interactions. Some of these residues are involved in LSTc binding, hence, 27C11 directly interferes with the glycan binding. Four consecutive tyrosine residues (Y231, Y232, Y233 and Y234) together with aromatic residues Y32 and W223 in H3 are involved in extensive contacts with non-polar regions in the BC2- and adjacent DE-loop from the neighboring VP1-monomer.

Effects of PML mutations on antibody binding

JCPyV strains isolated from the serum, CSF and brains of PML patients often contain mutations in residues lining the LSTc-binding pocket on the apical surface of JCPyV VP1 (Gorelik et al. 2011; Reid et al. 2011; Neu et al. 2010; Maginnis et al. 2013). Dominant JCPyV VP1 mutations characteristic for PML are predicted to be under positive selection during the development of PML. These mutations lead to an altered glycan binding spectrum for infectious entry, but also enable the virus to escape the host-immune response (Ray et al. 2015; Sunyaev et al. 2009). Superpositions as well as modeling with the four JCPyV VP1-antibody complexes were performed in order to analyze how the most prominent PML-associated mutations would affect antibody binding.
For antibody 98D3 it was shown that it binds the characteristic PML mutation L54F but fails to recognize S266F and S268F/Y (Figure 9). Serines 266 and 268 are part of the interaction network between the antibody and JCPyV VP1 and replacement of either amino acid with a bulky phenylalanine or tryptophan would lead to direct steric clashes with H1 and H3 of 98D3. Residue L54, which is not directly involved in interactions with 98D3, could be replaced with a phenylalanine without consequences for antibody binding. The less frequently mutated residue K59 is directly interacting with H3, thus, mutating this residue to either M, E or N would negatively affect binding. Binding would also be affected if residue S60 is mutated, since it is also located at the direct binding interface.
Antibody 27C2 recognizes characteristic PML-mutations L54F and S268F but is not able to bind to S266F like observed for antibody 98D3 (Figure 9). This finding can be explained by the interaction formed between the backbone amide group of S266 and H3 of 27C2. An introduction of a bulky phenylalanine side chain at this position would cause steric clashes with H3 as well as L2. Residue K59 directly interacts with L1 residues of 27C2, hence mutations at this position would adversely affect the antibody binding. Substitutions of residues N264 and Q270, which are also affected by PML-mutations, would most probably negatively influence 27C2 binding, since these residues also line the binding interface.
Antibody 27C11 recognizes all three most frequently occurring PML-associated mutations (L54F, S266F and S268F). Compared to antibodies 98D3 and 27C2, the epitope of 27C11 is shifted away from the sialic acid pocket with the majority of

interactions involving the BC2-loop. PML mutation hotspots, L54, S266 and S268 are hereby not directly contacted by residues of 27C11 and the H3 region does not penetrate into the sialic acid binding pocket. Therefore, mutations at residues L54, S266 and S268 do not affect the binding of antibody 27C11. Mutations at position K59 are likely to affect binding as 27C11 H3 residues D225 and N227 form a salt bridge and a hydrogen bond with PML-mutation hotspot K59 in the JCPyV VP1 BC2-loop. In a PML mutant, these favorable interactions would be lost. Another BC2-loop residue, S60, is involved in interactions with H3 residues, which are most likely diminished in PML mutations S60T or S60P.

Antibody 29B1 binds to a highly conserved epitope between JCPyV and BKPyV. This epitope does not overlap with the glycan binding site formed by the protruding loops on the outer surface of the pentamer, hence, 29B1 binding is not affected by characteristic PML-associated mutations, which cluster in these loops. The three most frequently occurring mutations L54F, S266F and S268F are recognized by the antibody. It is highly unlikely that less frequent mutations such as K59M/E/N, S60P/T, D65H, N264D/T/S and Q270H affect binding of 29B1.

All studied antibodies, 98D3, 27C2, 27C11 and 29B1, display neutralizing capabilities, even though residues of the LSTc are not directly contacted as seen for antibody 27C11 and 29B1. In these cases, engagement of the bulky antibody by the virus could abolish access to the receptor, similar to what has been seen in other examples (Dietrich, Harprecht, and Stehle 2017).

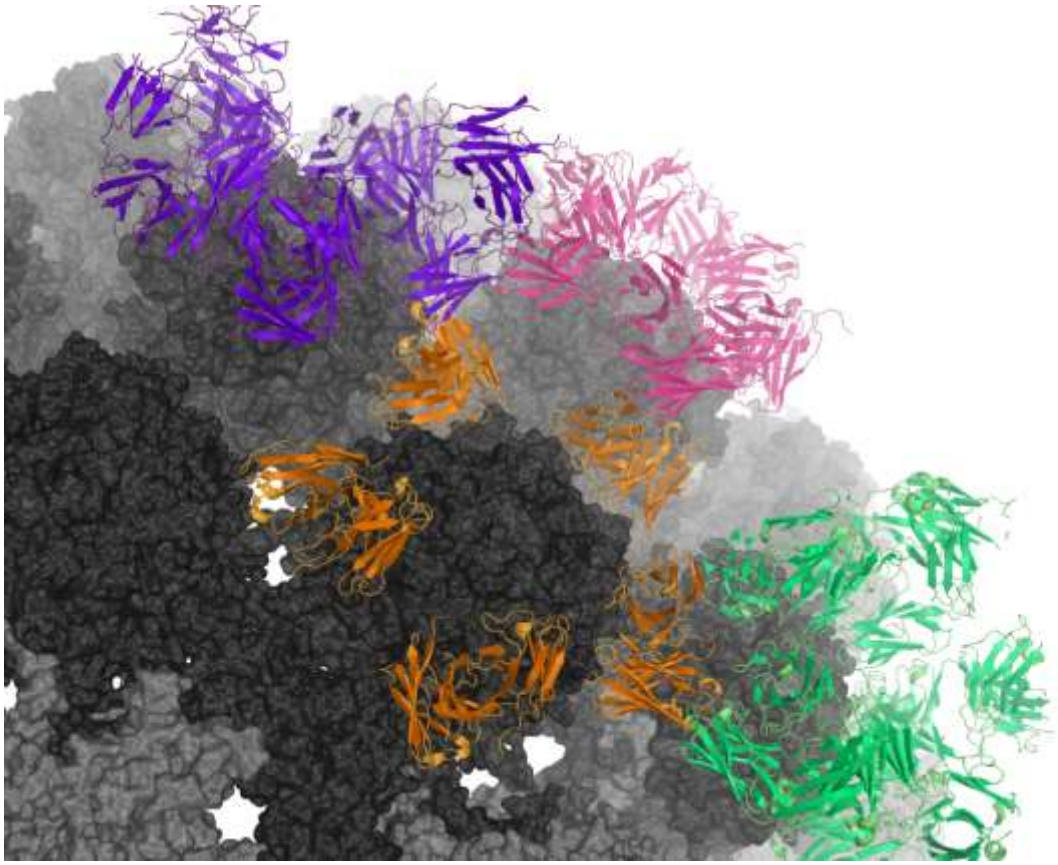

Figure 47: Model of mAb binding in JCPyV capsid context. Surface representation of the JCPyV capsid with bound mAb fragments shown in cartoon representation with 29B1 highlighted in orange, 27C11 in pink, 98D3 in purple, and 27C2 in green, respectively.

5.4 Conclusions and Outlook

The complex structure of JCPyV VP1 with four JCPyV-specific human mAbs as well as the complex structure of BKPyV VP1 with the cross-neutralizing mAb 29B1 helped in understanding the basis of the functionality and different specificity profiles by the underlying individual interactions. The selected mAbs can serve as lead candidates for the further development of a potential treatment of PML patients or patients at risk for PML (Jelcic et al. 2015). The approach of active or passive vaccination in order to stimulate protective adaptive immunity or as treatment in case of an ongoing disease can be accomplished by prophylactic and therapeutic immunization regimens (Jelcic et al 2015). Broadly neutralizing antibodies thus play a promising role in the treatment of viral infections, as has been shown for influenza, respiratory syncytial, Ebola and Zika viruses (Jelcic et al. 2017; Bornholdt et al. 2016; Corti et al. 2016; Sapparapu et al. 2016; Corti et al. 2013; Corti and Lanzavecchia 2013). The molecular mechanisms on how these antibodies exhibit cross-reactivity against the most common PML mutations as well as against BKPyV have broad implications for a rational design of vaccines and therapeutic antibodies (Bogdanoff et al. 2018; Jelcic et al. 2017).

Another approach for the rational design of JCPyV-antiviral therapeutics is the design of small molecule inhibitors of JCPyV in order to block the viral receptor attachment or interfere with viral assembly. In order to optimize the results described in this work, the design of the VP2 derived peptides could be improved with respect to not having a crystal symmetry averaged density in the experimental setup. Thus, molecular interactions could be clearly assigned and help thriving the development of more potent inhibitors. This could either be achieved by elongating the established VP2 derived peptide sequence to lock the fragment in place in order to achieve a non-averaged difference omit map in the crystallographic setup. Experimentally, co-crystallization as described in this thesis could be used for the formation of JCPyV VP1-peptide complexes. Another approach would be the co-expression of JCPyV VP1 together with the VP2 fragment as previously described (Chen, Stehle, and Harrison 1998).

As next steps in the further characterization of the putative JCPyV receptor APMAP interaction studies together with JCPyV VP1 are planned. Purified APMAP protein is incubated together with JCPyV VP1 and analyzed vie analytical SEC and surface plasmon resonance (SPR) in order to check for complex formation. A comparison with APMAP protein purified from eukaryotic cells would allow for the investigation in potential differences in JCPyV VP1 binding that would most likely arise from protein glycosylation. The ultimate goal is the crystallization and structural characterization of APMAP alone and in complex with JCPyV VP1 to examine the underlying molecular interactions.

6. Appendix

6.1 Antibody sequences with CDR annotations

98D3

VH

EVQLVESGGGVVQPGRSLRLSCAASGFTFSSSAMHWVRQAPGKGLEWVAVISYDGNNQLYADSVKGRLTISRDNSK
NALYLQLNSLRTEDTAVYFCARDGGGYSFGTYFFDFWGQGTLVTVSS

VL

DIQMTQSPSSLSASVGERVTITCRASQRISNYLNWYQQKPGKAPKLLIYAASTLQSGVPSRFSGSGSGTDFTLTIS
SLQPEDFATYYCQQSYSSPPTFGPGTKVDIK

27C2

VH

EVQLVESGGGLVKPGGSLRLSCAASGFTFSSYTMNWVRQAPGKGLQWVSSISSSSTYMYYGDSVKGRFTISRDNAR
NSLYLQMNSLRVEDTAVYYCARYAHDWNVDYWGQGTLVTVSS

VL

QSVLTQPPSASGTPGQRVTISCSGGSSNIGSNPVNWFQQFPGTAPKLLIYANTQRPSGVPDRFSGSKSGTSVSLAI
SGLQSEDEGDYHCAAWDDSLKGWVFGGGTKLTVL

27C11

VH

QVQLQESGPGLVKPSGTLSLTCAVSGDSISSSNWWSWVRQPPGKGLEWIGEIYHSGGTKYNPSLKSRVTISVDKSK
NHFSLKLRSVTAADTAVYYCARNRWFDNNRGGYYYYGMDVWGQGTTVTVSS

VL

DIQMTQSPSSLSASVGDRVTITCRASQGISSYLNWYQQKPGKAPKLLISATSDLQSGVPSRFSGSGSGTDFTLTIS
SLQPEDFATYYCQQSYSTPYTFGQGTKLEIK

29B1

VH

EVQLVESGGGLVKPGGSLRLSCAASGITFQYYAMNWVRQAPGKGLEWVSSIGGRGDTTYYTDSVKGRFTISRDNSK
STLYLQMNSLRAEDTAVYYCAKEPFDSSGDHRGVFDYWGQGTLVTVSS

VL

SYVLTQPPSVSVAPGKTARITCGGNNIGSRSVHWYQHKPGQAPVMIISYDMNRPSGIPERVSGSNYGNTATLTISR
VEAGDEADYYCQVWDSRSDHPYVFGTGTRVTVL

Sequence alignment heavy chains

```
98D3        EVQLVESGGGVVQPGRSLRLSCAASGFTFSSS-AMHWVRQAPGKGLEWVAVISYDGNNQL
27C2        EVQLVESGGGLVKPGGSLRLSCAASGFTFSSY-TMNWVRQAPGKGLQWVSSISSSSTYMY
27C11       QVQLQESGPGLVKPSGTLSLTCAVSGDSISSSNWWSWVRQPPGKGLEWIGEIYHSGGT-K
29B1        EVQLVESGGGLVKPGGSLRLSCAASGITFQYY-AMNWVRQAPGKGLEWVSSIGGRGDTTY
            :*** *** *:*:*. :* *:**.** ::.      **** *****:*:. *   .

98D3        YADSVKGRLTISRDNSKNALYLQLNSLRTEDTAVYFCARDGGG---YS-FGTYFFDFWGQ
27C2        YGDSVKGRFTISRDNARNSLYLQMNSLRVEDTAVYYCARYAHD---------WNVDYWGQ
27C11       YNPSLKSRVTISVDKSKNHFSLKLRSVTAADTAVYYCARNRWFDNNRGGYYYYGMDVWGQ
29B1        YTDSVKGRFTISRDNSKSTLYLQMNSLRAEDTAVYYCAKEPFD---SSGDHRGVFDYWGQ
            *  *:*.*.*** *:::. : *::.*: . *****:**:               .* ***

98D3        GTLVTVSS     123
```

```
27C2        GTLVTVSS     118
27C11       GTTVTVSS     127
29B1        GTLVTVSS     124
            ** *****
```

Sequence alignment light chains

```
98D3        DIQMTQSPSSLSASVGERVTITCRA--SQRISNYLNWYQQKPGKAPKLLIYAASTLQSGV
27C2        -QSVLTQPPSASGTPGQRVTISCSGGSSNIGSNPVNWFQQFPGTAPKLLIYANTQRPSGV
27C11       DIQMTQSPSSLSASVGDRVTITCRA--SQGISSYLNWYQQKPGKAPKLLISATSDLQSGV
29B1        -SYVLTQPPSVSVAPGKTARITCGG--NNIGSRSVHWYQHKPGQAPVMIISYDMNRPSGI
               :  .* * * : *. . *:* .  .:  *  ::*:*: ** ** ::*       **:

98D3        PSRFSGSGSGTDFTLTISSLQPEDFATYYCQQS---YSSPPTFGPGTKVDIK      107
27C2        PDRFSGSKSGTSVSLAISGLQSEDEGDYHCAAWDDSL-KGWVFGGGTKLTVL      110
27C11       PSRFSGSGSGTDFTLTISSLQPEDFATYYCQQS---YSTPYTFGQGTKLEIK      107
29B1        PERVSGSNYGNTATLTISRVEAGDEADYYCQVWDSRSDHPYVFGTGTRVTVL      109
            *.*.***  *.  :*:** ::  * . *:*          .** **:: :
```

APMAP alignment with STR1 (PDB ID 3V1S) for secondary structure prediction

```
APMAP   ESPIDPQPLSFKEPPLLLGVLHPNTKLRQAERLFE-NQLVGPESIA-HIGDV-MFTGTADGRVVKLEN-G-EIETIARFG
3v1s.1  -------------------------------KEILIEAPSYAPNSFTFDSTNKGFYTSVQDGRVIKYEGPNSGFVDFAYAS

APMAP   S----GPCKTR---DDEPVCGRPLGIRAGP-NGTLFVADAYKGLFEVNPWKREVKLLLSSETPIEGKNMSFVNDLTVTQ-
3v1s.1  PYWNKAFCENSTDAEKRPLCGRTYDISYNLQNNQLYIVDCYYHLSVVGSEGGHATQL---ATSVDGVPFKWLYAVTVDQR

APMAP   DGRKIYFTDSSSKWQRRDYLLLVMEGTDDGRLLEYDTVTREVKVLLDQLRFPNGVQLSPAEDFVLVAETTMARIRRVYVS
3v1s.1  TG-IVYFTDVSTLYDDRGVQQIMDTSDKTGRLIKYDPSTKETTLLLKELHVPGGAEVSADSSFVLVAEFLSHQIVKYWLE

APMAP   GLMKGGADLFVENMPGFPDNIRPSSSGGYWVGMSTIRPNPGFSMLDFLSERPWIKRMIFKLFSQETVMKFVPRYSLVLEL
3v1s.1  GPKKGTAEVLVK-IPN-PGNIKRNADGHFWVSSSEELD-----GNMHGRVDP----------------------KGIKF

APMAP   SDSGAFRRS--LHDPDGLVATYISEVHEHDGHLYLGSFRSPFLCRLSLQAV
3v1s.1  DEFGNILEVIPLPPPFAG--EHFEQIQEHDGLLYIGTLFHGSVGILVYD--
```

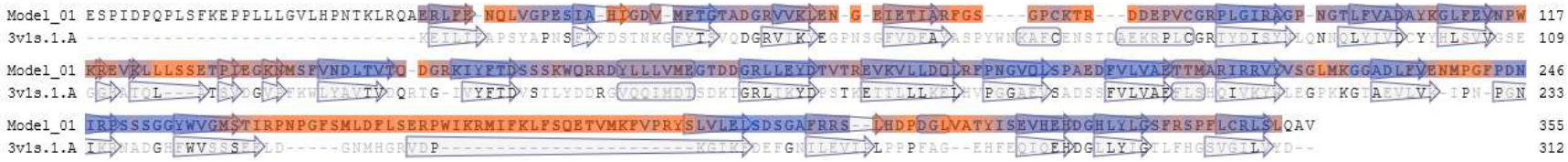

7. References

Adams, P. D., R. W. Grosse-Kunstleve, L. W. Hung, T. R. Ioerger, A. J. McCoy, N. W. Moriarty, R. J. Read, J. C. Sacchettini, N. K. Sauter, and T. C. Terwilliger. 2002. 'PHENIX: building new software for automated crystallographic structure determination', *Acta Crystallogr D Biol Crystallogr*, 58: 1948-54.

Ahmed, W., C. Wan, A. Goonetilleke, and T. Gardner. 2010. 'Evaluating sewage-associated JCV and BKV polyomaviruses for sourcing human fecal pollution in a coastal river in Southeast Queensland, Australia', *J Environ Qual*, 39: 1743-50.

Albrektsen, T., H. E. Richter, J. T. Clausen, and J. Fleckner. 2001. 'Identification of a novel integral plasma membrane protein induced during adipocyte differentiation', *Biochem J*, 359: 393-402.

Allander, T., K. Andreasson, S. Gupta, A. Bjerkner, G. Bogdanovic, M. A. Persson, T. Dalianis, T. Ramqvist, and B. Andersson. 2007. 'Identification of a third human polyomavirus', *J Virol*, 81: 4130-6.

Aly, L., S. Yousef, S. Schippling, I. Jelcic, P. Breiden, J. Matschke, R. Schulz, S. Bofill-Mas, L. Jones, V. Demina, M. Linnebank, G. Ogg, R. Girones, T. Weber, M. Sospedra, and R. Martin. 2011. 'Central role of JC virus-specific CD4+ lymphocytes in progressive multi-focal leucoencephalopathy-immune reconstitution inflammatory syndrome', *Brain*, 134: 2687-702.

Anderson, H. A., Y. Chen, and L. C. Norkin. 1998. 'MHC class I molecules are enriched in caveolae but do not enter with simian virus 40', *J Gen Virol*, 79 (Pt 6): 1469-77.

Anderson, R. G. 1998. 'The caveolae membrane system', *Annu Rev Biochem*, 67: 199-225.

Assetta, B., M. S. Maginnis, I. Gracia Ahufinger, S. A. Haley, G. V. Gee, C. D. Nelson, B. A. O'Hara, S. A. Allen Ramdial, and W. J. Atwood. 2013. '5-HT2 receptors facilitate JC polyomavirus entry', *J Virol*, 87: 13490-8.

Atwood, W. J., and L. C. Norkin. 1989. 'Class I major histocompatibility proteins as cell surface receptors for simian virus 40', *J Virol*, 63: 4474-7.

Barbanti-Brodano, G., S. Sabbioni, F. Martini, M. Negrini, A. Corallini, and M. Tognon. 2006. 'BK virus, JC virus and Simian Virus 40 infection in humans, and association with human tumors', *Adv Exp Med Biol*, 577: 319-41.

Barouch, D. H., and S. C. Harrison. 1994. 'Interactions among the major and minor coat proteins of polyomavirus', *J Virol*, 68: 3982-9.

Bellizzi, A., E. Anzivino, D. M. Rodio, S. Cioccolo, R. Scrivo, M. Morreale, S. Pontecorvo, F. Ferrari, G. Di Nardo, L. Nencioni, S. Carluccio, G. Valesini, A. Francia, S. Cucchiara, A. T. Palamara, and V. Pietropaolo. 2013. 'Human Polyomavirus JC monitoring and noncoding control region analysis in dynamic cohorts of individuals affected by immune-mediated diseases under treatment with biologics: an observational study', *Virol J*, 10: 298.

Bellizzi, A., E. Anzivino, D. M. Rodio, A. T. Palamara, L. Nencioni, and V. Pietropaolo. 2013. 'New insights on human polyomavirus JC and pathogenesis of progressive multifocal leukoencephalopathy', *Clin Dev Immunol*, 2013: 839719.

Bennett, S. M., N. M. Broekema, and M. J. Imperiale. 2012. 'BK polyomavirus: emerging pathogen', *Microbes Infect*, 14: 672-83.

Bennett, S. M., L. B. Zhao, C. Bosard, and M. J. Imperiale. 2015a. 'Role of a nuclear localization signal on the minor capsid Proteins VP2 and VP3 in BKPyV nuclear entry', *Virology*, 474: 110-16.

Bennett, S. M., L. Zhao, C. Bosard, and M. J. Imperiale. 2015b. 'Role of a nuclear localization signal on the minor capsid proteins VP2 and VP3 in BKPyV nuclear entry', *Virology*, 474: 110-6.

Berger, J. R. 2017. 'Classifying PML risk with disease modifying therapies', *Mult Scler Relat Disord*, 12: 59-63.

Bofill-Mas, S., P. Clemente-Casares, E. O. Major, B. Curfman, and R. Girones. 2003. 'Analysis of the excreted JC virus strains and their potential oral transmission', *J Neurovirol*, 9: 498-507.

Bofill-Mas, S., and R. Girones. 2001. 'Excretion and transmission of JCV in human populations', *J Neurovirol*, 7: 345-9.
———. 2003. 'Role of the environment in the transmission of JC virus', *J Neurovirol*, 9 Suppl 1: 54-8.
Bogdanoff, W. A., E. I. Perez, T. Lopez, C. F. Arias, and R. M. DuBois. 2018. 'Structural Basis for Escape of Human Astrovirus from Antibody Neutralization: Broad Implications for Rational Vaccine Design', *J Virol*, 92.
Bogner-Strauss, J. G., A. Prokesch, F. Sanchez-Cabo, D. Rieder, H. Hackl, K. Duszka, A. Krogsdam, B. Di Camillo, E. Walenta, A. Klatzer, A. Lass, M. Pinent, W. C. Wong, F. Eisenhaber, and Z. Trajanoski. 2010. 'Reconstruction of gene association network reveals a transmembrane protein required for adipogenesis and targeted by PPARgamma', *Cell Mol Life Sci*, 67: 4049-64.
Boldorini, R., S. Allegrini, U. Miglio, A. Paganotti, N. Cocca, M. Zaffaroni, F. Riboni, G. Monga, and R. Viscidi. 2011. 'Serological evidence of vertical transmission of JC and BK polyomaviruses in humans', *J Gen Virol*, 92: 1044-50.
Bollag, G., J. Tsai, J. Zhang, C. Zhang, P. Ibrahim, K. Nolop, and P. Hirth. 2012. 'Vemurafenib: the first drug approved for BRAF-mutant cancer', *Nat Rev Drug Discov*, 11: 873-86.
Bonhaus, D. W., C. Bach, A. DeSouza, F. H. Salazar, B. D. Matsuoka, P. Zuppan, H. W. Chan, and R. M. Eglen. 1995. 'The pharmacology and distribution of human 5-hydroxytryptamine2B (5-HT2B) receptor gene products: comparison with 5-HT2A and 5-HT2C receptors', *Br J Pharmacol*, 115: 622-8.
Bornholdt, Z. A., H. L. Turner, C. D. Murin, W. Li, D. Sok, C. A. Souders, A. E. Piper, A. Goff, J. D. Shamblin, S. E. Wollen, T. R. Sprague, M. L. Fusco, K. B. Pommert, L. A. Cavacini, H. L. Smith, M. Klempner, K. A. Reimann, E. Krauland, T. U. Gerngross, K. D. Wittrup, E. O. Saphire, D. R. Burton, P. J. Glass, A. B. Ward, and L. M. Walker. 2016. 'Isolation of potent neutralizing antibodies from a survivor of the 2014 Ebola virus outbreak', *Science*, 351: 1078-83.
Brady, J. N., V. D. Winston, and R. A. Consigli. 1977. 'Dissociation of polyoma virus by the chelation of calcium ions found associated with purified virions', *J Virol*, 23: 717-24.
Breau, W. C., W. J. Atwood, and L. C. Norkin. 1992. 'Class I major histocompatibility proteins are an essential component of the simian virus 40 receptor', *J Virol*, 66: 2037-45.
Breg, J., L. M. Kroon-Batenburg, G. Strecker, J. Montreuil, and J. F. Vliegenthart. 1989. 'Conformational analysis of the sialyl alpha(2----3/6)N-acetyllactosamine structural element occurring in glycoproteins, by two-dimensional NOE 1H-NMR spectroscopy in combination with energy calculations by hard-sphere exo-anomeric and molecular mechanics force-field with hydrogen-bonding potential', *Eur J Biochem*, 178: 727-39.
Brown, P., T. Tsai, and D. C. Gajdusek. 1975. 'Seroepidemiology of human papovaviruses. Discovery of virgin populations and some unusual patterns of antibody prevalence among remote peoples of the world', *Am J Epidemiol*, 102: 331-40.
Brunger, A. T. 1992. 'Free R value: a novel statistical quantity for assessing the accuracy of crystal structures', *Nature*, 355: 472-5.
Buch, M. H., A. M. Liaci, S. D. O'Hara, R. L. Garcea, U. Neu, and T. Stehle. 2015. 'Structural and Functional Analysis of Murine Polyomavirus Capsid Proteins Establish the Determinants of Ligand Recognition and Pathogenicity', *PLoS Pathog*, 11: e1005104.
Burkert, O., S. Kressner, L. Sinn, S. Giese, C. Simon, and H. Lilie. 2014. 'Biophysical characterization of polyomavirus minor capsid proteins', *Biol Chem*, 395: 871-80.
Burmeister, W. P., D. Guilligay, S. Cusack, G. Wadell, and N. Arnberg. 2004. 'Crystal structure of species D adenovirus fiber knobs and their sialic acid binding sites', *J Virol*, 78: 7727-36.
Butin-Israeli, V., O. Ben-nun-Shaul, I. Kopatz, S. A. Adam, T. Shimi, R. D. Goldman, and A. Oppenheim. 2011. 'Simian virus 40 induces lamin A/C fluctuations and nuclear envelope deformation during cell entry', *Nucleus*, 2: 320-30.
Cahan, L. D., R. Singh, and J. C. Paulson. 1983. 'Sialyloligosaccharide receptors of binding variants of polyoma virus', *Virology*, 130: 281-9.

Campanero-Rhodes, M. A., A. Smith, W. Chai, S. Sonnino, L. Mauri, R. A. Childs, Y. Zhang, H. Ewers, A. Helenius, A. Imberty, and T. Feizi. 2007. 'N-glycolyl GM1 ganglioside as a receptor for simian virus 40', *J Virol*, 81: 12846-58.

Carbone, M., G. Ascione, S. Chichiarelli, M. I. Garcia, M. Eufemi, and P. Amati. 2004. 'Chromosome-protein interactions in polyomavirus virions', *J Virol*, 78: 513-9.

Carrillo-Tripp, M., C. M. Shepherd, I. A. Borelli, S. Venkataraman, G. Lander, P. Natarajan, J. E. Johnson, C. L. Brooks, 3rd, and V. S. Reddy. 2009. 'VIPERdb2: an enhanced and web API enabled relational database for structural virology', *Nucleic Acids Res*, 37: D436-42.

Carson, K. R., D. Focosi, E. O. Major, M. Petrini, E. A. Richey, D. P. West, and C. L. Bennett. 2009. 'Monoclonal antibody-associated progressive multifocal leucoencephalopathy in patients treated with rituximab, natalizumab, and efalizumab: a Review from the Research on Adverse Drug Events and Reports (RADAR) Project', *Lancet Oncol*, 10: 816-24.

Caruso, M., L. Belloni, O. Sthandier, P. Amati, and M. I. Garcia. 2003. 'Alpha4beta1 integrin acts as a cell receptor for murine polyomavirus at the postattachment level', *J Virol*, 77: 3913-21.

Chang, H., M. Wang, R. T. Tsai, H. S. Lin, J. S. Huan, W. C. Wang, and D. Chang. 2002. 'High incidence of JC viruria in JC-seropositive older individuals', *J Neurovirol*, 8: 447-51.

Chapagain, M. L., and V. R. Nerurkar. 2010. 'Human polyomavirus JC (JCV) infection of human B lymphocytes: a possible mechanism for JCV transmigration across the blood-brain barrier', *J Infect Dis*, 202: 184-91.

Chen, C. K., N. L. Chan, and A. H. Wang. 2011. 'The many blades of the beta-propeller proteins: conserved but versatile', *Trends Biochem Sci*, 36: 553-61.

Chen, H., Z. Yang, C. Ding, L. Chu, Y. Zhang, K. Terry, H. Liu, Q. Shen, and J. Zhou. 2013. 'Fragment-based drug design and identification of HJC0123, a novel orally bioavailable STAT3 inhibitor for cancer therapy', *Eur J Med Chem*, 62: 498-507.

Chen, X. S., T. Stehle, and S. C. Harrison. 1998. 'Interaction of polyomavirus internal protein VP2 with the major capsid protein VP1 and implications for participation of VP2 in viral entry', *EMBO J*, 17: 3233-40.

Chilingaryan, Z., Z. Yin, and A. J. Oakley. 2012. 'Fragment-based screening by protein crystallography: successes and pitfalls', *Int J Mol Sci*, 13: 12857-79.

Chou, H. H., H. Takematsu, S. Diaz, J. Iber, E. Nickerson, K. L. Wright, E. A. Muchmore, D. L. Nelson, S. T. Warren, and A. Varki. 1998. 'A mutation in human CMP-sialic acid hydroxylase occurred after the Homo-Pan divergence', *Proc Natl Acad Sci U S A*, 95: 11751-6.

Cole, C. N., T. Landers, S. P. Goff, S. Manteuil-Brutlag, and P. Berg. 1977. 'Physical and genetic characterization of deletion mutants of simian virus 40 constructed in vitro', *J Virol*, 24: 277-94.

Collaborative Computational Project, Number. 1994. 'The CCP4 suite: programs for protein crystallography', *Acta Crystallogr D Biol Crystallogr*, 50: 760-3.

Corti, D., S. Bianchi, F. Vanzetta, A. Minola, L. Perez, G. Agatic, B. Guarino, C. Silacci, J. Marcandalli, B. J. Marsland, A. Piralla, E. Percivalle, F. Sallusto, F. Baldanti, and A. Lanzavecchia. 2013. 'Cross-neutralization of four paramyxoviruses by a human monoclonal antibody', *Nature*, 501: 439-43.

Corti, D., and A. Lanzavecchia. 2013. 'Broadly neutralizing antiviral antibodies', *Annu Rev Immunol*, 31: 705-42.

Corti, D., J. Misasi, S. Mulangu, D. A. Stanley, M. Kanekiyo, S. Wollen, A. Ploquin, N. A. Doria-Rose, R. P. Staupe, M. Bailey, W. Shi, M. Choe, H. Marcus, E. A. Thompson, A. Cagigi, C. Silacci, B. Fernandez-Rodriguez, L. Perez, F. Sallusto, F. Vanzetta, G. Agatic, E. Cameroni, N. Kisalu, I. Gordon, J. E. Ledgerwood, J. R. Mascola, B. S. Graham, J. J. Muyembe-Tamfun, J. C. Trefry, A. Lanzavecchia, and N. J. Sullivan. 2016. 'Protective monotherapy against lethal Ebola virus infection by a potently neutralizing antibody', *Science*, 351: 1339-42.

Dalianis, T., and H. H. Hirsch. 2013. 'Human polyomaviruses in disease and cancer', *Virology*, 437: 63-72.

Dalvit, C., E. Ardini, M. Flocco, G. P. Fogliatto, N. Mongelli, and M. Veronesi. 2003. 'A general NMR method for rapid, efficient, and reliable biochemical screening', *J Am Chem Soc*, 125: 14620-5.

Dalvit, C., P. E. Fagerness, D. T. Hadden, R. W. Sarver, and B. J. Stockman. 2003. 'Fluorine-NMR experiments for high-throughput screening: theoretical aspects, practical considerations, and range of applicability', *J Am Chem Soc*, 125: 7696-703.

Dalyot-Herman, N., O. Ben-nun-Shaul, A. Gordon-Shaag, and A. Oppenheim. 1996. 'The simian virus 40 packaging signal ses is composed of redundant DNA elements which are partly interchangeable', *J Mol Biol*, 259: 69-80.

Daniels, R., N. M. Rusan, P. Wadsworth, and D. N. Hebert. 2006. 'SV40 VP2 and VP3 insertion into ER membranes is controlled by the capsid protein VP1: implications for DNA translocation out of the ER', *Mol Cell*, 24: 955-66.

Daniels, R., N. M. Rusan, A. K. Wilbuer, L. C. Norkin, P. Wadsworth, and D. N. Hebert. 2006. 'Simian virus 40 late proteins possess lytic properties that render them capable of permeabilizing cellular membranes', *J Virol*, 80: 6575-87.

De Clercq, E. 2002. 'Strategies in the design of antiviral drugs', *Nat Rev Drug Discov*, 1: 13-25.

De Gascun, C. F., and M. J. Carr. 2013. 'Human polyomavirus reactivation: disease pathogenesis and treatment approaches', *Clin Dev Immunol*, 2013: 373579.

Delbue, S., E. Branchetti, S. Bertolacci, E. Tavazzi, E. Marchioni, R. Maserati, G. Minnucci, S. Tremolada, G. Vago, and P. Ferrante. 2009. 'JC virus VP1 loop-specific polymorphisms are associated with favorable prognosis for progressive multifocal leukoencephalopathy', *J Neurovirol*, 15: 51-6.

Deloukas, P., L. H. Matthews, J. Ashurst, J. Burton, J. G. Gilbert, M. Jones, G. Stavrides, J. P. Almeida, A. K. Babbage, C. L. Bagguley, J. Bailey, K. F. Barlow, K. N. Bates, L. M. Beard, D. M. Beare, O. P. Beasley, C. P. Bird, S. E. Blakey, A. M. Bridgeman, A. J. Brown, D. Buck, W. Burrill, A. P. Butler, C. Carder, N. P. Carter, J. C. Chapman, M. Clamp, G. Clark, L. N. Clark, S. Y. Clark, C. M. Clee, S. Clegg, V. E. Cobley, R. E. Collier, R. Connor, N. R. Corby, A. Coulson, G. J. Coville, R. Deadman, P. Dhami, M. Dunn, A. G. Ellington, J. A. Frankland, A. Fraser, L. French, P. Garner, D. V. Grafham, C. Griffiths, M. N. Griffiths, R. Gwilliam, R. E. Hall, S. Hammond, J. L. Harley, P. D. Heath, S. Ho, J. L. Holden, P. J. Howden, E. Huckle, A. R. Hunt, S. E. Hunt, K. Jekosch, C. M. Johnson, D. Johnson, M. P. Kay, A. M. Kimberley, A. King, A. Knights, G. K. Laird, S. Lawlor, M. H. Lehvaslaiho, M. Leversha, C. Lloyd, D. M. Lloyd, J. D. Lovell, V. L. Marsh, S. L. Martin, L. J. McConnachie, K. McLay, A. A. McMurray, S. Milne, D. Mistry, M. J. Moore, J. C. Mullikin, T. Nickerson, K. Oliver, A. Parker, R. Patel, T. A. Pearce, A. I. Peck, B. J. Phillimore, S. R. Prathalingam, R. W. Plumb, H. Ramsay, C. M. Rice, M. T. Ross, C. E. Scott, H. K. Sehra, R. Shownkeen, S. Sims, C. D. Skuce, M. L. Smith, C. Soderlund, C. A. Steward, J. E. Sulston, M. Swann, N. Sycamore, R. Taylor, L. Tee, D. W. Thomas, A. Thorpe, A. Tracey, A. C. Tromans, M. Vaudin, M. Wall, J. M. Wallis, S. L. Whitehead, P. Whittaker, D. L. Willey, L. Williams, S. A. Williams, L. Wilming, P. W. Wray, T. Hubbard, R. M. Durbin, D. R. Bentley, S. Beck, and J. Rogers. 2001. 'The DNA sequence and comparative analysis of human chromosome 20', *Nature*, 414: 865-71.

DeWire, S. M., S. Ahn, R. J. Lefkowitz, and S. K. Shenoy. 2007. 'Beta-arrestins and cell signaling', *Annu Rev Physiol*, 69: 483-510.

Diederichs, K., and P. A. Karplus. 1997. 'Improved R-factors for diffraction data analysis in macromolecular crystallography', *Nat Struct Biol*, 4: 269-75.

Dietrich, M. H., C. Harprecht, and T. Stehle. 2017. 'The bulky and the sweet: How neutralizing antibodies and glycan receptors compete for virus binding', *Protein Sci*, 26: 2342-54.

Diotti, R. A., A. Nakanishi, N. Clementi, N. Mancini, E. Criscuolo, L. Solforosi, and M. Clementi. 2013. 'JC polyomavirus (JCV) and monoclonal antibodies: friends or potential foes?', *Clin Dev Immunol*, 2013: 967581.

Drayman, N., Y. Glick, O. Ben-nun-shaul, H. Zer, A. Zlotnick, D. Gerber, O. Schueler-Furman, and A. Oppenheim. 2013. 'Pathogens use structural mimicry of native host ligands as a mechanism for host receptor engagement', *Cell Host Microbe*, 14: 63-73.

Du Pasquier, R. A., S. Corey, D. H. Margolin, K. Williams, L. A. Pfister, U. De Girolami, J. J. Mac Key, C. Wuthrich, J. T. Joseph, and I. J. Koralnik. 2003. 'Productive infection of cerebellar granule cell neurons by JC virus in an HIV+ individual', *Neurology*, 61: 775-82.

Dubois, V., H. Dutronc, M. E. Lafon, V. Poinsot, J. L. Pellegrin, J. M. Ragnaud, A. M. Ferrer, and H. J. Fleury. 1997. 'Latency and reactivation of JC virus in peripheral blood of human immunodeficiency virus type 1-infected patients', *J Clin Microbiol*, 35: 2288-92.

Dugan, A. S., M. L. Gasparovic, and W. J. Atwood. 2008. 'Direct correlation between sialic acid binding and infection of cells by two human polyomaviruses (JC virus and BK virus)', *J Virol*, 82: 2560-4.

Dupzyk, A., and B. Tsai. 2016. 'How Polyomaviruses Exploit the ERAD Machinery to Cause Infection', *Viruses*, 8.

———. 2018. 'Bag2 Is a Component of a Cytosolic Extraction Machinery That Promotes Membrane Penetration of a Nonenveloped Virus', *J Virol*, 92.

Dutton, A. C., A. N. Massoura, T. J. Dover, N. A. Andrews, and N. M. Barnes. 2008. 'Identification and functional significance of N-glycosylation of the 5-ht5A receptor', *Neurochem Int*, 52: 419-25.

Dwyer, J. J., K. L. Wilson, D. K. Davison, S. A. Freel, J. E. Seedorff, S. A. Wring, N. A. Tvermoes, T. J. Matthews, M. L. Greenberg, and M. K. Delmedico. 2007. 'Design of helical, oligomeric HIV-1 fusion inhibitor peptides with potent activity against enfuvirtide-resistant virus', *Proc Natl Acad Sci U S A*, 104: 12772-7.

Eash, S., and W. J. Atwood. 2005. 'Involvement of cytoskeletal components in BK virus infectious entry', *J Virol*, 79: 11734-41.

Eash, S., W. Querbes, and W. J. Atwood. 2004. 'Infection of vero cells by BK virus is dependent on caveolae', *J Virol*, 78: 11583-90.

Eash, S., R. Tavares, E. G. Stopa, S. H. Robbins, L. Brossay, and W. J. Atwood. 2004. 'Differential distribution of the JC virus receptor-type sialic acid in normal human tissues', *Am J Pathol*, 164: 419-28.

Edfeldt, F. N., R. H. Folmer, and A. L. Breeze. 2011. 'Fragment screening to predict druggability (ligandability) and lead discovery success', *Drug Discov Today*, 16: 284-7.

Egli, A., L. Infanti, A. Dumoulin, A. Buser, J. Samaridis, C. Stebler, R. Gosert, and H. H. Hirsch. 2009. 'Prevalence of polyomavirus BK and JC infection and replication in 400 healthy blood donors', *J Infect Dis*, 199: 837-46.

Ehlers, B., and U. Moens. 2014. 'Genome analysis of non-human primate polyomaviruses', *Infect Genet Evol*, 26: 283-94.

Elphick, G. F., W. Querbes, J. A. Jordan, G. V. Gee, S. Eash, K. Manley, A. Dugan, M. Stanifer, A. Bhatnagar, W. K. Kroeze, B. L. Roth, and W. J. Atwood. 2004. 'The human polyomavirus, JCV, uses serotonin receptors to infect cells', *Science*, 306: 1380-3.

Engel, S., T. Heger, R. Mancini, F. Herzog, J. Kartenbeck, A. Hayer, and A. Helenius. 2011. 'Role of endosomes in simian virus 40 entry and infection', *J Virol*, 85: 4198-211.

Erickson, K. D., C. Bouchet-Marquis, K. Heiser, E. Szomolanyi-Tsuda, R. Mishra, B. Lamothe, A. Hoenger, and R. L. Garcea. 2012. 'Virion assembly factories in the nucleus of polyomavirus-infected cells', *PLoS Pathog*, 8: e1002630.

Ewers, H., and A. Helenius. 2011. 'Lipid-mediated endocytosis', *Cold Spring Harb Perspect Biol*, 3: a004721.

Ewers, H., W. Romer, A. E. Smith, K. Bacia, S. Dmitrieff, W. Chai, R. Mancini, J. Kartenbeck, V. Chambon, L. Berland, A. Oppenheim, G. Schwarzmann, T. Feizi, P. Schwille, P. Sens, A. Helenius, and L. Johannes. 2010. 'GM1 structure determines SV40-induced membrane invagination and infection', *Nat Cell Biol*, 12: 11-8; sup pp 1-12.

Feng, H., M. Shuda, Y. Chang, and P. S. Moore. 2008. 'Clonal integration of a polyomavirus in human Merkel cell carcinoma', *Science*, 319: 1096-100.

Ferenczy, M. W., L. J. Marshall, C. D. Nelson, W. J. Atwood, A. Nath, K. Khalili, and E. O. Major. 2012. 'Molecular biology, epidemiology, and pathogenesis of progressive multifocal leukoencephalopathy, the JC virus-induced demyelinating disease of the human brain', *Clin Microbiol Rev*, 25: 471-506.

Ferrante, P., R. Caldarelli-Stefano, E. Omodeo-Zorini, L. Vago, R. Boldorini, and G. Costanzi. 1995. 'PCR detection of JC virus DNA in brain tissue from patients with and without progressive multifocal leukoencephalopathy', *J Med Virol*, 47: 219-25.

Frasca, G. M., S. Sandrini, L. Cosmai, C. Porta, W. Asch, M. Santoni, C. Salviani, A. D'Errico, D. Malvi, E. Balestra, and M. Gallieni. 2015. 'Renal cancer in kidney transplanted patients', *J Nephrol*, 28: 659-68.

Frisque, R. J. 1983. 'Nucleotide sequence of the region encompassing the JC virus origin of DNA replication', *J Virol*, 46: 170-6.

Gardner, S. D., A. M. Field, D. V. Coleman, and B. Hulme. 1971. 'New human papovavirus (B.K.) isolated from urine after renal transplantation', *Lancet*, 1: 1253-7.

Gasparovic, M. L., G. V. Gee, and W. J. Atwood. 2006. 'JC virus minor capsid proteins Vp2 and Vp3 are essential for virus propagation', *J Virol*, 80: 10858-61.

Gaynor, A. M., M. D. Nissen, D. M. Whiley, I. M. Mackay, S. B. Lambert, G. Wu, D. C. Brennan, G. A. Storch, T. P. Sloots, and D. Wang. 2007. 'Identification of a novel polyomavirus from patients with acute respiratory tract infections', *PLoS Pathog*, 3: e64.

Gee, G. V., A. S. Dugan, N. Tsomaia, D. F. Mierke, and W. J. Atwood. 2006. 'The role of sialic acid in human polyomavirus infections', *Glycoconj J*, 23: 19-26.

Geiger, R., D. Andritschke, S. Friebe, F. Herzog, S. Luisoni, T. Heger, and A. Helenius. 2011. 'BAP31 and BiP are essential for dislocation of SV40 from the endoplasmic reticulum to the cytosol', *Nat Cell Biol*, 13: 1305-14.

Geoghegan, E. M., D. V. Pastrana, R. M. Schowalter, U. Ray, W. Gao, M. Ho, G. T. Pauly, D. M. Sigano, C. Kaynor, E. Cahir-McFarland, B. Combaluzier, J. Grimm, and C. B. Buck. 2017. 'Infectious Entry and Neutralization of Pathogenic JC Polyomaviruses', *Cell Rep*, 21: 1169-79.

Gharakhanian, E., L. Munoz, and L. Mayorca. 2003. 'The simian virus 40 minor structural protein Vp3, but not Vp2, is essential for infectious virion formation', *J Gen Virol*, 84: 2111-6.

Gilbert, J., and T. Benjamin. 2004. 'Uptake pathway of polyomavirus via ganglioside GD1a', *J Virol*, 78: 12259-67.

Gilbert, J. M., and T. L. Benjamin. 2000. 'Early steps of polyomavirus entry into cells', *J Virol*, 74: 8582-8.

Gilbert, J. M., I. G. Goldberg, and T. L. Benjamin. 2003. 'Cell penetration and trafficking of polyomavirus', *J Virol*, 77: 2615-22.

Gilbert, J., W. Ou, J. Silver, and T. Benjamin. 2006. 'Downregulation of protein disulfide isomerase inhibits infection by the mouse polyomavirus', *J Virol*, 80: 10868-70.

Gillock, E. T., S. Rottinghaus, D. Chang, X. Cai, S. A. Smiley, K. An, and R. A. Consigli. 1997. 'Polyomavirus major capsid protein VP1 is capable of packaging cellular DNA when expressed in the baculovirus system', *J Virol*, 71: 2857-65.

Goodwin, E. C., A. Lipovsky, T. Inoue, T. G. Magaldi, A. P. Edwards, K. E. Van Goor, A. W. Paton, J. C. Paton, W. J. Atwood, B. Tsai, and D. DiMaio. 2011. 'BiP and multiple DNAJ molecular chaperones in the endoplasmic reticulum are required for efficient simian virus 40 infection', *MBio*, 2: e00101-11.

Gorelik, L., M. Lerner, S. Bixler, M. Crossman, B. Schlain, K. Simon, A. Pace, A. Cheung, L. L. Chen, M. Berman, F. Zein, E. Wilson, T. Yednock, A. Sandrock, S. E. Goelz, and M. Subramanyam. 2010. 'Anti-JC virus antibodies: implications for PML risk stratification', *Ann Neurol*, 68: 295-303.

Gorelik, L., C. Reid, M. Testa, M. Brickelmaier, S. Bossolasco, A. Pazzi, A. Bestetti, P. Carmillo, E. Wilson, M. McAuliffe, C. Tonkin, J. P. Carulli, A. Lugovskoy, A. Lazzarin, S. Sunyaev, K. Simon, and P. Cinque. 2011. 'Progressive multifocal leukoencephalopathy (PML) development is associated with mutations in JC virus capsid protein VP1 that change its receptor specificity', *J Infect Dis*, 204: 103-14.

Gray, J. A., and B. L. Roth. 2001. 'Paradoxical trafficking and regulation of 5-HT(2A) receptors by agonists and antagonists', *Brain Res Bull*, 56: 441-51.

Greenfield, N. J. 2006. 'Using circular dichroism spectra to estimate protein secondary structure', *Nat Protoc*, 1: 2876-90.

Griffith, J. P., D. L. Griffith, I. Rayment, W. T. Murakami, and D. L. Caspar. 1992. 'Inside polyomavirus at 25-A resolution', *Nature*, 355: 652-4.
Gross, L. 1953. 'Neck tumors, or leukemia, developing in adult C3H mice following inoculation, in early infancy, with filtered (Berkefeld N), or centrifugated (144,000 X g), Ak-leukemic extracts', *Cancer*, 6: 948-58.
Gupta, G., S. Kuppachi, R. S. Kalil, C. B. Buck, C. F. Lynch, and E. A. Engels. 2018. 'Treatment for presumed BK polyomavirus nephropathy and risk of urinary tract cancers among kidney transplant recipients in the United States', *Am J Transplant*, 18: 245-52.
Hajduk, P. J., and J. Greer. 2007. 'A decade of fragment-based drug design: strategic advances and lessons learned', *Nat Rev Drug Discov*, 6: 211-9.
Hajduk, P. J., J. R. Huth, and S. W. Fesik. 2005. 'Druggability indices for protein targets derived from NMR-based screening data', *J Med Chem*, 48: 2518-25.
Hamilton, R. S., M. Gravell, and E. O. Major. 2000. 'Comparison of antibody titers determined by hemagglutination inhibition and enzyme immunoassay for JC virus and BK virus', *J Clin Microbiol*, 38: 105-9.
Hamza, I. A., L. Jurzik, A. Stang, K. Sure, K. Uberla, and M. Wilhelm. 2009. 'Detection of human viruses in rivers of a densly-populated area in Germany using a virus adsorption elution method optimized for PCR analyses', *Water Res*, 43: 2657-68.
Hariharan, S., E. P. Cohen, B. Vasudev, R. Orentas, R. P. Viscidi, J. Kakela, and B. DuChateau. 2005. 'BK virus-specific antibodies and BKV DNA in renal transplant recipients with BKV nephritis', *Am J Transplant*, 5: 2719-24.
Hartshorn, M. J., C. W. Murray, A. Cleasby, M. Frederickson, I. J. Tickle, and H. Jhoti. 2005. 'Fragment-based lead discovery using X-ray crystallography', *J Med Chem*, 48: 403-13.
Hayer, A., M. Stoeber, D. Ritz, S. Engel, H. H. Meyer, and A. Helenius. 2010. 'Caveolin-1 is ubiquitinated and targeted to intralumenal vesicles in endolysosomes for degradation', *J Cell Biol*, 191: 615-29.
Hirsch, H. H., D. C. Brennan, C. B. Drachenberg, F. Ginevri, J. Gordon, A. P. Limaye, M. J. Mihatsch, V. Nickeleit, E. Ramos, P. Randhawa, R. Shapiro, J. Steiger, M. Suthanthiran, and J. Trofe. 2005. 'Polyomavirus-associated nephropathy in renal transplantation: interdisciplinary analyses and recommendations', *Transplantation*, 79: 1277-86.
Holthofer, H., J. Reivinen, and A. Miettinen. 1994. 'Nephron segment and cell-type specific expression of gangliosides in the developing and adult kidney', *Kidney Int*, 45: 123-30.
Hortobagyi, G. N., S. M. Stemmer, H. A. Burris, Y. S. Yap, G. S. Sonke, S. Paluch-Shimon, M. Campone, K. L. Blackwell, F. Andre, E. P. Winer, W. Janni, S. Verma, P. Conte, C. L. Arteaga, D. A. Cameron, K. Petrakova, L. L. Hart, C. Villanueva, A. Chan, E. Jakobsen, A. Nusch, O. Burdaeva, E. M. Grischke, E. Alba, E. Wist, N. Marschner, A. M. Favret, D. Yardley, T. Bachelot, L. M. Tseng, S. Blau, F. Xuan, F. Souami, M. Miller, C. Germa, S. Hirawat, and J. O'Shaughnessy. 2016. 'Ribociclib as First-Line Therapy for HR-Positive, Advanced Breast Cancer', *N Engl J Med*, 375: 1738-48.
Hurdiss, D. L., M. Frank, J. S. Snowden, A. Macdonald, and N. A. Ranson. 2018. 'The Structure of an Infectious Human Polyomavirus and Its Interactions with Cellular Receptors', *Structure*, 26: 839-47 e3.
Ilhan, A., W. Gartner, A. Nabokikh, T. Daneva, O. Majdic, G. Cohen, G. A. Bohmig, W. Base, W. H. Horl, and L. Wagner. 2008. 'Localization and characterization of the novel protein encoded by C20orf3', *Biochem J*, 414: 485-95.
Inoue, T., A. Dosey, J. F. Herbstman, M. S. Ravindran, G. Skiniotis, and B. Tsai. 2015. 'ERdj5 Reductase Cooperates with Protein Disulfide Isomerase To Promote Simian Virus 40 Endoplasmic Reticulum Membrane Translocation', *J Virol*, 89: 8897-908.
Irie, A., and A. Suzuki. 1998. 'CMP-N-Acetylneuraminic acid hydroxylase is exclusively inactive in humans', *Biochem Biophys Res Commun*, 248: 330-3.
Ishizu, K. I., H. Watanabe, S. I. Han, S. N. Kanesashi, M. Hoque, H. Yajima, K. Kataoka, and H. Handa. 2001. 'Roles of disulfide linkage and calcium ion-mediated interactions in assembly and

disassembly of virus-like particles composed of simian virus 40 VP1 capsid protein', *J Virol*, 75: 61-72.
Ishov, A. M., and G. G. Maul. 1996. 'The periphery of nuclear domain 10 (ND10) as site of DNA virus deposition', *J Cell Biol*, 134: 815-26.
Jao, C. C., M. K. Weidman, A. R. Perez, and E. Gharakhanian. 1999. 'Cys9, Cys104 and Cys207 of simian virus 40 Vp1 are essential for inter-pentamer disulfide-linkage and stabilization in cell-free lysates', *J Gen Virol*, 80 (Pt 9): 2481-9.
Jelcic, I., B. Combaluzier, I. Jelcic, W. Faigle, L. Senn, B. J. Reinhart, L. Stroh, R. M. Nitsch, T. Stehle, M. Sospedra, J. Grimm, and R. Martin. 2015. 'Broadly neutralizing human monoclonal JC polyomavirus VP1-specific antibodies as candidate therapeutics for progressive multifocal leukoencephalopathy', *Sci Transl Med*, 7: 306ra150.
Jelcic, I., B. Combaluzier, I. Jelcic, M. Sospedra, J. Grimm, and R. Martin. 2017. 'Prevention and therapy of JC polyomavirus-mediated progressive multifocal leukoencephalopathy - a realistic possibility?', *Swiss Med Wkly*, 147: w14520.
Jhoti, H., A. Cleasby, M. Verdonk, and G. Williams. 2007. 'Fragment-based screening using X-ray crystallography and NMR spectroscopy', *Curr Opin Chem Biol*, 11: 485-93.
Jiang, M., J. R. Abend, B. Tsai, and M. J. Imperiale. 2009. 'Early events during BK virus entry and disassembly', *J Virol*, 83: 1350-8.
Johannes, L., and V. Popoff. 2008. 'Tracing the retrograde route in protein trafficking', *Cell*, 135: 1175-87.
Johannes, L., and C. Wunder. 2011. 'Retrograde transport: two (or more) roads diverged in an endosomal tree?', *Traffic*, 12: 956-62.
Jordan, J. B., L. Poppe, X. Xia, A. C. Cheng, Y. Sun, K. Michelsen, H. Eastwood, P. D. Schnier, T. Nixey, and W. Zhong. 2012. 'Fragment based drug discovery: practical implementation based on (1)(9)F NMR spectroscopy', *J Med Chem*, 55: 678-87.
Kabsch, W. 2010. 'Integration, scaling, space-group assignment and post-refinement', *Acta Crystallogr D Biol Crystallogr*, 66: 133-44.
Karplus, P. A., and K. Diederichs. 2012. 'Linking crystallographic model and data quality', *Science*, 336: 1030-3.
Kawano, M. A., T. Inoue, H. Tsukamoto, T. Takaya, T. Enomoto, R. U. Takahashi, N. Yokoyama, N. Yamamoto, A. Nakanishi, T. Imai, T. Wada, K. Kataoka, and H. Handa. 2006. 'The VP2/VP3 minor capsid protein of simian virus 40 promotes the in vitro assembly of the major capsid protein VP1 into particles', *J Biol Chem*, 281: 10164-73.
Kawano, M. A., L. Xing, H. Tsukamoto, T. Inoue, H. Handa, and R. H. Cheng. 2009. 'Calcium bridge triggers capsid disassembly in the cell entry process of simian virus 40', *J Biol Chem*, 284: 34703-12.
Kean, J. M., S. Rao, M. Wang, and R. L. Garcea. 2009. 'Seroepidemiology of human polyomaviruses', *PLoS Pathog*, 5: e1000363.
Khan, Z. M., Y. Liu, U. Neu, M. Gilbert, B. Ehlers, T. Feizi, and T. Stehle. 2014. 'Crystallographic and glycan microarray analysis of human polyomavirus 9 VP1 identifies N-glycolyl neuraminic acid as a receptor candidate', *J Virol*, 88: 6100-11.
Khanna, N., L. Elzi, N. J. Mueller, C. Garzoni, M. Cavassini, C. A. Fux, P. Vernazza, E. Bernasconi, M. Battegay, H. H. Hirsch, and H. I. V. Cohort Study Swiss. 2009. 'Incidence and outcome of progressive multifocal leukoencephalopathy over 20 years of the Swiss HIV Cohort Study', *Clin Infect Dis*, 48: 1459-66.
Khow, O., and S. Suntrarachun. 2012. 'Strategies for production of active eukaryotic proteins in bacterial expression system', *Asian Pac J Trop Biomed*, 2: 159-62.
Knowles, W. A. 2006. 'Discovery and epidemiology of the human polyomaviruses BK virus (BKV) and JC virus (JCV)', *Adv Exp Med Biol*, 577: 19-45.
Knowles, W. A., P. Pipkin, N. Andrews, A. Vyse, P. Minor, D. W. Brown, and E. Miller. 2003. 'Population-based study of antibody to the human polyomaviruses BKV and JCV and the simian polyomavirus SV40', *J Med Virol*, 71: 115-23.

Komagome, R., H. Sawa, T. Suzuki, Y. Suzuki, S. Tanaka, W. J. Atwood, and K. Nagashima. 2002. 'Oligosaccharides as receptors for JC virus', *J Virol*, 76: 12992-3000.
Kondo, Y., M. S. Windrem, L. Zou, D. Chandler-Militello, S. J. Schanz, R. M. Auvergne, S. J. Betstadt, A. R. Harrington, M. Johnson, A. Kazarov, L. Gorelik, and S. A. Goldman. 2014. 'Human glial chimeric mice reveal astrocytic dependence of JC virus infection', *J Clin Invest*, 124: 5323-36.
Koralnik, I. J., C. Wuthrich, X. Dang, M. Rottnek, A. Gurtman, D. Simpson, and S. Morgello. 2005. 'JC virus granule cell neuronopathy: A novel clinical syndrome distinct from progressive multifocal leukoencephalopathy', *Ann Neurol*, 57: 576-80.
Kosukegawa, A., F. Arisaka, M. Takayama, H. Yajima, A. Kaidow, and H. Handa. 1996. 'Purification and characterization of virus-like particles and pentamers produced by the expression of SV40 capsid proteins in insect cells', *Biochim Biophys Acta*, 1290: 37-45.
Krauzewicz, N., C. H. Streuli, N. Stuart-Smith, M. D. Jones, S. Wallace, and B. E. Griffin. 1990. 'Myristylated polyomavirus VP2: role in the life cycle of the virus', *J Virol*, 64: 4414-20.
Krebs, C. J., M. T. McAvoy, and G. Kumar. 1995. 'The JC virus minimal core promoter is glial cell specific in vivo', *J Virol*, 69: 2434-42.
Krissinel, E., and K. Henrick. 2007. 'Inference of macromolecular assemblies from crystalline state', *J Mol Biol*, 372: 774-97.
Lamarche, C., J. Orio, S. Collette, L. Senecal, M. J. Hebert, E. Renoult, L. A. Tibbles, and J. S. Delisle. 2016. 'BK Polyomavirus and the Transplanted Kidney: Immunopathology and Therapeutic Approaches', *Transplantation*, 100: 2276-87.
Ledeen, R. W., and G. Wu. 2008. 'Nuclear sphingolipids: metabolism and signaling', *J Lipid Res*, 49: 1176-86.
Liddington, R. C., Y. Yan, J. Moulai, R. Sahli, T. L. Benjamin, and S. C. Harrison. 1991. 'Structure of simian virus 40 at 3.8-A resolution', *Nature*, 354: 278-84.
Lilley, B. N., J. M. Gilbert, H. L. Ploegh, and T. L. Benjamin. 2006. 'Murine polyomavirus requires the endoplasmic reticulum protein Derlin-2 to initiate infection', *J Virol*, 80: 8739-44.
Lindner, J. M., V. Cornacchione, A. Sathe, C. Be, H. Srinivas, E. Riquet, X. C. Leber, A. Hein, M. B. Wrobel, M. Scharenberg, T. Pietzonka, C. Wiesmann, J. Abend, and E. Traggiai. 2019. 'Human Memory B Cells Harbor Diverse Cross-Neutralizing Antibodies against BK and JC Polyomaviruses', *Immunity*.
Lipinski, C. A. 2004. 'Lead- and drug-like compounds: the rule-of-five revolution', *Drug Discov Today Technol*, 1: 337-41.
Lipinski, C. A., F. Lombardo, B. W. Dominy, and P. J. Feeney. 2001. 'Experimental and computational approaches to estimate solubility and permeability in drug discovery and development settings', *Adv Drug Deliv Rev*, 46: 3-26.
Liu, C. K., A. P. Hope, and W. J. Atwood. 1998. 'The human polyomavirus, JCV, does not share receptor specificity with SV40 on human glial cells', *J Neurovirol*, 4: 49-58.
Liu, C. K., G. Wei, and W. J. Atwood. 1998. 'Infection of glial cells by the human polyomavirus JC is mediated by an N-linked glycoprotein containing terminal alpha(2-6)-linked sialic acids', *J Virol*, 72: 4643-9.
Lloyd, K. O., and K. Furukawa. 1998. 'Biosynthesis and functions of gangliosides: recent advances', *Glycoconj J*, 15: 627-36.
Louis-Jeune, C., M. A. Andrade-Navarro, and C. Perez-Iratxeta. 2012. 'Prediction of protein secondary structure from circular dichroism using theoretically derived spectra', *Proteins*, 80: 374-81.
Low, J. A., B. Magnuson, B. Tsai, and M. J. Imperiale. 2006. 'Identification of gangliosides GD1b and GT1b as receptors for BK virus', *J Virol*, 80: 1361-6.
Ma, X., J. Koepke, G. Fritzsch, R. Diem, T. M. Kutchan, H. Michel, and J. Stockigt. 2004. 'Crystallization and preliminary X-ray crystallographic analysis of strictosidine synthase from Rauvolfia: the first member of a novel enzyme family', *Biochim Biophys Acta*, 1702: 121-4.
Ma, X., S. Panjikar, J. Koepke, E. Loris, and J. Stockigt. 2006. 'The structure of Rauvolfia serpentina strictosidine synthase is a novel six-bladed beta-propeller fold in plant proteins', *Plant Cell*, 18: 907-20.

Ma, Y., J. Gao, J. Yin, L. Gu, X. Liu, S. Chen, Q. Huang, H. Lu, Y. Yang, H. Zhou, Y. Wang, and Y. Peng. 2016. 'Identification of a Novel Function of Adipocyte Plasma Membrane-Associated Protein (APMAP) in Gestational Diabetes Mellitus by Proteomic Analysis of Omental Adipose Tissue', *J Proteome Res*, 15: 628-37.

Maginnis, M. S. 2018. 'Virus-Receptor Interactions: The Key to Cellular Invasion', *J Mol Biol*, 430: 2590-611.

Maginnis, M. S., S. A. Haley, G. V. Gee, and W. J. Atwood. 2010. 'Role of N-linked glycosylation of the 5-HT2A receptor in JC virus infection', *J Virol*, 84: 9677-84.

Maginnis, M. S., C. D. Nelson, and W. J. Atwood. 2015. 'JC polyomavirus attachment, entry, and trafficking: unlocking the keys to a fatal infection', *J Neurovirol*, 21: 601-13.

Maginnis, M. S., L. J. Stroh, G. V. Gee, B. A. O'Hara, A. Derdowski, T. Stehle, and W. J. Atwood. 2013. 'Progressive multifocal leukoencephalopathy-associated mutations in the JC polyomavirus capsid disrupt lactoseries tetrasaccharide c binding', *MBio*, 4: e00247-13.

Magnuson, B., E. K. Rainey, T. Benjamin, M. Baryshev, S. Mkrtchian, and B. Tsai. 2005. 'ERp29 triggers a conformational change in polyomavirus to stimulate membrane binding', *Mol Cell*, 20: 289-300.

Major, E. O., K. Amemiya, G. Elder, and S. A. Houff. 1990. 'Glial cells of the human developing brain and B cells of the immune system share a common DNA binding factor for recognition of the regulatory sequences of the human polyomavirus, JCV', *J Neurosci Res*, 27: 461-71.

Major, E. O., K. Amemiya, C. S. Tornatore, S. A. Houff, and J. R. Berger. 1992. 'Pathogenesis and molecular biology of progressive multifocal leukoencephalopathy, the JC virus-induced demyelinating disease of the human brain', *Clin Microbiol Rev*, 5: 49-73.

Major, E. O., A. E. Miller, P. Mourrain, R. G. Traub, E. de Widt, and J. Sever. 1985. 'Establishment of a line of human fetal glial cells that supports JC virus multiplication', *Proc Natl Acad Sci U S A*, 82: 1257-61.

Mannova, P., D. Liebl, N. Krauzewicz, A. Fejtova, J. Stokrova, Z. Palkova, B. E. Griffin, and J. Forstova. 2002. 'Analysis of mouse polyomavirus mutants with lesions in the minor capsid proteins', *J Gen Virol*, 83: 2309-19.

Mashalidis, E. H., P. Sledz, S. Lang, and C. Abell. 2013. 'A three-stage biophysical screening cascade for fragment-based drug discovery', *Nat Protoc*, 8: 2309-24.

Matthews, B. W. 1968. 'Solvent content of protein crystals', *J Mol Biol*, 33: 491-7.

Mayberry, C. L., A. N. Soucy, C. R. Lajoie, J. K. DuShane, and M. S. Maginnis. 2019. 'JC Polyomavirus Entry by Clathrin-Mediated Endocytosis is Driven by beta-arrestin', *J Virol*.

McCoy, A. J., R. W. Grosse-Kunstleve, P. D. Adams, M. D. Winn, L. C. Storoni, and R. J. Read. 2007. 'Phaser crystallographic software', *J Appl Crystallogr*, 40: 658-74.

McQuaig, S. M., T. M. Scott, J. O. Lukasik, J. H. Paul, and V. J. Harwood. 2009. 'Quantification of human polyomaviruses JC Virus and BK Virus by TaqMan quantitative PCR and comparison to other water quality indicators in water and fecal samples', *Appl Environ Microbiol*, 75: 3379-88.

Metz, I., E. W. Radue, A. Oterino, T. Kumpfel, H. Wiendl, S. Schippling, J. Kuhle, M. A. Sahraian, F. Gray, V. Jakl, D. Hausler, and W. Bruck. 2012. 'Pathology of immune reconstitution inflammatory syndrome in multiple sclerosis with natalizumab-associated progressive multifocal leukoencephalopathy', *Acta Neuropathol*, 123: 235-45.

Mitra, N., S. Sinha, T. N. Ramya, and A. Surolia. 2006. 'N-linked oligosaccharides as outfitters for glycoprotein folding, form and function', *Trends Biochem Sci*, 31: 156-63.

Moens, U., M. Van Ghelue, and B. Ehlers. 2014. 'Are human polyomaviruses co-factors for cancers induced by other oncoviruses?', *Rev Med Virol*, 24: 343-60.

Monaco, M. C., W. J. Atwood, M. Gravell, C. S. Tornatore, and E. O. Major. 1996. 'JC virus infection of hematopoietic progenitor cells, primary B lymphocytes, and tonsillar stromal cells: implications for viral latency', *J Virol*, 70: 7004-12.

Monaco, M. C., P. N. Jensen, J. Hou, L. C. Durham, and E. O. Major. 1998. 'Detection of JC virus DNA in human tonsil tissue: evidence for site of initial viral infection', *J Virol*, 72: 9918-23.

Monk, S. A., J. M. Williams, A. G. Hope, and N. M. Barnes. 2004. 'Identification and importance of N-glycosylation of the human 5-hydroxytryptamine3A receptor subunit', *Biochem Pharmacol*, 68: 1787-96.

Moriyama, T., and A. Sorokin. 2008. 'Intracellular trafficking pathway of BK Virus in human renal proximal tubular epithelial cells', *Virology*, 371: 336-49.

Mosser, S., J. R. Alattia, M. Dimitrov, A. Matz, J. Pascual, B. L. Schneider, and P. C. Fraering. 2015. 'The adipocyte differentiation protein APMAP is an endogenous suppressor of Abeta production in the brain', *Hum Mol Genet*, 24: 371-82.

Muhlenhoff, M., M. Eckhardt, and R. Gerardy-Schahn. 1998. 'Polysialic acid: three-dimensional structure, biosynthesis and function', *Curr Opin Struct Biol*, 8: 558-64.

Munch, J., L. Standker, K. Adermann, A. Schulz, M. Schindler, R. Chinnadurai, S. Pohlmann, C. Chaipan, T. Biet, T. Peters, B. Meyer, D. Wilhelm, H. Lu, W. Jing, S. Jiang, W. G. Forssmann, and F. Kirchhoff. 2007. 'Discovery and optimization of a natural HIV-1 entry inhibitor targeting the gp41 fusion peptide', *Cell*, 129: 263-75.

Murshudov, G. N., P. Skubak, A. A. Lebedev, N. S. Pannu, R. A. Steiner, R. A. Nicholls, M. D. Winn, F. Long, and A. A. Vagin. 2011. 'REFMAC5 for the refinement of macromolecular crystal structures', *Acta Crystallogr D Biol Crystallogr*, 67: 355-67.

Nakanishi, A., N. Itoh, P. P. Li, H. Handa, R. C. Liddington, and H. Kasamatsu. 2007a. 'Minor capsid proteins of simian virus 40 are dispensable for nucleocapsid assembly and cell entry but are required for nuclear entry of the viral genome', *Journal of Virology*, 81: 3778-85.

———. 2007b. 'Minor capsid proteins of simian virus 40 are dispensable for nucleocapsid assembly and cell entry but are required for nuclear entry of the viral genome', *J Virol*, 81: 3778-85.

Nakanishi, A., P. P. Li, Q. M. Qu, Q. H. Jafri, and H. Kasamatsu. 2007. 'Molecular dissection of nuclear entry-competent SV40 during infection', *Virus Research*, 124: 226-30.

Nakanishi, A., D. Shum, H. Morioka, E. Otsuka, and H. Kasamatsu. 2002a. 'Interaction of the Vp3 nuclear localization signal with the importin alpha-2/beta heterodimer directs nuclear entry of infecting simian virus 40', *Journal of Virology*, 76: 9368-77.

———. 2002b. 'Interaction of the Vp3 nuclear localization signal with the importin alpha 2/beta heterodimer directs nuclear entry of infecting simian virus 40', *J Virol*, 76: 9368-77.

Nelson, C. D., A. Derdowski, M. S. Maginnis, B. A. O'Hara, and W. J. Atwood. 2012. 'The VP1 subunit of JC polyomavirus recapitulates early events in viral trafficking and is a novel tool to study polyomavirus entry', *Virology*, 428: 30-40.

Nelson, C. D., L. J. Stroh, G. V. Gee, B. A. O'Hara, T. Stehle, and W. J. Atwood. 2015. 'Modulation of a pore in the capsid of JC polyomavirus reduces infectivity and prevents exposure of the minor capsid proteins', *J Virol*, 89: 3910-21.

Neu, U., S. A. Allen, B. S. Blaum, Y. Liu, M. Frank, A. S. Palma, L. J. Stroh, T. Feizi, T. Peters, W. J. Atwood, and T. Stehle. 2013. 'A structure-guided mutation in the major capsid protein retargets BK polyomavirus', *PLoS Pathog*, 9: e1003688.

Neu, U., J. Bauer, and T. Stehle. 2011. 'Viruses and sialic acids: rules of engagement', *Curr Opin Struct Biol*, 21: 610-8.

Neu, U., Z. M. Khan, B. Schuch, A. S. Palma, Y. Liu, M. Pawlita, T. Feizi, and T. Stehle. 2013. 'Structures of B-lymphotropic polyomavirus VP1 in complex with oligosaccharide ligands', *PLoS Pathog*, 9: e1003714.

Neu, U., M. S. Maginnis, A. S. Palma, L. J. Stroh, C. D. Nelson, T. Feizi, W. J. Atwood, and T. Stehle. 2010. 'Structure-function analysis of the human JC polyomavirus establishes the LSTc pentasaccharide as a functional receptor motif', *Cell Host Microbe*, 8: 309-19.

Neu, U., K. Woellner, G. Gauglitz, and T. Stehle. 2008. 'Structural basis of GM1 ganglioside recognition by simian virus 40', *Proc Natl Acad Sci U S A*, 105: 5219-24.

Ngamukote, S., M. Yanagisawa, T. Ariga, S. Ando, and R. K. Yu. 2007. 'Developmental changes of glycosphingolipids and expression of glycogenes in mouse brains', *J Neurochem*, 103: 2327-41.

Nguyen, D. H., P. Tangvoranuntakul, and A. Varki. 2005. 'Effects of natural human antibodies against a nonhuman sialic acid that metabolically incorporates into activated and malignant immune cells', *J Immunol*, 175: 228-36.
O'Hara, B. A., and W. J. Atwood. 2008. 'Interferon beta1-a and selective anti-5HT(2a) receptor antagonists inhibit infection of human glial cells by JC virus', *Virus Res*, 132: 97-103.
O'Hara, B. A., C. Rupasinghe, A. Yatawara, G. Gaidos, D. F. Mierke, and W. J. Atwood. 2014. 'Gallic acid-based small-molecule inhibitors of JC and BK polyomaviral infection', *Virus Res*, 189: 280-5.
Oppenheim, A., Z. Sandalon, A. Peleg, O. Shaul, S. Nicolis, and S. Ottolenghi. 1992. 'A cis-acting DNA signal for encapsidation of simian virus 40', *J Virol*, 66: 5320-8.
Padgett, B. L., D. L. Walker, G. M. ZuRhein, R. J. Eckroade, and B. H. Dessel. 1971. 'Cultivation of papova-like virus from human brain with progressive multifocal leucoencephalopathy', *Lancet*, 1: 1257-60.
Padler-Karavani, V., H. Yu, H. Cao, H. Chokhawala, F. Karp, N. Varki, X. Chen, and A. Varki. 2008. 'Diversity in specificity, abundance, and composition of anti-Neu5Gc antibodies in normal humans: potential implications for disease', *Glycobiology*, 18: 818-30.
Pastrana, D. V., D. C. Brennan, N. Cuburu, G. A. Storch, R. P. Viscidi, P. S. Randhawa, and C. B. Buck. 2012. 'Neutralization serotyping of BK polyomavirus infection in kidney transplant recipients', *PLoS Pathog*, 8: e1002650.
Pastrana, D. V., U. Ray, T. G. Magaldi, R. M. Schowalter, N. Cuburu, and C. B. Buck. 2013. 'BK polyomavirus genotypes represent distinct serotypes with distinct entry tropism', *J Virol*, 87: 10105-13.
Pavlovic, D., A. C. Patera, F. Nyberg, M. Gerber, M. Liu, and Consortium Progressive Multifocal Leukeoncephalopathy. 2015. 'Progressive multifocal leukoencephalopathy: current treatment options and future perspectives', *Ther Adv Neurol Disord*, 8: 255-73.
Pelkmans, L., and A. Helenius. 2002. 'Endocytosis via caveolae', *Traffic*, 3: 311-20.
Pelkmans, L., J. Kartenbeck, and A. Helenius. 2001. 'Caveolar endocytosis of simian virus 40 reveals a new two-step vesicular-transport pathway to the ER', *Nat Cell Biol*, 3: 473-83.
Peretti, A., E. M. Geoghegan, D. V. Pastrana, S. Smola, P. Feld, M. Sauter, S. Lohse, M. Ramesh, E. S. Lim, D. Wang, C. Borgogna, P. C. FitzGerald, V. Bliskovsky, G. J. Starrett, E. K. Law, R. S. Harris, J. K. Killian, J. Zhu, M. Pineda, P. S. Meltzer, R. Boldorini, M. Gariglio, and C. B. Buck. 2018. 'Characterization of BK Polyomaviruses from Kidney Transplant Recipients Suggests a Role for APOBEC3 in Driving In-Host Virus Evolution', *Cell Host Microbe*, 23: 628-35 e7.
Pfitzner, U., and M. H. Zenk. 1989. 'Homogeneous Strictosidine Synthase Isoenzymes from Cell Suspension Cultures of Catharanthus roseus', *Planta Med*, 55: 525-30.
Pho, M. T., A. Ashok, and W. J. Atwood. 2000. 'JC virus enters human glial cells by clathrin-dependent receptor-mediated endocytosis', *J Virol*, 74: 2288-92.
Ponassi, M., C. Cantoni, R. Biassoni, R. Conte, A. Spallarossa, A. Moretta, L. Moretta, M. Bolognesi, and D. Bordo. 2003. 'Expression and crystallographic characterization of the extracellular domain of human natural killer cell triggering receptor NKp46', *Acta Crystallogr D Biol Crystallogr*, 59: 2259-61.
Ponassi, M., C. Cantoni, R. Biassoni, R. Conte, A. Spallarossa, A. Pesce, A. Moretta, L. Moretta, M. Bolognesi, and D. Bordo. 2003. 'Structure of the human NK cell triggering receptor NKp46 ectodomain', *Biochem Biophys Res Commun*, 309: 317-23.
Prosperini, L., N. de Rossi, C. Scarpazza, L. Moiola, M. Cosottini, S. Gerevini, R. Capra, and P. M. L. study group Italian. 2016. 'Natalizumab-Related Progressive Multifocal Leukoencephalopathy in Multiple Sclerosis: Findings from an Italian Independent Registry', *PLoS One*, 11: e0168376.
Qian, M., D. Cai, K. J. Verhey, and B. Tsai. 2009. 'A lipid receptor sorts polyomavirus from the endolysosome to the endoplasmic reticulum to cause infection', *PLoS Pathog*, 5: e1000465.
Qian, M., and B. Tsai. 2010. 'Lipids and proteins act in opposing manners to regulate polyomavirus infection', *J Virol*, 84: 9840-52.

Qu, Q., H. Sawa, T. Suzuki, S. Semba, C. Henmi, Y. Okada, M. Tsuda, S. Tanaka, W. J. Atwood, and K. Nagashima. 2004. 'Nuclear entry mechanism of the human polyomavirus JC virus-like particle: role of importins and the nuclear pore complex', *J Biol Chem*, 279: 27735-42.

Querbes, W., A. Benmerah, D. Tosoni, P. P. Di Fiore, and W. J. Atwood. 2004. 'A JC virus-induced signal is required for infection of glial cells by a clathrin- and eps15-dependent pathway', *J Virol*, 78: 250-6.

Querbes, W., B. A. O'Hara, G. Williams, and W. J. Atwood. 2006. 'Invasion of host cells by JC virus identifies a novel role for caveolae in endosomal sorting of noncaveolar ligands', *J Virol*, 80: 9402-13.

Quirk, P. L., S. Rao, B. L. Roth, and R. E. Siegel. 2004. 'Three putative N-glycosylation sites within the murine 5-HT3A receptor sequence affect plasma membrane targeting, ligand binding, and calcium influx in heterologous mammalian cells', *J Neurosci Res*, 77: 498-506.

Rainey-Barger, E. K., S. Mkrtchian, and B. Tsai. 2007. 'Dimerization of ERp29, a PDI-like protein, is essential for its diverse functions', *Mol Biol Cell*, 18: 1253-60.

Randhawa, P. S., G. Gupta, A. Vats, R. Shapiro, and R. P. Viscidi. 2006. 'Immunoglobulin G, A, and M responses to BK virus in renal transplantation', *Clin Vaccine Immunol*, 13: 1057-63.

Ray, U., P. Cinque, S. Gerevini, V. Longo, A. Lazzarin, S. Schippling, R. Martin, C. B. Buck, and D. V. Pastrana. 2015. 'JC polyomavirus mutants escape antibody-mediated neutralization', *Sci Transl Med*, 7: 306ra151.

Rayment, I., T. S. Baker, D. L. Caspar, and W. T. Murakami. 1982. 'Polyoma virus capsid structure at 22.5 A resolution', *Nature*, 295: 110-5.

Reid, C. E., H. Li, G. Sur, P. Carmillo, S. Bushnell, R. Tizard, M. McAuliffe, C. Tonkin, K. Simon, S. Goelz, P. Cinque, L. Gorelik, and J. P. Carulli. 2011. 'Sequencing and analysis of JC virus DNA from natalizumab-treated PML patients', *J Infect Dis*, 204: 237-44.

Resh, M. D. 1999. 'Fatty acylation of proteins: new insights into membrane targeting of myristoylated and palmitoylated proteins', *Biochim Biophys Acta*, 1451: 1-16.

Rinaldo, C. H., G. D. Tylden, and B. N. Sharma. 2013. 'The human polyomavirus BK (BKPyV): virological background and clinical implications', *APMIS*, 121: 728-45.

Ringe, D. 1995. 'What makes a binding site a binding site?', *Curr Opin Struct Biol*, 5: 825-9.

Romer, W., L. Berland, V. Chambon, K. Gaus, B. Windschiegl, D. Tenza, M. R. E. Aly, V. Fraisier, J. C. Florent, D. Perrais, C. Lamaze, G. Raposo, C. Steinem, P. Sens, P. Bassereau, and L. Johannes. 2007. 'Shiga toxin induces tubular membrane invaginations for its uptake into cells', *Nature*, 450: 670-U3.

Rothberg, K. G., J. E. Heuser, W. C. Donzell, Y. S. Ying, J. R. Glenney, and R. G. Anderson. 1992. 'Caveolin, a protein component of caveolae membrane coats', *Cell*, 68: 673-82.

Sahli, R., R. Freund, T. Dubensky, R. Garcea, R. Bronson, and T. Benjamin. 1993. 'Defect in entry and altered pathogenicity of a polyoma virus mutant blocked in VP2 myristylation', *Virology*, 192: 142-53.

Salunke, D. M., D. L. Caspar, and R. L. Garcea. 1986. 'Self-assembly of purified polyomavirus capsid protein VP1', *Cell*, 46: 895-904.

———. 1989. 'Polymorphism in the assembly of polyomavirus capsid protein VP1', *Biophys J*, 56: 887-900.

Samraj, A. N., O. M. Pearce, H. Laubli, A. N. Crittenden, A. K. Bergfeld, K. Banda, C. J. Gregg, A. E. Bingman, P. Secrest, S. L. Diaz, N. M. Varki, and A. Varki. 2015. 'A red meat-derived glycan promotes inflammation and cancer progression', *Proc Natl Acad Sci U S A*, 112: 542-7.

Sapparapu, G., E. Fernandez, N. Kose, Cao Bin, J. M. Fox, R. G. Bombardi, H. Zhao, C. A. Nelson, A. L. Bryan, T. Barnes, E. Davidson, I. U. Mysorekar, D. H. Fremont, B. J. Doranz, M. S. Diamond, and J. E. Crowe. 2016. 'Neutralizing human antibodies prevent Zika virus replication and fetal disease in mice', *Nature*, 540: 443-47.

Sauter, N. K., M. D. Bednarski, B. A. Wurzburg, J. E. Hanson, G. M. Whitesides, J. J. Skehel, and D. C. Wiley. 1989. 'Hemagglutinins from two influenza virus variants bind to sialic acid derivatives

with millimolar dissociation constants: a 500-MHz proton nuclear magnetic resonance study', *Biochemistry*, 28: 8388-96.
Scadden, J. R., A. Sharif, K. Skordilis, and R. Borrows. 2017. 'Polyoma virus nephropathy in kidney transplantation', *World J Transplant*, 7: 329-38.
Schelhaas, M., J. Malmstrom, L. Pelkmans, J. Haugstetter, L. Ellgaard, K. Grunewald, and A. Helenius. 2007. 'Simian Virus 40 depends on ER protein folding and quality control factors for entry into host cells', *Cell*, 131: 516-29.
Schmitt, C., L. Raggub, S. Linnenweber-Held, O. Adams, A. Schwarz, and A. Heim. 2014. 'Donor origin of BKV replication after kidney transplantation', *J Clin Virol*, 59: 120-5.
Schnaar, R. L., A. Suzuki, and P. Stanley. 2009. 'Glycosphingolipids.' in nd, A. Varki, R. D. Cummings, J. D. Esko, H. H. Freeze, P. Stanley, C. R. Bertozzi, G. W. Hart and M. E. Etzler (eds.), *Essentials of Glycobiology* (Cold Spring Harbor (NY)).
Schowalter, R. M., and C. B. Buck. 2013. 'The Merkel cell polyomavirus minor capsid protein', *PLoS Pathog*, 9: e1003558.
Schwarz, A., S. Linnenweber-Held, A. Heim, T. Framke, H. Haller, and C. Schmitt. 2016. 'Viral Origin, Clinical Course, and Renal Outcomes in Patients With BK Virus Infection After Living-Donor Renal Transplantation', *Transplantation*, 100: 844-53.
Shah, K., and N. Nathanson. 1976. 'Human exposure to SV40: review and comment', *Am J Epidemiol*, 103: 1-12.
Shah, K. V. 2007. 'SV40 and human cancer: a review of recent data', *Int J Cancer*, 120: 215-23.
Shayman, J. A., and N. S. Radin. 1991. 'Structure and function of renal glycosphingolipids', *Am J Physiol*, 260: F291-302.
Shental-Bechor, D., and Y. Levy. 2008. 'Effect of glycosylation on protein folding: a close look at thermodynamic stabilization', *Proc Natl Acad Sci U S A*, 105: 8256-61.
Shishido-Hara, Y., S. Ichinose, K. Higuchi, Y. Hara, and K. Yasui. 2004. 'Major and minor capsid proteins of human polyomavirus JC cooperatively accumulate to nuclear domain 10 for assembly into virions', *J Virol*, 78: 9890-903.
Silverman, L., and L. J. Rubinstein. 1965. 'Electron microscopic observations on a case of progressive multifocal leukoencephalopathy', *Acta Neuropathol*, 5: 215-24.
Singh, M., B. Tam, and B. Akabayov. 2018. 'NMR-Fragment Based Virtual Screening: A Brief Overview', *Molecules*, 23.
Smith, T. H., L. J. Coronel, J. G. Li, M. R. Dores, M. T. Nieman, and J. Trejo. 2016. 'Protease-activated Receptor-4 Signaling and Trafficking Is Regulated by the Clathrin Adaptor Protein Complex-2 Independent of beta-Arrestins', *J Biol Chem*, 291: 18453-64.
Sock, E., K. Renner, D. Feist, H. Leger, and M. Wegner. 1996. 'Functional comparison of PML-type and archetype strains of JC virus', *J Virol*, 70: 1512-20.
Solis, M., A. Velay, R. Porcher, P. Domingo-Calap, E. Soulier, M. Joly, M. Meddeb, W. Kack-Kack, B. Moulin, S. Bahram, F. Stoll-Keller, H. Barth, S. Caillard, and S. Fafi-Kremer. 2018. 'Neutralizing Antibody-Mediated Response and Risk of BK Virus-Associated Nephropathy', *J Am Soc Nephrol*, 29: 326-34.
Sroller, V., E. Hamsikova, V. Ludvikova, P. Vochozkova, M. Kojzarova, M. Fraiberk, M. Salakova, A. Moravkova, J. Forstova, and S. Nemeckova. 2014. 'Seroprevalence rates of BKV, JCV, and MCPyV polyomaviruses in the general Czech Republic population', *J Med Virol*, 86: 1560-8.
Stehle, T., S. J. Gamblin, Y. Yan, and S. C. Harrison. 1996. 'The structure of simian virus 40 refined at 3.1 A resolution', *Structure*, 4: 165-82.
Stehle, T., and S. C. Harrison. 1996. 'Crystal structures of murine polyomavirus in complex with straight-chain and branched-chain sialyloligosaccharide receptor fragments', *Structure*, 4: 183-94.
———. 1997. 'High-resolution structure of a polyomavirus VP1-oligosaccharide complex: implications for assembly and receptor binding', *EMBO J*, 16: 5139-48.
Stehle, T., Y. Yan, T. L. Benjamin, and S. C. Harrison. 1994. 'Structure of murine polyomavirus complexed with an oligosaccharide receptor fragment', *Nature*, 369: 160-3.

Stergiou, L., M. Bauer, W. Mair, D. Bausch-Fluck, N. Drayman, B. Wollscheid, A. Oppenheim, and L. Pelkmans. 2013. 'Integrin-mediated signaling induced by simian virus 40 leads to transient uncoupling of cortical actin and the plasma membrane', *PLoS One*, 8: e55799.

Stewart, S. E., B. E. Eddy, and N. Borgese. 1958. 'Neoplasms in mice inoculated with a tumor agent carried in tissue culture', *J Natl Cancer Inst*, 20: 1223-43.

Stolt, A., K. Sasnauskas, P. Koskela, M. Lehtinen, and J. Dillner. 2003. 'Seroepidemiology of the human polyomaviruses', *J Gen Virol*, 84: 1499-504.

Streuli, C. H., and B. E. Griffin. 1987. 'Myristic acid is coupled to a structural protein of polyoma virus and SV40', *Nature*, 326: 619-22.

Stroh, L. J., M. S. Maginnis, B. S. Blaum, C. D. Nelson, U. Neu, G. V. Gee, B. A. O'Hara, N. Motamedi, D. DiMaio, W. J. Atwood, and T. Stehle. 2015. 'The Greater Affinity of JC Polyomavirus Capsid for alpha2,6-Linked Lactoseries Tetrasaccharide c than for Other Sialylated Glycans Is a Major Determinant of Infectivity', *J Virol*, 89: 6364-75.

Stroh, L. J., and T. Stehle. 2014. 'Glycan Engagement by Viruses: Receptor Switches and Specificity', *Annu Rev Virol*, 1: 285-306.

Sunyaev, S. R., A. Lugovskoy, K. Simon, and L. Gorelik. 2009. 'Adaptive mutations in the JC virus protein capsid are associated with progressive multifocal leukoencephalopathy (PML)', *PLoS Genet*, 5: e1000368.

Suzuki, T., Y. Orba, Y. Okada, Y. Sunden, T. Kimura, S. Tanaka, K. Nagashima, W. W. Hall, and H. Sawa. 2010. 'The human polyoma JC virus agnoprotein acts as a viroporin', *PLoS Pathog*, 6: e1000801.

Sweet, B. H., and M. R. Hilleman. 1960. 'The vacuolating virus, S.V. 40', *Proc Soc Exp Biol Med*, 105: 420-7.

Szklarczyk, O. M., N. Gonzalez-Segredo, P. Kukura, A. Oppenheim, D. Choquet, V. Sandoghdar, A. Helenius, I. F. Sbalzarini, and H. Ewers. 2013. 'Receptor concentration and diffusivity control multivalent binding of Sv40 to membrane bilayers', *PLoS Comput Biol*, 9: e1003310.

Tan, C. S., and I. J. Koralnik. 2010. 'Progressive multifocal leukoencephalopathy and other disorders caused by JC virus: clinical features and pathogenesis', *Lancet Neurol*, 9: 425-37.

Tan, I. L., I. J. Koralnik, J. A. Rumbaugh, P. C. Burger, A. King-Rennie, and J. C. McArthur. 2011. 'Progressive multifocal leukoencephalopathy in a patient without immunodeficiency', *Neurology*, 77: 297-9.

Tangvoranuntakul, P., P. Gagneux, S. Diaz, M. Bardor, N. Varki, A. Varki, and E. Muchmore. 2003. 'Human uptake and incorporation of an immunogenic nonhuman dietary sialic acid', *Proc Natl Acad Sci U S A*, 100: 12045-50.

Tillou, X., and A. Doerfler. 2014. 'Urological tumors in renal transplantation', *Minerva Urol Nefrol*, 66: 57-67.

Tornatore, C., J. R. Berger, S. A. Houff, B. Curfman, K. Meyers, D. Winfield, and E. O. Major. 1992. 'Detection of JC virus DNA in peripheral lymphocytes from patients with and without progressive multifocal leukoencephalopathy', *Ann Neurol*, 31: 454-62.

Tsai, B., J. M. Gilbert, T. Stehle, W. Lencer, T. L. Benjamin, and T. A. Rapoport. 2003. 'Gangliosides are receptors for murine polyoma virus and SV40', *EMBO J*, 22: 4346-55.

Tsai, B., and M. Qian. 2010. 'Cellular entry of polyomaviruses', *Curr Top Microbiol Immunol*, 343: 177-94.

van der Meijden, E., R. W. Janssens, C. Lauber, J. N. Bouwes Bavinck, A. E. Gorbalenya, and M. C. Feltkamp. 2010. 'Discovery of a new human polyomavirus associated with trichodysplasia spinulosa in an immunocompromized patient', *PLoS Pathog*, 6: e1001024.

Van Loy, T., K. Thys, C. Ryschkewitsch, O. Lagatie, M. C. Monaco, E. O. Major, L. Tritsmans, and L. J. Stuyver. 2015. 'JC virus quasispecies analysis reveals a complex viral population underlying progressive multifocal leukoencephalopathy and supports viral dissemination via the hematogenous route', *J Virol*, 89: 1340-7.

Vargas, D. L., and W. R. Tyor. 2017. 'Update on disease-modifying therapies for multiple sclerosis', *J Investig Med*, 65: 883-91.

Varki, A. 2001. 'Loss of N-glycolylneuraminic acid in humans: Mechanisms, consequences, and implications for hominid evolution', *Am J Phys Anthropol*, Suppl 33: 54-69.
———. 2009. 'Multiple changes in sialic acid biology during human evolution', *Glycoconj J*, 26: 231-45.
Varki, A., and R. Schauer. 2009. 'Sialic Acids.' in nd, A. Varki, R. D. Cummings, J. D. Esko, H. H. Freeze, P. Stanley, C. R. Bertozzi, G. W. Hart and M. E. Etzler (eds.), *Essentials of Glycobiology* (Cold Spring Harbor (NY)).
Varki, N. M., and A. Varki. 2007. 'Diversity in cell surface sialic acid presentations: implications for biology and disease', *Lab Invest*, 87: 851-7.
Vembar, S. S., and J. L. Brodsky. 2008. 'One step at a time: endoplasmic reticulum-associated degradation', *Nat Rev Mol Cell Biol*, 9: 944-57.
Vermersch, P., L. Kappos, R. Gold, J. F. Foley, T. Olsson, D. Cadavid, C. Bozic, and S. Richman. 2011. 'Clinical outcomes of natalizumab-associated progressive multifocal leukoencephalopathy', *Neurology*, 76: 1697-704.
Walczak, C. P., and B. Tsai. 2011. 'A PDI family network acts distinctly and coordinately with ERp29 to facilitate polyomavirus infection', *J Virol*, 85: 2386-96.
Wasik, B. R., K. N. Barnard, and C. R. Parrish. 2016. 'Effects of Sialic Acid Modifications on Virus Binding and Infection', *Trends Microbiol*, 24: 991-1001.
Waterhouse, A., M. Bertoni, S. Bienert, G. Studer, G. Tauriello, R. Gumienny, F. T. Heer, T. A. P. de Beer, C. Rempfer, L. Bordoli, R. Lepore, and T. Schwede. 2018. 'SWISS-MODEL: homology modelling of protein structures and complexes', *Nucleic Acids Res*, 46: W296-W303.
Whitlow, M., B. A. Bell, S. L. Feng, D. Filpula, K. D. Hardman, S. L. Hubert, M. L. Rollence, J. F. Wood, M. E. Schott, D. E. Milenic, and et al. 1993. 'An improved linker for single-chain Fv with reduced aggregation and enhanced proteolytic stability', *Protein Eng*, 6: 989-95.
Wielens, J., S. J. Headey, D. I. Rhodes, R. J. Mulder, O. Dolezal, J. J. Deadman, J. Newman, D. K. Chalmers, M. W. Parker, T. S. Peat, and M. J. Scanlon. 2013. 'Parallel screening of low molecular weight fragment libraries: do differences in methodology affect hit identification?', *J Biomol Screen*, 18: 147-59.
Williams, T. M., F. Medina, I. Badano, R. B. Hazan, J. Hutchinson, W. J. Muller, N. G. Chopra, P. E. Scherer, R. G. Pestell, and M. P. Lisanti. 2004. 'Caveolin-1 gene disruption promotes mammary tumorigenesis and dramatically enhances lung metastasis in vivo. Role of Cav-1 in cell invasiveness and matrix metalloproteinase (MMP-2/9) secretion', *J Biol Chem*, 279: 51630-46.
Wolf, A. A., M. G. Jobling, D. E. Saslowsky, E. Kern, K. R. Drake, A. K. Kenworthy, R. K. Holmes, and W. I. Lencer. 2008. 'Attenuated endocytosis and toxicity of a mutant cholera toxin with decreased ability to cluster ganglioside GM1 molecules', *Infect Immun*, 76: 1476-84.
Wuthrich, C., Y. M. Cheng, J. T. Joseph, S. Kesari, C. Beckwith, E. Stopa, J. E. Bell, and I. J. Koralnik. 2009. 'Frequent infection of cerebellar granule cell neurons by polyomavirus JC in progressive multifocal leukoencephalopathy', *J Neuropathol Exp Neurol*, 68: 15-25.
Xu, C., and D. T. Ng. 2015. 'Glycosylation-directed quality control of protein folding', *Nat Rev Mol Cell Biol*, 16: 742-52.
Xu, D., E. I. Newhouse, R. E. Amaro, H. C. Pao, L. S. Cheng, P. R. Markwick, J. A. McCammon, W. W. Li, and P. W. Arzberger. 2009. 'Distinct glycan topology for avian and human sialopentasaccharide receptor analogues upon binding different hemagglutinins: a molecular dynamics perspective', *J Mol Biol*, 387: 465-91.
Yan, Y., T. Stehle, R. C. Liddington, H. Zhao, and S. C. Harrison. 1996. 'Structure determination of simian virus 40 and murine polyomavirus by a combination of 30-fold and 5-fold electron-density averaging', *Structure*, 4: 157-64.
Yogo, Y., T. Kitamura, C. Sugimoto, T. Ueki, Y. Aso, K. Hara, and F. Taguchi. 1990. 'Isolation of a possible archetypal JC virus DNA sequence from nonimmunocompromised individuals', *J Virol*, 64: 3139-43.
You, J., S. D. O'Hara, P. Velupillai, S. Castle, S. Levery, R. L. Garcea, and T. Benjamin. 2015. 'Ganglioside and Non-ganglioside Mediated Host Responses to the Mouse Polyomavirus', *PLoS Pathog*, 11: e1005175.

Yu, R. K., L. J. Macala, T. Taki, H. M. Weinfield, and F. S. Yu. 1988. 'Developmental changes in ganglioside composition and synthesis in embryonic rat brain', *J Neurochem*, 50: 1825-9.
Yu, R. K., Y. Nakatani, and M. Yanagisawa. 2009. 'The role of glycosphingolipid metabolism in the developing brain', *J Lipid Res*, 50 Suppl: S440-5.
Yu, R. K., Y. T. Tsai, T. Ariga, and M. Yanagisawa. 2011. 'Structures, biosynthesis, and functions of gangliosides--an overview', *J Oleo Sci*, 60: 537-44.
Zhang, Z., Z. Zhu, W. Chen, Z. Cai, B. Xu, Z. Tan, A. Wu, X. Ge, X. Guo, Z. Tan, Z. Xia, H. Zhu, T. Jiang, and Y. Peng. 2019. 'Cell membrane proteins with high N-glycosylation, high expression and multiple interaction partners are preferred by mammalian viruses as receptors', *Bioinformatics*, 35: 723-28.
Zheng, H. Y., T. Takasaka, K. Noda, A. Kanazawa, H. Mori, T. Kabuki, K. Joh, T. Oh-ishi, H. Ikegaya, K. Nagashima, W. W. Hall, T. Kitamura, and Y. Yogo. 2005. 'New sequence polymorphisms in the outer loops of the JC polyomavirus major capsid protein (VP1) possibly associated with progressive multifocal leukoencephalopathy', *J Gen Virol*, 86: 2035-45.
Zhu, A., and R. Hurst. 2002. 'Anti-N-glycolylneuraminic acid antibodies identified in healthy human serum', *Xenotransplantation*, 9: 376-81.
Zila, V., F. Difato, L. Klimova, S. Huerfano, and J. Forstova. 2014. 'Involvement of microtubular network and its motors in productive endocytic trafficking of mouse polyomavirus', *PLoS One*, 9: e96922.
Zurhein, G., and S. M. Chou. 1965. 'Particles Resembling Papova Viruses in Human Cerebral Demyelinating Disease', *Science*, 148: 1477-9.

8. Acknowledgments

Vielen lieben Dank möchte ich sagen an…

- Prof. Dr. Thilo Stehle, für die kompetente und positive Betreuung meiner Promotion, für das Ermöglichen eines freien wissenschaftlichen Arbeitens und das Fördern eigenständiger Ideen sowie für die stets menschliche Unterstützung.

- Prof. Dr. Dirk Schwarzer für die spontane Bereitschaft, die Zweitbetreuung meiner Promotion zu übernehmen.

- Prof. Dr. Walter Atwood for the helpful support, scientific advice and fruitful collaboration.

- Allen Mitgliedern des AK Stehle insbesondere den (jetzigen aber auch ehemaligen) Mitgliedern des „Eliteoffice“ Georg, Micha, Elena, Yinglan, Melli, Bärbel und Luisa für die Hilfsbereitschaft und die produktiven Diskussionen. Danke für die schöne Zeit, die lustigen Kuchenpausen und Laborausflüge.

- Irmi und Erik für die gute Zusammenarbeit und die langen Sitzungen im Roboterraum zwecks Betreuung der Roboter aka „viscious machines from hell“.

- Den ehemaligen Arbeitsgruppenmitgliedern, ganz besonders Joana und Felix, Melli, MicBuc und Manu für die produktiven Gespräche, die Hilfsbereitschaft und wunderbaren Treffen auch über den Laboralltag hinaus.

- Den tatkräftigen Helferlein Andreas, Max und Fabian, die mich in guter Zusammenarbeit in den Projekten unterstützt haben. Ein besonderer Dank geht hierbei an Jasmin, meine rechte und linke Hand im Labor in den letzten Monaten, die sich trotz schwieriger Projekte nicht den Optimismus und die Motivation in der Wissenschaft hat nehmen lassen.

- Meinen Freunden, Simone und Tobi, Dennis und Franzi, Anika, Täin, Mole, Markus, Stefan, David und Jenn und Kate, egal wie groß die räumliche Entfernung auch sein mag, danke, dass ihr immer für einen da seid.

- Meiner Familie, die immer für mich da ist und mich nie hat vergessen lassen, wo ich herkomme. Durch euch komme ich immer wieder gerne in die Heimat zurück. Danke für die immerwährende Unterstützung.

- Daniel, ohne dich wäre ich nicht da, wo ich jetzt bin. Vielen Dank für all die wundervollen Jahre, und ich freue mich schon auf unseren nächsten großen Lebensabschnitt. Ich liebe dich.

- Kriemel, keiner konnte mir die Zeit des Schreibens so sehr versüßen wie du. Eine bessere Begleitung für die Zeit konnte ich mir nicht wünschen. Wir freuen uns, dich bald in den Armen halten zu dürfen.